ABSTRACT

Large Scale Fused Filament Fabrication:
The Effects of Process Parameters on Bead Geometry

Nathan K. Spinnie, M.S.M.E.

Mentor: Douglas E. Smith, Ph.D.

Fused Filament Fabrication (FFF) continues to grow, expanding beyond small scale prototyping to large scale industrial use. This study examines parameters for scaling FFF, concentrating on polymer bead geometry. Bead shape is important because individual beads are the mesostructure that determine the mechanical properties of a printed part, with large scale parts requiring fiber inclusions to achieve strengthened mechanical properties; bead shape should be rectangular to prevent voids. Using a single screw polymer extruder capable of producing 13 lbs/hr HDPE and an 18”x18” build platform, parameters including nozzle height, screw RPM, platform speed, polymer type, and short fiber inclusions were adjusted to study parameter effects on bead geometry. Parameters were studied to understand conditions for optimal outputs such as cross-sectional shape and minimizing voids. Results indicate that elevated platform velocities and nozzle heights are optimal for large scale deposition, while fiber reinforced polymers are highly sensitive to the deposition process.

Large Scale Fused Filament Fabrication:
The Effects of Process Parameters on Bead Geometry

by

Nathan K. Spinnie, B.S.E.

A Thesis

Approved by the Department of Mechanical Engineering

_____

William Jordan, Ph.D., Chairperson

Submitted to the Graduate Faculty of
Baylor University in Partial Fulfillment of the
Requirements for the Degree
of

Master of Science in Mechanical Engineering

Approved by the Thesis Committee

_____

Douglas E. Smith, Ph.D., Chairperson

_____

David A. Jack, Ph.D.

_____

Scott James, Ph.D.

Accepted by the Graduate School

August 2016

_____

J. Larry Lyon, Ph.D., Dean

Page bearing signatures is kept on file in the Graduate School.

TABLE OF CONTENTS

LIST OF FIGURES vii

LIST OF TABLES xi

ACKNOWLEDGMENTS xiii

DEDICATION xiv

CHAPTER ONE 1

Introduction 1

1.1 Motivation and Objective 2

1.2 Order of Thesis 6

CHAPTER TWO 7

Literature Review 7

2.1 Fused Filament Fabrication 7

2.1.1 Overview of Technologies 8

2.1.2 Fused Filament Fabrication Materials 14

2.1.3 Process Parameters and Development 16

2.1.4 Material Properties 18

2.1.5 Large Scale Adaptation 21

2.2 Fiber Reinforcement 24

2.2.1 Fiber Orientation Background 25

2.3.3 FFF Fiber Reinforcement 29

2.3 Process Dynamics and Effects 31

2.3.2 Processing Effects 36

2.4. Application to Current Work 37

CHAPTER THREE 39
Experimental Methods 39
3.1 System Design and Improvements 39
3.1.1 Initial Large Scale FFF Extruder 40
3.1.2 Table Design and Improvements 48
3.2 Sample Preparation and Manufacturing 54
3.2.1 Sample Preparation 54
3.2.2 Large Scale FFF Deposition 69
3.3 Image Processing 76
3.3.1 Imaging 77
3.3.2 Image Processing 78
CHAPTER FOUR 81
Data Analysis 81
4.1 Flowrate and Freestream Analysis 81
4.1.1 Parameter Flowrate Analysis 81
4.1.2 Bead Cross Section Analysis 90
4.1.3 Error Analysis 103
4.2 Bead Geometry Parameter Analyses 109
4.2.1 Bead Aspect Ratio 109
4.2.2 Swell Ratios 118
4.2.3 Bead Shape Convexity 135
4.2.4 Shape Compactness 140
4.3 Bead Shape Prediction Regression 146
4.3.1. Least Squares Regression Model 146
4.3.2. Deposition Prediction Models 148

4.3.3. Regression Summary 152
CHAPTER FIVE 156
Conclusions and Future Work 156
5.1 Conclusions 156
5.1.1. Polymer Specific Conclusions 157
5.1.2. General Conclusions 159
5.2. Future Work 159
5.2.1. System Improvements 160
5.2.2. Further Studies 160
APPENDIX 162
APPENDIX A 163
Large Scale Deposition System Operation 163
A.1 Platform 163
A.2 Exon8 Extruder 170
BIBLIOGRAPHY 175

LIST OF FIGURES

Figure 2.1. Computer model converted to STL with center hole estimated using triangles. 12

Figure 2.2. Bead deposition pattern on build platform. 12

Figure 2.3. Illustration of the square-cube problem. 22

Figure 2.4. Liquefier diagram including filament rollers and nozzle apparatus. 33

Figure 2.5. Standard liquefier and nozzle geometry for FFF. 35

Figure 3.1. Brabender single screw extruder. 41

Figure 3.2. Brabender 90° attachment for vertical extrusion. 42

Figure 3.3. Brabender 90° attachment with resistive wiring heat tape. 43

Figure 3.4. Exon8 mounted on suspension stand. 45

Figure 3.5. Hopper rotated from 45° to 90° to increase feeding pressure and allow all pellets to feed into extruder. 45

Figure 3.6. Amphora™ polymer clogs in the feeding section of the hopper where it connects to the first flight of the extrusion screw. 46

Figure 3.7. Initial oval cross-sectional area of impinging pellets (a), placement of aluminum spacers (b), and resulting pellet impingement area (c). 47

Figure 3.8. Initial platform using drawer slides to translate second axis. 49

Figure 3.9. Translation platform with two automatic axes. 50

Figure 3.10. Brackets printed on the MakerBot Replicator 2X to attach electronics. 51

Figure 3.11. Diagram of (a) piston motion allowing for two degrees of freedom, and (b) MakerBot printed piston sleeve. 51

Figure 3.12. Cable carrier with individual links printed using FFF. 52

Figure 3.13. TGA drying tests for (a) Amphora™, (b) Neat ABS, (c) 10% Carbon Fiber filled ABS, and (d) 13% Carbon Fiber filled ABS. 57

Figure 3.14. Burnoff test for neat ABS ramped up to and held at 500°C for 80 mins. 58

Figure 3.15. Burnoff test for 3 pellet samples of 13% carbon fiber filled ABS ramped to and held at 500°C for 60 mins. 59

Figure 3.16. Burnoff test for 10% Carbon Fiber Filled ABS ramped up to and held at 500°C for 60 minutes. 60

Figure 3.17. DSC tests showing T_g and T_m for (a) Amphora™, (b) Neat ABS, (c) 10% Carbon Fiber filled ABS, and (d) 13% Carbon Fiber filled ABS. 62

Figure 3.18. DSC comparison plot of required heat to process. 63

Figure 3.19. Melt Flow Indexer data for each polymer as a function of flowrate. 65

Figure 3.20. SEM images of carbon fiber lengths in µm. 67

Figure 3.21. Individual sample fiber length distributions and combined distribution overlaid with a Weibull distribution curve. 68

Figure 3.22. Path generation of a single bead. 72

Figure 3.23. Example bead printed with Amphora™, showing print path and flow pulsing. 75

Figure 3.24. Freestream samples printed using Amphora™. 76

Figure 3.25. Sample ABS cross section showing horizontal alignment technique. 78

Figure 3.26. Imaging process of an Amphora™ bead cross section, from (a) printed bead to (b) cut, (c) dye, (d) crop, (e) black/white image, and (f) boundary trace. 80

Figure 4.1. Interpretation legend (a) and freestream flowrate compared with bead flowrate for Amphora™ (b), Neat ABS (c), 10% CF ABS (d), and 13% CF ABS (e). 84

Figure 4.2. Revised Amphora™ freestream flowrate to compensate for pulsing effect. 87

Figure 4.3. Amphora™ bead cross sections over all parameter values studied, at nozzle heights of (a) 1.5, (b) 3.25, and (c) and 5 mm. Printed at a platform temperature of 65°C and an extrusion temperature of 240°C. 92

Figure 4.4. Neat ABS bead cross sections over all parameter values studied, at nozzle heights of (a) 1.5, (b) 3.25, and (c) and 5 mm. Printed at a platform temperature of 65°C and an extrusion temperature of 230°C. 95

Figure 4.5. 10% carbon fiber filled ABS bead cross sections over all parameter values studied, at nozzle heights of (a) 1.5, (b) 3.25, and (c) and 5 mm. Printed at a platform temperature of 65°C and an extrusion temperature of 230°C. 98

Figure 4.6. 13% carbon fiber filled ABS bead cross sections over all parameter values studied, at nozzle heights of (a) 1.5, (b) 3.25, and (c) and 5 mm. Printed at a platform temperature of 65°C and an extrusion temperature of 230°C. 101

Figure 4.7. Amphora™ flowrate data with error bars for (a) 1.5, (b) 3.25, and (c) 5 mm nozzle heights. 105

Figure 4.8. Neat ABS flowrate data with error bars for (a) 1.5, (b) 3.25, and (c) 5 mm nozzle heights. 107

Figure 4.9. Interpretation legend for specific parameter plots. 109

Figure 4.10. RPM vs aspect ratio for (a) Amphora™, (b) Neat ABS, (c) 10% CF ABS, and (d) 13% CF ABS. 112

Figure 4.11. Amphora™ aspect ratio data with error bars for (a) 1.5, (b) 3.25, and (c) 5 mm nozzle heights. 115

Figure 4.12. Neat ABS aspect ratio data with error bars for (a) 1.5, (b) 3.25, and (c) 5 mm nozzle heights. 118

Figure 4.13. Horizontal and vertical swell ratios for (a-b) Amphora™, (c-d) Neat ABS, (e-f) 10% CF ABS, and (g-h) 13% CF ABS. 124

Figure 4.14. Amphora™ swell data for vertical swell at (a) 1.5, (b) 3.25, (c) 5 mm, and horizontal swell at (d) 1.5, (e) 3.25, and (f) 5 mm nozzle heights. 129

Figure 4.15. Neat ABS swell data for vertical (a) 1.5, (b) 3.25, (c) 5 mm, and horizontal (d) 1.5, (e) 3.25, and (f) 5 mm nozzle heights. 133

Figure 4.16. Sample bead cross section overlaid with convex hull. 136

Figure 4.17. Convexity ratios for (a) Amphora™, (b) Neat ABS, (c) 10% CF ABS, and (d) 13% CF ABS over all parameter values studied. 138

Figure 4.18. Shape compactness ratio for a square, a circle, and a triangle when using best-fit circumscribing rectangle. 142

Figure 4.19. Shape compactness ratios for (a) Amphora™, (b) Neat ABS, (c) 10% CF ABS, and (d) 13% CF ABS over all parameter values studied. 144

Figure A.1. Stepper motor placement for (x,y) axes..... 163

Figure A.2. Table circuit diagrams. 165

Figure A.3. LabVIEW block diagram and user interface for operating platform..... 166

Figure A.4. Translation pattern from Table A.2. 169

Figure A.5. Exon8 Control Box. 170

Figure A.6. Exon8 in Off (left) and On (right) positions. 171

Figure A.7. Exon8 Control Box immediately after being turned on. 171

Figure A.8. Vertical axis translation system. 173

Figure A.9. Slide-lock nut movement. 173

LIST OF TABLES

Table 3.1. SEM settings used to measure fiber distribution data for 13% Carbon Fiber Filled ABS pellets. 66

Table 3.2. Parameter settings defined using minimum, maximum, and intermediate 69

Table 4.3. Flowrate Coefficient of Variation Values for Amphora™. 106

Table 4.4. Flowrate Coefficient of Variation Values for Neat ABS..... 108

Table 4.5. Aspect Ratio Coefficient of Variation Values for Amphora™. 116

Table 4.6. Aspect Ratio Coefficient of Variation Values for Neat ABS. 118

Table 4.7. Amphora™ vertical swell % coefficient of variation values..... 129

Table 4.8. Amphora™ horizontal swell % coefficient of variation values. 130

Table 4.9. Neat ABS vertical swell % coefficient of variation values. 134

Table 4.10. Neat ABS horizontal swell % coefficient of variation values. 134

Table 4.11. Coefficient of determination for Amphora™ models..... 148

Table 4.12. Coefficient of determination for Neat ABS models. 149

Table 4.13. Coefficient of determination for 10% carbon fiber filled ABS models..... 151

Table 4.14. Coefficient of determination for 13% carbon fiber filled ABS models..... 152

Table 4.15. Regression Coefficients for Flowrate 153

Table 4.16. Regression Coefficients for Bead Width 153

Table 4.17. Regression Coefficients for Bead Height 153

Table 4.18. Regression Coefficients for Aspect Ratio..... 153

Table 4.19. Regression Coefficients for Horizontal Swell 154

Table 4.20. Regression Coefficients for Vertical Swell 154

Table 4.21. Regression Coefficients for Convexity..... 154

Table 4.22. Regression Coefficients for Compactness 154

Table A.1. List of basic commands for operating platform. 167

Table A.2. List of initiation and concatenation commands for operating platform. 168

ACKNOWLEDGMENTS

To my advisor, Dr. Douglas E. Smith, for his guidance, insight, and expertise as my research progressed. Thank you for supporting me during these past two years, it has been a fulfilling experience.

To my professor, Dr. David Jack, who fielded many research questions even though he wasn't my advisor. Thank you for your patience and advice, and for looking at MatLab code even when "quick question" wasn't usually quick or just one question.

To my committee member, Dr. Scott James, for his willingness to be on my committee. Thank you for your valuable insight into my research from a different perspective.

To my fiancée, Julia, for her support and encouragement but also for her willingness to listen. Thank you for keeping me going on the days when I didn't want to, for understanding when the guys at the BRIC got to see me more than you did, and for listening and nodding along as I tell you the newest cool MatLab command I discovered.

To my family, for their support and encouragement from afar as I pursued this endeavor. Thanks for believing in me.

To the guys at the BRIC, specifically Blake and Robbie, for valuable discussion and insight into research, and for making an atmosphere where it was fun to come to work. Thanks for making the office entertaining, for the random nerf shenanigans, and for being great friends.

DEDICATION

To David Dietz, who taught a class of 6th grade students and had nicknames for all of them. Mine was Spinmaster, and by his hand science transformed from a subject to a lifelong passion. Now truly a Master, I can only hope my work will influence others half as much as his teaching touched mine. May he rest in peace.

CHAPTER ONE

Introduction

Additive Manufacturing (AM) is a growing suite of manufacturing technologies that produce three-dimensional parts layer-by-layer, adding material to each layer to create a finished product. The general process for creating an AM part begins with computer modeling software, where a three-dimensional part is generated and saved in a file format that can be read by an AM machine, typically Stereolithography (STL), which condenses the part to a combination of triangular prisms. Common AM processes include Stereolithography (SL), which uses a photosensitive fluid exposed to UV light, Selective Laser Sintering (SLS), where metallic powder is solidified using lasers, and Laminated Object Manufacturing (LOM), where sheets of laminate are cut to the layer pattern and adhered to previous layers. There are several major benefits to AM processes, including elimination of tooling and molds used in traditional manufacturing methods, identical price points for small and large batches of parts, and the high degree of complexity an AM part can possess over a traditionally manufactured part with little to no added cost.

Fused Filament Fabrication (FFF) is one specific technology in the AM group that lays down molten thermoplastic filament in layers on a build plate before incrementing in the vertical direction and starting the next layer. FFF technology has the capacity to redefine manufacturing processes, with a niche market for small-volume production that would normally require expensive tooling. FFF prototype parts can go from the drawing board to physical realization in a matter of hours, allowing users to iteratively design

geometrically complex and innovatively refreshing parts in industries where iteration and innovation have been previously limited. FFF has already allowed for a paradigm shift in industrial manufacturing by redefining the design process, but continues to hold promise as a revolutionary technology with a broader scope than prototyping and modeling.

1.1 Motivation and Objective

Currently, FFF technology is focused on designing and prototyping, with scale models printed on small machines with approximately 0.25 ft^3 of build volume, allowing researchers to physically manipulate and examine how parts fit together, and how the design might be improved, without wasting resources by manufacturing a full-sized prototype. Using traditional processes, it is possible to produce only the final part where all design takes place within a computer environment without the aid of FFF, but these parts are rarely optimized due to the prohibitive cost of design iterations. Even with successful improvements to the manufacturing design process using computer simulated environments in conjunction with FFF, the potential manufacturing applications of FFF technology have yet to be fully realized.

While prototyping is extremely useful, final production of a part is typically achieved using conventional methods and materials, which sets limits on the design space based on manufacturing process limitations. Furthermore, traditional manufacturing requires expensive tooling that drives up the startup cost of production, and makes small batch production extremely expensive. To combat these issues, it would be beneficial to apply FFF to the manufacturing of final parts rather than just the design prototypes. However, to accomplish this manufacturing goal, several factors must be addressed that

currently prevent today's FFF technology from successfully manufacturing production parts.

The first major limitation is the size of a typical FFF part. The MakerBot Replicator 2X Desktop 3D Printer (MakerBot Industries, Brooklyn, NY), representative of the existing 3D desktop printers, has a build volume of 24.6 L x 15.2 W x 15.5 H cm, which is equivalent to 0.26 ft^3 [1]. The scale of most industrial parts is much larger than a build volume of 0.26 ft^3, which is limited to such a small space by several factors. The filament used in FFF processes is small. Most desktop FFF printers use a filament feedstock having a 1.75 mm diameter, which is extruded through a nozzle only 0.4 mm in diameter. Small filament diameter limits the size of potential parts; even printed inside the current build volume, parts can potentially take days or weeks to fully print. For example, the MakerBot Replicator 2X, with a build volume of 0.26ft^3 printing at a high resolution of 0.1 mm bead height, 0.2 mm bead width, and 150 mm/s print speed would take 4 weeks, 9 hours, 41 minutes, and 40 seconds. FFF systems also use a heater to melt the polymer, which is only effective on a small scale filament to allow the heater to fully and consistently melt the polymer as it feeds into the nozzle. Therefore, small scale systems are severely limited by filament size, print time, and the mechanism by which they melt the polymer filament.

Secondly, the overall mechanical properties of an FFF printed part are defined by the initial mechanical properties of the polymer as well as changes in these properties caused during printing. Therefore, a printed part can only ever be as strong as the polymer used to produce it, which is generally weak compared to the desired properties of the part. For example, FFF parts are commonly printed using acrylonitrile-butadiene-

styrene (ABS), which has a Young's Modulus of 1.4-3.1 GPa, compared to 69 GPa for aluminum and 180 GPa for stainless steel [2]. For the properties of FFF parts to be comparable to that of metallic parts, the modulus of an FFF part needs to be improved.

Increased mechanical properties may be achieved by adding discrete fibers into the polymer filament. For example, T300 carbon fibers have a Young's Modulus of 230 GPa. Therefore, the rule of mixtures would predict that 70% ABS with 30% carbon fiber would provide the same modulus as aluminum [3]. Unfortunately, there are more complex mechanisms involved than simply combining percentages of each material, such as the directional dependency of the embedded fibers and the bonding between fibers and matrix. The rule of mixtures sufficiently demonstrates that fiber inclusion can significantly improve part strength if researchers can optimize the FFF process to take advantage of the potential for improved properties.

Therefore, it becomes imperative that to shift the application of FFF from design prototyping to industrial manufacturing, two criteria must be met; first, that the current size of deposition be increased to accommodate a larger build volume, and secondly that the strength of a finished part be improved through discrete fiber inclusion to expand the range of applicability.

The goal of this thesis is to provide a basis for large scale FFF through experimental work focused on parametrization; to examine several optimizable deposition parameters such as nozzle height, platform speed, and screw RPM and determine the effects of these parameters on bead geometry. Effects to be analyzed include: 1) warping, the tendency of an FFF printed part to warp as it cools due to a combination of thermal gradients and thermal expansion, creating irregular bead shapes;

2) voids, an effect of the FFF process where printed beads are not perfectly rectangular in cross section, causing beads printed side by side to have gaps; and 3) sensitivity of polymers to the deposition process, by examining the effects of altering deposition parameters on the geometry of printed beads. The effect of fiber inclusions are also examined in this study, by comparing polymers with and without inclusions to determine what effects fibers have on the deposition process.

Large scale FFF is currently in the nascent stages, with little established research and few published papers on the subject. Most of the existing research has been conducted by Oak Ridge National Laboratory (Oak Ridge, TN), including a prototype large scale system on a Computerized Numerical Control (CNC) gantry system that was used to print the chassis of a car at the 2014 IMTS conference [4]. Oak Ridge used a carbon fiber reinforced ABS polymeric composite to print the car chassis in 44 hours, with the final printed prototype demonstrating the possibility of successfully implementing large scale FFF into industrial manufacturing. Other advances in large scale FFF include construction cement and wall applications, and fiber reinforcement research, which will be further examined in Chapter Two. With so little existing research in large scale FFF, it is imperative to fully understand the process before successful parts can be achieved. It is necessary to understand the key differences between small and large scale systems, as well as how aspects of the large scale system affect printed parts.

In this thesis, a large scale FFF system is constructed with two main components: (1), a single screw polymer extruder that provides a steady stream of melted thermoplastic polymer in place of the filament/heater section found on small scale systems, and (2), a two-axis automated build platform to simulate the FFF polymer

deposition process. This system is then analyzed through parameterization studies by manipulating screw RPM, nozzle height, table speed, and polymer type, to determine the feasibility of large scale FFF, and furthermore to define acceptable parameters at which this system can produce successfully printed parts. Beads are printed on the platform at various settings of these parameters, and cross sections are taken from these beads that are imaged and stored as data to be analyzed. Geometry metrics including area, aspect ratio, shape compactness, swell ratio, convexity, and compactness are used to determine optimum bead shapes that produce the best prints to avoid common FFF problems such as warping and voids.

1.2 Order of Thesis

Chapter One presents the reader with an introduction into the thesis topic, including motivation for the current work and an overview of the research path. Chapter Two provides an in-depth analysis of existing research and scholarly articles on topics pertaining to the existing research, including descriptions of various additive manufacturing technologies, typical FFF materials and their properties, an examination of processing parameters, large scale adaptations, fiber reinforcement, and process deposition dynamics. Chapter Three gives a thorough description of the experimental process, including system modifications, sample preparation, and processing parameters. Chapter Four establishes the method by which samples are analyzed, beginning with processing samples into data followed by analyzing the data with geometry metrics to determine suitability for the FFF process. Chapter Five presents conclusions based on the data analysis, an overall discussion on the research findings, and recommendations for further study.

CHAPTER TWO

Literature Review

Additive manufacturing (AM), specifically Fused Filament Fabrication (FFF), has seen significant advancement over the past two decades. A large portion of the literature on AM focuses on optimization of process parameters to generate better printed parts. Little attention has been given to fiber reinforcement of FFF parts, which is desired in the field of FFF to move the process from a prototyping technology to a manufacturing tool. Understanding the process parameters of FFF in the presence of reinforcing fibers is crucial because these parameters influence fiber orientation, ultimately changing the dimensional stability, strength, and stiffness of the part. Fiber orientation itself is a decades old theory that has been well studied and analyzed, leading to a large number of resources on the prediction, measurement, and analysis of fibers in a polymer melt. Furthermore, the geometric influence of the FFF nozzle on polymer flow has been evaluated to understand the influence of geometry on fiber orientation through fiber orientation models.

2.1 Fused Filament Fabrication

Decades ago, part production involved custom creations by artisans at the request of a consumer. While this process generated high quality parts, it did not lend itself to high production rates [5]. The innovation of manufacturing tooling afforded increased production by allowing consecutive parts to be made from the same base tools, which further increased innovations in dimensional stability and interchangeable parts.

However, these innovations led to another, less agreeable effect in that customizable parts diminished in favor of mass production. Further development in manufacturing led to technologies such as injection molding, die casting, and machining, all of which require specialized tools with limits on complexity and iteration. In this way, AM offers a return to the historical availability of highly custom parts through the potential to significantly lower costs of tooling, or eliminate the need for tooling altogether. AM is also a highly repeatable process, producing reliably consistent parts of high quality.

AM is a new, and therefore not fully understood, manufacturing method. More traditional processes such as injection molding dominate the plastics manufacturing industry, and it is for these processes that AM seeks to provide a potential alternative. For example, in injection molding, a mold for the part is required that can cost thousands of dollars, not to mention the actual injection molding machine which can cost millions of dollars [5]. Given that these molds are so expense, the design iteration process is constrained from a cost/benefit standpoint, and as a result it is difficult for molds to accommodate optimized parts. Custom parts manufacturing is the golden standard for additive manufacturing, the possibility that optimized and complex parts can be made by completely bypassing the need for expensive tooling, using a method where design iteration is comparably inexpensive and custom parts are not only possible but encouraged. In addition to iteration and cost benefits, there is also no added cost for complexity and customization.

2.1.1 Overview of Technologies

AM is a broad collection of manufacturing technologies that has grown in popularity. These technologies use a wide range of materials, concepts, and iterations to

fabricate a final product. AM processes also allow a greater range of applicability based on the combination of technologies, such as the use of two or more materials to increase a part's functionality. A few common AM processes are described in this section.

Stereolithography (SL) is an AM method that uses a photosensitive fluid monomer resin that solidifies when exposed to ultraviolet (UV) light [6]. A laser traces a path on the top layer of resin, solidifying a pattern at the surface that forms a layer of the part. The build platform is lowered, and the subsequent layer laser-traced, building from the bottom up. Due to scattering of the light beam in the resin, the laser fully reacts resin at the surface, with reactions decreasing with depth into the fluid, resulting in a parabolic bead shape. The SL process is time consuming due to the presence of liquid as the building medium; after each layer, the part is lowered for the next layer, but the lowering motion creates waves in the fluid, requiring the process to wait for these waves to settle before beginning the next layer. Parts are then placed in a UV oven for several hours to ensure that they are fully cured. In addition, hollow parts are impossible to create without allowing for drainage from the center of a part, and after a part is completed any excess fluid is either trapped in the part due to poor part design, or drained from intentional voids. Dimensional stability in SL parts is affected by the accuracy of layer depth, which is directly related to the variability of initial layer coating thicknesses.

Selective laser sintering (SLS) uses a powder instead of a fluid. In a process similar to SL, grains are fused together by a CO_2 laser that traces the pattern of the current layer. In both SL and SLS technologies, excess material remains in the print volume until the part has finished manufacturing, providing support for overhanging geometry and allowing for more part complexity than methods that do not provide

support material. However, trapped volume has the same effect in SLS as in SL, where parts require draining excess volume, or for sealed geometries the excess material is forever trapped within the part. Materials for SLS are cheaper and more readily available than those for SL, as any material that can be reduced to a fine powder and fused with heat has potential to be used in SLS, allowing for a wide spectrum of part properties depending on the powder material. Similar to SL, SLS parts are also time consuming to produce. While there isn't a wait between layer production for SLS because the material is solid and doesn't produce waves, the entire SLS chamber is heated to slightly below the fusion temperature of the powder medium, and the chamber must be slowly cooled after production to ensure the part retains dimensional stability without warping or shrinking due to thermal gradients and expansion. Additionally, the build chamber requires a sealed nitrogen atmosphere, making SLS machines expensive though the materials may be inexpensive.

Laminated object manufacturing (LOM) rolls a sheet of laminate over the build plate, which is then cut in a layer pattern with a laser refined to cut the thickness of the layer. Excess laminate is cut into small pieces, but not removed, to provide support material before being removed at the end. A new sheet of laminate is drawn over the top, and the process continues. Once again, there is the presence of trapped volumes inside the part that creates a waste of material, the inability to create sealed hollow parts, and production of parts that are more dense than necessary. Unlike the previous two technologies, however, the LOM process is much quicker because the cutting laser need only trace the outline of the part instead of tracing rows across the entire surface. Unfortunately, the process combines lasers with paper materials, creating a fire hazard,

yields poor shear strength due to alternating layers of resin and laminate, and creates manufactured parts are difficult to remove from the build plate.

Other rapid prototyping technologies include: Solid ground curing (SGC), which uses a UV-sensitive resin exposed layer by layer through a mask of UV light, ballistic particle manufacturing (BPM), which ejects molten material to impact and fuse with a powder base, and solid foil polymerization (SFP), which is similar to LOM but uses foil instead of a laminate [6]. While this list is certainly not exhaustive, it gives the reader an indication of the inspiration and direction taken in the development of AM technologies, and a basis for the complexity involved in such processes. Descriptions of SL, SLS, and LOM also highlight several common drawbacks present in AM technologies, specifically that many AM processes are time consuming, complicated by trapped volumes, and require expensive, gas-filled enclosures, all of which point toward the benefits of FFF.

FFF is perhaps the most popular AM technology, taking advantage of the low cost of polymers, relative simplicity of the process, and capability for complexity. The input to the FFF process is a computer generated model that is sliced into layers and stored in a file format called stereolithography (STL), which uses triangular prisms to represent the part surface, as shown in Figure 2.1.

Software then interprets the STL file in layers, taking each layer and generating a bead pattern that satisfies the part geometry subject to the dimensional accuracy of the system. Layers are then traced by the extrusion nozzle along the previously generated bead paths until an entire cross-section is “drawn” in polymer, and the build platform moves down to start constructing the next layer (Figure 2.2).

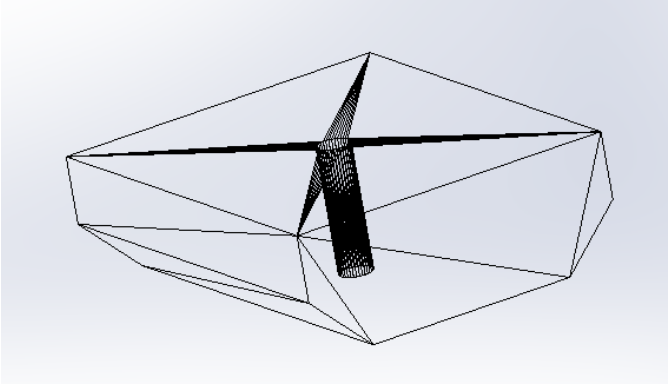

Figure 2.1. Computer model converted to STL with center hole estimated using triangles.

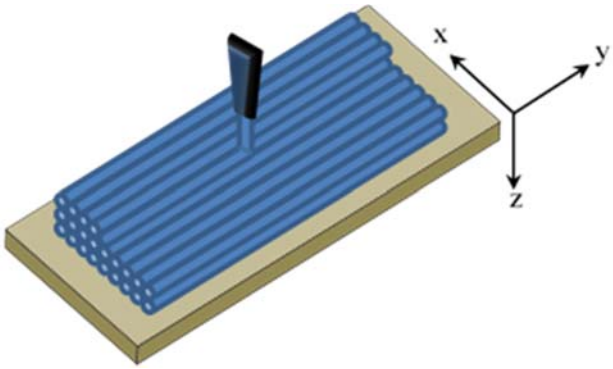

Figure 2.2. Bead deposition pattern on build platform.

If required, support material is printed so that subsequent layers have a solid base to print on top of, but parts can often be oriented to build with little to no support material. The lack of support material is one beneficial aspect of FFF over other processes such as SLS and LOM, providing FFF designers with the ability to create hollow parts without the need to drain trapped volumes. Other benefits over comparable AM technologies include not requiring a specialized printing enclosure atmosphere and lack of necessary curing after the part is printed, reducing production time.

However, being such a new technology, many aspects of FFF still require attention to make the process viable as a true manufacturing method. FFF parts suffer from stair-casing, which results from having a finite number of layers, and highly detracts from surface finish [7], [8]. Polymer from previous layers cools quickly, resulting in a decreased ability for the current layer to bond through polymer chain entanglement with existing layers. Furthermore, bead cross sections are not rectangular in shape, resulting in voids in the finished part that significantly reduce part strength. Bead width constrains dimensional accuracy, making it impossible to print features smaller than the size of the bead itself, and causing layers that are printed with only a few beads to be less dimensionally stable than those printed with many layers [9]. Polymers have high coefficients of thermal expansion (CTEs), which cause a contraction of the material as the polymer cools, causing the part to shrink and warp, reducing dimensionality accuracy and part functionality. Even with the production of a perfect part, an FFF part is still being manufactured with a polymer, and therefore has the strength and stiffness characteristics of that polymer. These issues necessitate knowledge of how process parameters will reduce or eliminate such deficiencies in the FFF process, and therefore improve the overall potential for manufacturing capability.

A discussion by Salonitis [10] outlines several emerging possibilities for FFF using multifunctional materials, including the addition of reinforcement particles to a material matrix. He also describes “smart” composites with embedded sensing electronics to detect damage, and the design of wiring into composites to save volume and mass. Other potential areas of research mentioned in his study include thermal storage, self-healing, and electromagnetic shielding.

2.1.2 Fused Filament Fabrication Materials

Materials development is highly important to FFF, as material properties must meet specific part requirements to take full advantage of the process. Polymers, for example, must have acceptable ranges of thermal properties. A material that has a high processing temperature, slightly above its glass transition temperature, requires a high amount of energy to heat and process, and may also require processing within a specially heated chamber. Glass transition temperatures (T_g) must also be in a specific range depending on application, which due to potential material changes near T_g can cause undesired effects if the temperature of the part reaches T_g. There are other desirable polymer traits for FFF use, including polymers with a low CTE that reduce warping as a part cools, and high strength and stiffness properties that are application dependent. Based on these criteria, several thermoplastic polymers have been developed for use in FFF processes.

One of the most prominent FFF polymers is acrylonitrile-butadiene-styrene (ABS), a thermoplastic commonly used in injection molding and extrusion. The properties of ABS are well known, the material is currently used in traditional manufacturing to make products such as Legos [11], and is popular for a wide variety of plastics applications. The glass transition temperature of ABS is approximately 105°C and has a processing temperature range of 220-240°C, placing it well within the range of low energy requirements compared to other AM processes. However, ABS also has a high CTE that can cause warping, and is slightly brittle compared to other polymer materials [12]. A study by Rodriguez [13] examined the mechanical properties of FFF

processed ABS parts, and found their strength and properties to be within the desired range for application.

Poly-lactic acid (PLA) is another widely used FFF material, which like ABS is commonly used in injection molding and extrusion. PLA is less brittle than ABS [12], and has the added benefit of being biodegradable, which makes it highly suitable for FFF biocomposite applications [14]. By making surgical implants from PLA, the polymer implant will gradually degrade inside the body, allowing the body to progressively accept the load from the supportive implant, and also removing the need for a second surgery to remove the implant. PLA's CTE is also lower than ABS, with processing temperatures in the same 220-240°C range. Other biopolymers being researched for FFF application include polycaprolactone (PCL) [15], polyglycolic acid (PGA) [16], and other mers created using derivatives of lactic acid.

Several other common thermoplastics and extrusion materials are applicable to FFF as well, such as polycarbonate (PC) and polypropylene (PP), which despite less favorable mechanical properties are included due to their low material cost and ease of processing characteristics [17]–[20]. Nylon is also in development as an FFF material for its high impact and fracture-resistant properties [21].

Other polymers are being specifically developed for 3D printing to take advantage of the high degree of bead alignment and need for bonding between layers. Pellets with added fibers increase properties in the direction of fiber orientation, with the added anticipation of fibers crossing bead boundaries to form better bead-to-bead bonds. An example of a fiber-reinforced FFF material is fiberglass-filled polypropylene, currently being used in fiber orientation research [22]. Other research studies combine several

polymers, such as linear low density polyethylene (LLDPE) into ABS to improve flexibility [23]. A product by Eastman called Amphora™ [24] is in development specifically for AM, which is low-odor, has a high degree of dimensional stability, and is easy to process.

2.1.3 Process Parameters and Development

The parameters of FFF are highly customizable, which allows for multiple variable optimization of the deposition process, but also leads to convolution of the effects of each parameter on the final product. With so much possible variation, many studies have sought to find an optimized process parameter system that will minimize the negative effects of FFF, such as warping, dimensional instability, and voids, and produce the highest possible quality part.

In a study by Rodriguez, et al. [13], variations on printed features were examined based on changes in the processing parameters of a Stratasys FFF1600 Modeler. The study manipulated nine parameters:

- Extrusion temperature
- Envelope temperature
- Bead gap
- Flow rate
- Nozzle height increment
- Nozzle speed
- Laydown path
- Layer to layer angle
- Layer to layer translation

Results from Rodriguez's study suggest several ways to improve the quality of prints. A negative bead gap, defined as the width of a printed bead minus the distance between beads, allows the polymer to better fill voids during printing, resulting in a higher part density as well as better layer to layer adhesion. Higher flow rates also reduce gap sizes, allowing polymer to fill in larger areas during printing.

Sun, et al. [25] reviewed the effects of similar processing conditions on inter-layer bonding of polymer filaments. Key parameters from this study included an analysis of the effect of deposition on heat dissipation, and the resulting cooling rate of previous layers. Results from Sun's analysis suggest that allowing the material to cool before coming back to the area to print a new layer is beneficial to reduce defects in geometry. Enclosed build volume temperatures, known as envelope temperatures, were also studied and were found to have a significant effect on layer to layer adhesion, as the previously printed layers remain at a higher temperature and are therefore more conducive to bonding with the current layer by polymer strand entanglement. Convection within the envelope also had some effect on inter-layer bonding, but can be included in the overall state of envelope conditions.

Gray, et al. [26] studied the effects of processing parameters specifically on fiber reinforced FFF parts. Similar to other studies mentioned, varied parameters included processing temperature and laydown pattern. Gray found that lower concentrations of fibers could produce higher strength parts under the right conditions, and furthermore that altering laydown path between layers, like in FFF printing, creates stronger parts.

Concentrating on applying FFF to tooling, Garg, et al. [27] examined process parameters for suitability in production of manufacturing patterns. Dimensionality was

the main factor in determining viability, while print orientation also affected the final part. He concluded that the FFF printing process produces consistent parts which, when optimized using various parameters, can be used in the production of patterns for casting applications.

Roberson, et al. [17] conducted a study aimed to produce deposition materials with specific properties. Desirable properties not generally seen in FFF included electrical conductivity and recyclability. The strategy was to use existing materials as a basis for mixtures that could take advantage of key aspects of each of the materials. Material combination is becoming more common as researchers begin to gear specific materials to applications rather than using "off the shelf" materials for a variety of applications.

2.1.4 Material Properties

Mechanical properties of FFF parts are a function of processing parameters. There is, however, merit in the comparison of FFF optimally printed parts to their current counterparts in industry, specifically injection molded and extruded parts. It is also important to note that the FFF process applies inherent alignment properties to finished parts due to the fabrication process involving beads laid down in patterns. As implied by the presence of air gaps between beads and layers, the strength of a part along the axis of a bead will be stronger than the strength of a part perpendicular to a bead. Critical to the optimization of process parameters is determining how to lower the transverse strength deficit and thereby increase mechanical properties of the printed part.

Masood, et al. [19] conducted a study on the difference between polycarbonate FFF printed parts and comparable injection molded parts. By altering process parameters

such as air gap, layer offset angle, and bead width, the objective was to optimize these parameters for part strength. Each parameter was assigned three levels, and the subsequent strength effects analyzed by tensile testing. It was determined that FFF processed polycarbonate parts fall in the 70-75% range of tensile strength compared to injection molded tensile bars. However, the scope of Masood's study did not take into account the varying properties within a part based on print orientation and print path.

Ahn, et al. [28] acknowledged the anisotropic properties of ABS FFF parts and further sought to characterize those properties based on build parameters using tensile and compressive strengths. Both air gap and bead orientation were found to significantly affect strength, and both parameters were studied further to correlate anisotropy to these parameters. In the FFF process, bead direction can be linked to the strongest local axis of the part; a larger air gap increases gaps in the final part, which intuitively suggests large effects on part strength based on print orientation. FFF parts were found to have 10-75% tensile strength compared to injection molded parts dependent on print parameters, which is consistent with Masood [19], [28]. From these results, printing guidelines were established to increase desired part properties:

- Orient build so that load is applied axially along the majority of beads
- Radii contain stress concentrations due to limits of FFF dimensionality, which does not allow load to be distributed along curves
- Negative air gap increases strength and stiffness by decreasing gaps between beads and layers
- Small bead widths increase build time but also improve surface finish

Another study by Ahn [29] applied classical lamination theory to FFF prints to characterize bead orientation compared to tensile strength. Individual layers of a part were modeled as lamina in plane stress, and stresses were computed to determine applicable forces and moments. Failure of each lamina was then calculated using the Tsai-Wu failure criterion, and material properties of ABS FFF were taken from the previous study as inputs for the model [28]. The classical lamination method proved effective for predicting failure from bead angle, suggesting that further development of failure theory could improve the model's predictive ability. Hill [18] also examined failure relative to bead angle, and concluded that while parts become significantly weaker when all beads are deposited uniaxially, the FFF process takes advantage of inter-layer angle changes to avoid exacerbating the anisotropy problem, and parts printed using this offset have optimized strength in all directions perpendicular to the build plate.

Surface roughness, also called stair-casing, is another issue inherent to FFF due to the approximation of geometries using layers. Small part features suffer from layer width estimates that reduce the suitability of FFF parts for high accuracy applications. Surface roughness effects are most obvious at the surface of the part; a solution to the stair-casing problem would allow the technology to gain a foothold in manufacturing by achieving similar dimensionality to injection molding and extrusion parts. Armillotta [30] studied the resolution of part features as a function of their relative size to bead width. Based on his study, features that are approximated with ten or more beads maintain shapes closely related to the original model. Below the threshold of ten beads, features begin to lose resolution due to stair-stepping. Ideally, an FFF manufactured part should not contain features lower than the resolution of its smallest bead size, to avoid poor reproduction of

features. Another study by Boschetto [31] also predicted surface roughness. A program was created to analyze a three-dimensional part prior to printing, which optimized the part orientation and build direction for minimal surface roughness. By using part orientation optimization as a design tool, it was possible to meet specific roughness parameters for the part by changing print orientation.

2.1.5 Large Scale Adaptation

Of particular interest in transitioning FFF from a prototyping to manufacturing process is to increase the scale of buildable parts. Current FFF technologies limit the size of printable parts based on the build volume of their gantry system, feasibility of material to large scale application, print time, and other limiting factors. However, FFF has caught the interest of large scale manufacturers, such as the automotive and construction industries, with intentions to solve scaling issues and make use of the technology in manufacturing.

Several specific issues arise when trying to increase the scale of FFF printing. One such issue is related to dimensional tolerances of the final product; with the current technology, dimension accuracy of parts is on the order of millimeters, with a typical filament diameter of 1.75 mm and nozzle diameter of 0.4 mm [32]. When printing a larger part, by necessity the material extrusion diameter must be significantly larger to offset the increased volume output; otherwise a print might require weeks or months to fully finish. However, increased extrusion diameter also causes the surface finish of larger parts to increase proportionally with FFF features such as bead shape and warping affecting surfaces. Another issue involves deposition material; projects built on a larger scale would have a tendency to require more structural strength, both to allow bottom

layers to support top layers, and to satisfy potential loading conditions. The benefit from a materials perspective, however, is that with a larger extrusion diameter, there is also a greater potential for materials development and inclusions.

Additionally, there is an issue related to heating and cooling of materials. On a larger scale, if polymers were used, heating the increased diameter polymer requires more energy, which is then stored as heat in the melt flow. While increases in heating energy is a drawback, the real concern is dissipating heat after the polymer has been deposited. Assuming a circular deposition cross section, as the cross section of the deposited bead increases, the volume of the bead increases at a greater rate than the surface area, known as the square-cube problem (Figure 2.3). In FFF, the exponential increase of volume to surface area affects the ability of an FFF part to cool before the next layer is deposited because convective cooling is directly related to surface area.

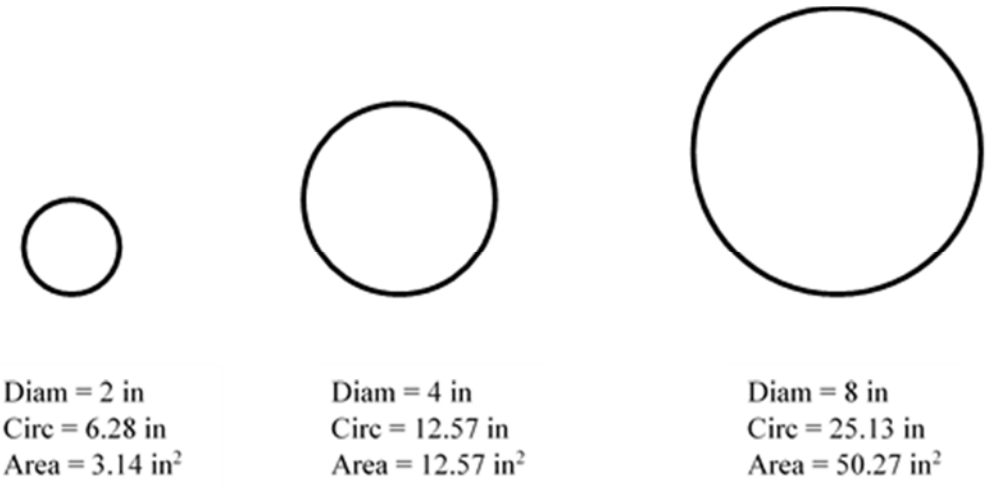

Figure 2.3. Illustration of the square-cube problem.

With volume increasing faster than surface area, large-scale deposition begins to have difficulty using natural convection to solidify layers before a new layer is laid on

top of the previous. If excess heat is still present when the next layer is deposited, the lower layers cannot sufficiently support the upper layers, and the part begins to sag under its own mass. The reverse theory is also a problem, given that bonding between layers is most effective if the new layer, as it is deposited, slightly softens and bonds with the previous layer, allowing polymer chains to cross the layer boundaries. In a larger print, if the deposition nozzle takes too long to make a complete cycle, the previous layers might already be fully cooled to room temperature and the new layer will not bond as well.

The automotive industry is interested in FFF technology for several reasons, including cheaper availability of polymer materials compared to metals, and the lightweight characteristics of polymers. If the FFF process can be applied to manufacturing vehicle chassis, the materials cost and the fuel consumption of a vehicle will decrease due to a drastic decrease in total mass. BMW has begun to manufacture the passenger compartments of the i-series electric vehicles using a carbon fiber woven composite, taking advantage of the lightweight design and fiber reinforcement properties [33]. The difficulty with using woven composites is molding the carbon fiber weave into the chassis shape, requiring a wide range of tooling that somewhat offsets the production cost savings.

Oak Ridge National Laboratory is working on composite-based car chassis fabricated with large scale AM. In 2014, a demonstration using an FFF gantry system printed a car body during the annual International Manufacturing and Technology Show (IMTS) in Chicago, after which the engine, wheels, and other components of the car were added, and the finished “Strati” was driven off the showroom floor [4]. Defects in the production of the Strati, such as layer delaminations, warping, and poor surface finish

suggest that large scale FFF needs further refinement, but the success of a 3D printed car proves that the process is possible and promising.

Construction-oriented technologies based on small scale FFF are currently being researched, with focuses on on-site piecewise construction and foundation fabrication. In August 2015, researchers in Tokyo used a camera guided deposition system to construct a freeform pavilion out of a composite adhesive/chopstick mixture [34], displaying both the potential for FFF in construction applications as well as the possibilities for a broader range of material composition. Another construction based research effort concentrated on concrete printing, with applications applied to laying foundation and reducing build time [35]. The process of concrete printing showed a freedom of design similar to that of small-scale FFF, with contours and complex shapes easily achieved. However, boundaries between layers were highly irregular and required post-processing and finishing to achieve desired smoothness. Therefore, concrete printing is ideal for applications within contained boundaries, such as printing foundation within pre-laid forms, but is currently less applicable to three-dimensional design.

2.2 Fiber Reinforcement

Fiber reinforcement of FFF parts is imperative to increase the properties of printed parts beyond the strength, stiffness, and other performance measures of FFF printing polymers. Increases in material properties due to fiber reinforcement are well documented and acknowledged in injection molding processes, but also introduce a higher level of complexity in the prediction of part properties due to fiber orientation, fiber-matrix bonding, residual stresses, and fiber concentration. Each of these problems

must be addressed when using fiber reinforced materials in FFF, and require further inspection.

2.2.1 Fiber Orientation Background

The first step in understanding the effect of adding fibers to a polymer is to understand the fundamental physics of fiber motion in polymer melt flow, allowing researchers to predict the orientation behavior of fibers under extrusion and deposition conditions, and ultimately to determine the final mechanical properties of a fiber reinforced FFF part.

Primary particle theory for fibers inside a polymer matrix is derived from Jeffery [36]. He describes the periodic motion of ellipsoidal particles in a Newtonian fluid based on previous discoveries by Einstein [37] involving spherical particles. Several assumptions are made by Jeffery that help to simplify the problem to model the behavior of the particle motion in the fluid. It is assumed that the particle motion is slow and that the particle is small and massless, leading to simplified equations of motion. The particle is assumed to be contained within a large volume of fluid that eliminates boundary effects from walls, and no other particles interact with the particle of interest to disturb its motion; in other words, the solutions is assumed to be diluted. These assumptions, along with the equations of motion described for the particle, lead to a coupled system of differential equations. The final form of this theory describes the particle rotating periodically, a phenomenon coined “Jeffery’s Orbit”.

Several problems present themselves when attempting to use Jeffery’s particle motion model; first, that the motion of each particle in a fluid flow must be calculated separately, which becomes increasingly ineffective as the number of particles is

increased; and second, that a fiber does not interact with neighboring fibers, a phenomenon expected in fiber reinforcement. Folgar and Tucker [38] addressed several of these issues by modeling a distribution of fibers. First, experimental observation of shear flows shows a tendency to align fibers in the flow direction instead of the periodic motion suggested by Jeffery's results. This alignment phenomenon is likely due in part to fiber-fiber interactions, which became a focus of Folgar and Tucker's research. The following assumptions were applied to the new model, similar to the assumptions originally made by Jeffery: fibers are uniform and rigid, sufficiently large to avoid atomic scale effects, the fluid is incompressible, particle inertia and buoyancy are negligible, fibers are randomly distributed, and no external forces act on the system [38]. Their new fiber orientation model includes a fiber interaction term, which if set to zero can simplify to Jeffery's Equation in the form of a partial differential equation.

Several new features of fiber modeling are derived from the theory developed by Folgar and Tucker, the first of which is that a steady state fiber distribution for a simple flow criterion (shear flow, elongational flow) is reached in steady flow regardless of prescribed initial conditions, which logically eliminates the steady state periodic rotation proposed by Jeffery. It can also be shown that elongational flows align fibers more highly than shear flows, and that the steady state of the fibers does not completely align in the flow direction. Finally, the fiber interaction coefficient makes the process irreversible, whereas Jeffery's result is a reversible process. Experimental results indicate that the fiber interaction coefficient, as expected, increases with fiber volume ratio as well as aspect ratio [36], [38].

Building on work describing fiber orientation using probability distribution functions, Advani and Tucker [39] introduced "orientation tensors" to improve the fiber orientation modeling process. From Tucker's earlier paper [38], the probability distribution function for fiber orientation $\psi(\theta,\phi)$ is used, where the orientation of a single fiber can be described by two angles in three dimensions. The distribution function must allow both descriptive angles to be periodic by 2*pi. An infinite number of tensors of increasing order may be used to describe the fiber orientation distribution function, where including higher order tensors provides a more accurate representation. Advani and Tucker [39] define many important properties of the tensorial approach to fiber orientation, including their symmetry regardless of increasing order. The question is also posed: what order tensor is sufficient to predict orientation, and further to predict continuum properties based on this tensor? Advani and Tucker suggest that using second-order tensors to describe orientation is sufficient when fibers are not highly aligned, but the more accurate description provided by a fourth-order tensor is needed when fibers become more increasingly aligned.

Experimental results suggest that fiber orientation occurs more slowly than calculated using the method developed by Folgar and Tucker [38]. Wang [40] suggested altering the eigenvalues of the fiber orientation tensor using a scaling factor to get better agreement between results, essentially creating an adjustable constant based on experimental data to add to the fiber orientation model. The fiber orientation model created by Folgar and Tucker [38] uses isotropic rotary diffusion with the addition of the fiber interaction, but this constant affects all terms in the orientation tensor equally, which also fails to match experimental data. To resolve this issue, an anisotropic model is

proposed [41] that provides for different diffusion terms in different coordinate directions, allowing for a total of five terms in the orientation diffusion model that yields improved agreement with experimental orientation measurements.

It is important to note that a fourth order orientation tensor a_{ijkl} is needed to calculate changes in the second order tensor a_{ij} , which demonstrates the need for an estimation of higher order tensors in the calculation of lower order tensors, known as a closure method which were first introduced in Advani and Tucker [39]. Cintra and Tucker examined closure methods [42], proposing a new family of fitted closures based on orthotropic properties of the tensors. More recently, Montgomery-Smith, et al. [43] presented a fast-exact closure method for Jeffery's motion that eliminates the need for approximating higher order tensors and significantly improves the accuracy of fiber orientation calculations. The fast-exact closure method defines two orientation tensors such that higher order tensors can be directly calculated from lower order tensors, allowing for solutions to Jeffery's equation based on the existence of an exact solution without diffusion, but also allowing for the diffusion term to exist in the solution.

The eventual goal of fiber orientation prediction is to be able to predict the material properties of a fiber reinforced composite from a predicted fiber orientation state. The rule of mixtures is mentioned in Chapter One as a method of material property prediction assuming the composite is fabricated using continuous fibers. Other prediction models have been proposed for highly aligned fibers, such as the Halpin-Tsai [3] and Tandon-Weng [44] models. However, these models predict properties only for high alignment orientation states, which is not useful in cases where the orientation state is known but not highly aligned. Further work has been done by Advani, et al. [39] and Jack

and Smith [45], to predict the mechanical properties of a short-fiber reinforced composite given any fiber orientation state. Continued work in mechanical property prediction continues to bridge the gap between fiber orientation and composite properties for short-fiber composite processing.

2.3.3 FFF Fiber Reinforcement

Fiber reinforcement is used extensively in composite manufacturing processes such as injection molding and fiber laminates, and in these industries the inclusion of fibers improves the mechanical properties of the resulting composite. Therefore, the use of fibers in FFF is a natural progression of the technology. Love [46], a researcher at Oak Ridge National Laboratory, briefly discusses the role of carbon fiber in FFF from a manufacturing perspective, outlining the potential benefits and drawbacks of fiber inclusion. For example, short fibers in FFF greatly increase mechanical properties in the direction of the fiber, but properties perpendicular to the fiber direction and along boundary layers remain near the properties of the original polymer, which highlights the importance of design for end-use parts based on loading conditions.

Another important aspect of FFF carbon fiber inclusion is that carbon fibers have a negative coefficient of thermal expansion (CTE), meaning that as carbon fibers increase in temperature, the fiber actually shrinks. As pointed out by Love, et al. [46] in their study on carbon fiber, mixing carbon fibers with a negative CTE and a polymer with a positive CTE can result in a composite with a near-zero CTE, reducing the tendency for a part to warp as it cools and increasing dimensional stability. Given that warping is a primary concern in FFF, inclusions that decrease warping are highly desirable. Carbon fiber inclusion strategy is proven during experimental testing, where a comparison of neat

ABS to 13% carbon fiber filled ABS showed a high degree of warping in the ABS and negligible warping in the fiber-filled ABS [46].

Mechanical properties of FFF composites are discussed by Zhong [23] in an overview of FFF fiber reinforced composites, emphasizing necessary characteristics such as suitable glass transition (T_g) and melt (T_m) temperature ranges, low CTE, and material strength and stiffness, keeping in mind that mechanical properties will be altered by the fibers. In Zhong's study, inclusion of fibers had a notable effect on processing temperatures by increasing the softening temperature. However, at 30% fiber volume fraction the composite material became brittle and was not feasible for filament extrusion. Zhong continued to experiment with different volume fractions, adding LDPE to increase ductility, and successfully achieved extrusion of the composite at ~10% volume fraction after mixing with LDPE.

Extensive research is also being conducted on the effects of the FFF process on composites and fiber orientation, building from knowledge of fiber behavior in injection molding and other plastic production processes. Yasuda, et al. [47] directly studied fiber orientation through an injection molding expansion geometry slit channel, concluding that fibers were highly aligned in the channel leading up to the expansion. Upon reaching the abrupt 1:16 channel expansion, fibers rotated perpendicular to the channel flow. Furthermore, fiber-fiber interaction was found to be highly important at the neck of the expansion due to high fiber angular velocity, and fiber-fiber interactions less significant after the expansion and at the channel boundaries due to low fiber angular velocity and flow velocity.

The injection molding software package Moldflow, a program used to simulate fiber orientation, was implemented by Nixon [48] to study the effects of FFF processing parameters on orientation. One of the primary experimental design variables was nozzle geometry, which varied through convergent, straight, and divergent models. Nixon found that fiber orientation does not change significantly in the liquefier region, and that just before the nozzle the shear flow increases, which helps align the fibers. At the nozzle, the convergent model aligned fibers before leaving the nozzle, suitable for extrusion with a high rate of desired alignment. The straight design caused fibers to unalign slightly, most likely due to end effects of the nozzle exit. Finally, the diverging nozzle produced intricate flow patterns, with volume fraction playing little to no role in orientation due to minimal fiber-fiber interaction. Extension of the flow caused alignment to decrease in the flow direction, appropriate for quasi-isotropic applications.

Work by Heller, et al. [49] specifically studied the effects of the FFF process on fiber orientation, including effects of the nozzle and die swell. Results from this study indicate that the extrusion process has a significant effect on fiber orientation, where fibers are highly aligned in the flow direction within nozzle convergence zone, but fibers decrease in axial alignment as the polymer flow exits the nozzle due to the significant changes in velocity gradients that occur in the die swell.

2.3 Process Dynamics and Effects

A variety of process parameters were discussed in Section 2.1.3 related to the optimization of the FFF process, such as temperature, bead characteristics, extrusion speed, and raster path. With FFF process parameters in mind, this section further examines the FFF process and its effects on deposition parameters, specifically exploring

the dynamics and mechanics of FFF with the goal of fully characterizing the deposition process.

2.3.1 Dynamics

The extrusion head of an FFF printer is divided into two sections; one section where solid filament is drawn into the head with roller gears, and a second section where the filament is heated to a viscous fluid and extruded out of the nozzle. The extrusion process is driven by the roller gears, creating back pressure from the filament to push the liquid polymer through nozzle (Figure 2.4).

The liquefier dynamics of the FFF process were further studied by Bellini [50] to understand and control fluid flow during extrusion. Bellini describes the typical extrusion process, indicating that after the volumetric flowrate is established, the nozzle must deposit an initial bead, to be discarded later, to reach a steady state flow. Acceleration and deceleration of deposition during extrusion is also examined, making note that during these processes it is difficult to guarantee a steady flow rate relative to the platform. For example, if the raster path encounters a corner, edge, or a new layer, the nozzle mechanism must account for these changes in deposition rate while maintaining a constant bead width. Other factors described by Bellini, which serve to further complicate the liquefier dynamics, include:

- Fluid compressibility
- Boundary conditions along the wall including friction, viscosity, and slipping
- Slipping or catching of the filament being fed into the nozzle
- Variable heating applied to melt the thermoplastic
- State change of material inside the nozzle

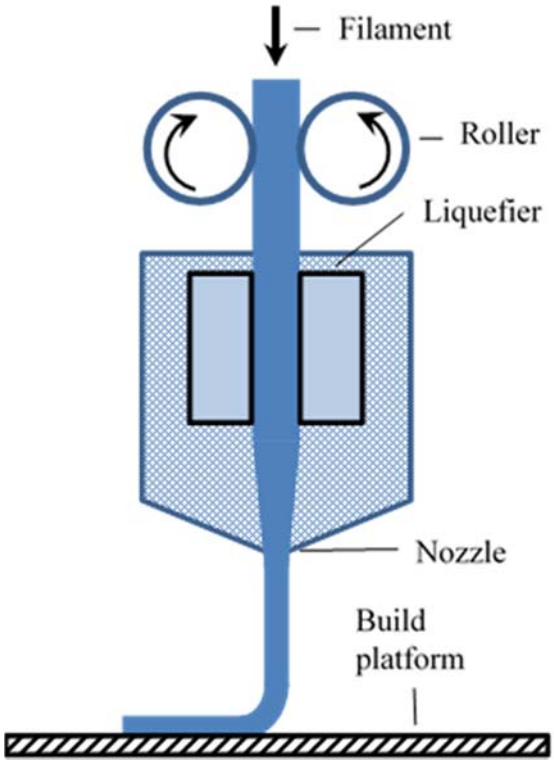

Figure 2.4. Liquefier diagram including filament rollers and nozzle apparatus.

To define the liquefier dynamics, Bellini used two modeling approaches, both a mathematical model and a transfer function. By varying conditions within the model such as gear angular velocity and fluid properties, the flow rate out of the nozzle was measured, and the effects of these varying parameters were shown to significantly affect the resulting polymer flowrate. In both the mathematical model and using the transfer function, the models showed good agreement with experimental results, understanding that the physical system, unlike the models, cannot respond immediately to a step change.

Melt extrusion and liquefier dynamics are also examined by Turner [51] in a review of the design and modeling of FFF processes. The filament feeding mechanism is described in detail, explaining that toothed gears are used to grip the filament and push it into the liquefier with enough pressure to successfully grab the filament without crushing

it. Factors affecting the performance of the feeding system include slipping between the gears and the filament, failure of the solid filament at the top of the feedstock to piston the liquid polymer out of the nozzle, and compression of the filament below the rollers causing buckling. The system further increases in complexity when considering that the feed rate of the extruder varies with changes in nozzle velocity during printing.

The liquefier itself is generally heated using resistive wire coils, kept at a constant temperature using a thermocouple control loop [51]. The heat flux required for the liquefier mechanism is sizable, required to fully melt the thermoplastic over the travel of a few centimeters, creating the opportunity for changes in heat flux to affect the functionality of the extruding head. In general, melt temperature is optimal when the polymer is sufficiently liquid to bond well between layers, but not so hot that the polymer begins to thermally degrade or easily lose shape after deposition. Viscosity and shear rate as a function of temperature also affect performance of the liquefier, with viscosity modeled as a combination of Arrhenius temperature and shear-rate dependent terms [51].

A simplified geometric model of the liquefier is shown in

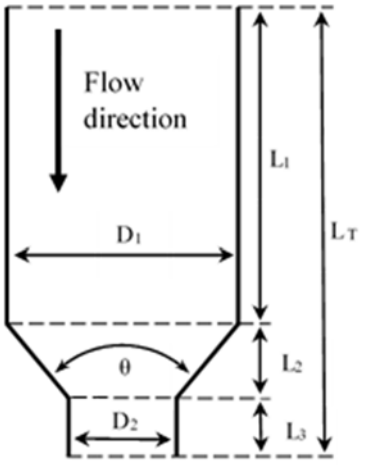

Figure 2.5, divided into three sections as modeled by Turner [51], with design variables including total length, nozzle angle, nozzle exit diameter, and liquefier diameter. The

liquefier diameter is assumed to be the same size as the filament, to best facilitate the piston motion that allows solid filament at the top of the nozzle to push the liquid polymer out of the nozzle. Apart from the diameter constraint, the extrusion nozzle remains available for process optimization.

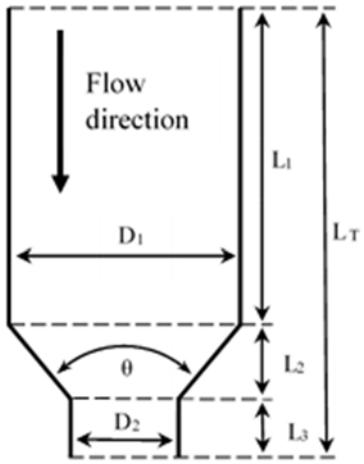

Figure 2.5. Standard liquefier and nozzle geometry for FFF.

Specific liquefier dynamics are further studied by Mostafa, et al. [52] using an ABS/iron compound, focusing on the motion of a compound material passing through the extrusion head. Iron powder was selected to help improve the mechanical and thermal properties of the ABS stock, along with increasing bonding adhesion between polymer layers. Mostafa's main finding was that pressure drops created intermittent flows, potentially caused by increased viscosity and friction effects of the heterogeneous ABS/iron composite. However, pressure drop variations did not affect the liquid flow enough to invalidate the material for FFF processes, and his model successfully demonstrated the process effects of adding particles to the liquefier.

A different approach was taken by Ramanath [15], who specifically studied biopolymer modeling in FFF through the liquefier. The biopolymer PCL was used, and

pressure drops through the liquefier and nozzle were examined to determine feasibility for use in the FFF process. Results determined that PCL was an acceptable FFF biopolymer, with pressure drops in the 20-30% range, within acceptable limits for extrusion.

In a study on FFF material properties, Ahn [28] discussed possible changes to nozzle geometry, noting that each physical nozzle change requires recalibration to determine flow rate. When the polymer bead is homogenous, simply recalculating flowrate is a valid approach, but variations in nozzle geometry with inclusions such as reinforcement fibers could greatly influence orientation state. Therefore, changes in nozzle geometry with complex FFF materials must be more extensively examined than when using pure polymers.

2.3.2 Processing Effects

While many processing conditions can be modified to produce varying results in a final FFF part, several elements of the extrusion process are worth mentioning based on the mechanical processes inherent in part production. One such mechanical aspect is the creation of residual stresses in the thermoplastic, created due to the melting and re-solidifying of the thermoplastic. Gusarov [53] describes residual stresses as the result of contraction of melted zones, which thermally expand when heated and must therefore contract as they cool. In the process of manufacturing an FFF part, print parameters such as raster orientation and part orientation on the build platform can have a significant effect on the generation and magnitude of residual stresses, especially areas of an FFF part with high stress concentrations created by complex features.

A study by Wu [54] investigated the presence of residual stresses in AM steel parts as a result of processing parameters. While Wu's study focused on powder bed fusion technology, his findings are generally applicable to AM processes. The goal was to reduce residual stresses by altering the build pattern, suggesting that the same part manufactured using smaller raster lines with an optimized build pattern can reduce stresses by nearly half. Stress reduction is due mostly to a process called "island scanning," where a large surface area of the part is produced by generating smaller sections in alternating orientations, thereby creating smaller aligned areas with reduced stresses.

The geometrical shape of the bead is also important in understanding the deposition process, as it helps to define the polymer path from the FFF nozzle to the build plate. Jin [55] discusses the path of the filament as it exits the nozzle and makes contact with the build plate, modeling the resulting path with a Tractrix curve with the nozzle at a height of 0.014 mm. It is significant to observe from his study that after leaving the nozzle with cross-section parallel to the build plate, the motion of the extrusion head as well as previous extruded material rotate the filament so that it arrives on the build plate with its cross section perpendicular to the platform.

2.4. Application to Current Work

The previous sections in this literature review have given an outline of the current research in FFF, motivating the use of FFF among other AM technologies. This overview of FFF materials and process parameters emphasizes the importance of fiber inclusions. Unfortunately, there is little current research in the field of large scale FFF, as demonstrated in Section 2.1.5, highlighting a need for research in the area of large scale

FFF to move the technology from prototyping and modeling to industrial manufacturing. This thesis work is focused on contributing to the large scale FFF knowledgebase through parameterization of a large scale system, determining the processing effects and parameters necessary to produce a successful large scale FFF part.

In summary, FFF deposition is a highly complex process that is not only dependent on material, temperature, and process parameters, but is also sensitive to the dynamics of melting a polymer from a solid to a fluid. As solid polymer undergoes a phase change to a viscous liquid, small changes in heat flux, pressure, friction, and other effects can significantly alter deposition.

CHAPTER THREE

Experimental Methods

The focus of Chapter Three is the development of a large scale FFF system, which is designed and developed for materials testing. Then, specific details are given for preparation and printing of samples used in the parametric study described in Chapter Four. Three of the parameters studied relate to the FFF system, specifically table speed, screw RPM, and nozzle height, while the fourth parameter relates to the polymer material used in the deposition process.

3.1 System Design and Improvements

As mentioned in Chapter Two, one of the major changes necessary between small and large scale FFF is the transition from a filament-heating system to an extrusion system. An extruder is necessary to bring high volumes of polymer to melt quickly enough to be used in FFF, requiring a redesign of the deposition phase from existing small scale FFF systems. Once a large scale FFF system has been created, it can be used to examine the process parameters specific to large scale FFF deposition, and conclusions drawn about the technology's scalability.

The large scale FFF system at Baylor University started at the conceptual stage, with several design iterations taking place before a suitable system was reached. Design iterations provided valuable insight into the application of FFF to large scale production, and allowed the FFF system to be specifically modified for its intended applications.

3.1.1 Initial Large Scale FFF Extruder

A C.W. Brabender FE-2000A single screw extruder was used to melt polymer pellets, and convey polymer to the exit nozzle where the extruder lay horizontally

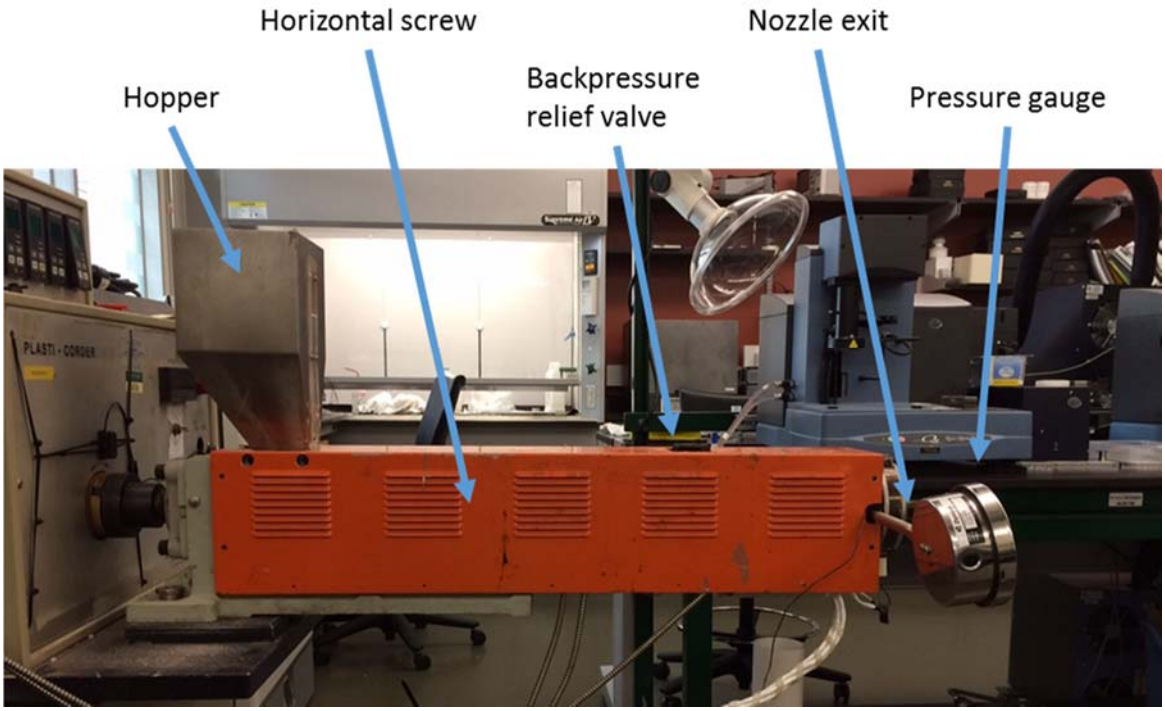

Figure 3.1). Horizontal extrusion created an immediate issue because prints need to be built with material extruding vertically, so a 90° bend was added to turn the extrudate vertically before being extruded (Figure 3.2). The vertical bend is made with copper pipe, which adds approximately 4" to the polymer path, an additional 1" horizontally and 3" vertically. At the end of the vertical bend, pipe threads allow for plugs to be inserted as nozzles, providing users a means to create various nozzle diameters by drilling holes in the plugs.

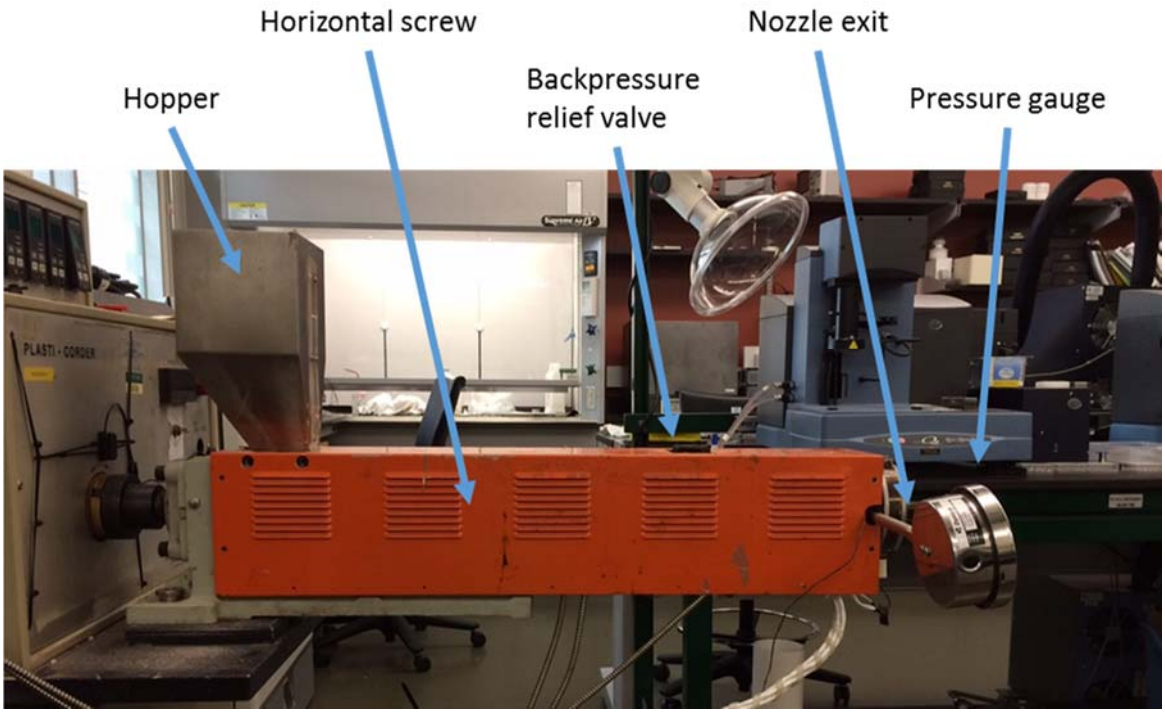

Figure 3.1. Brabender single screw extruder.

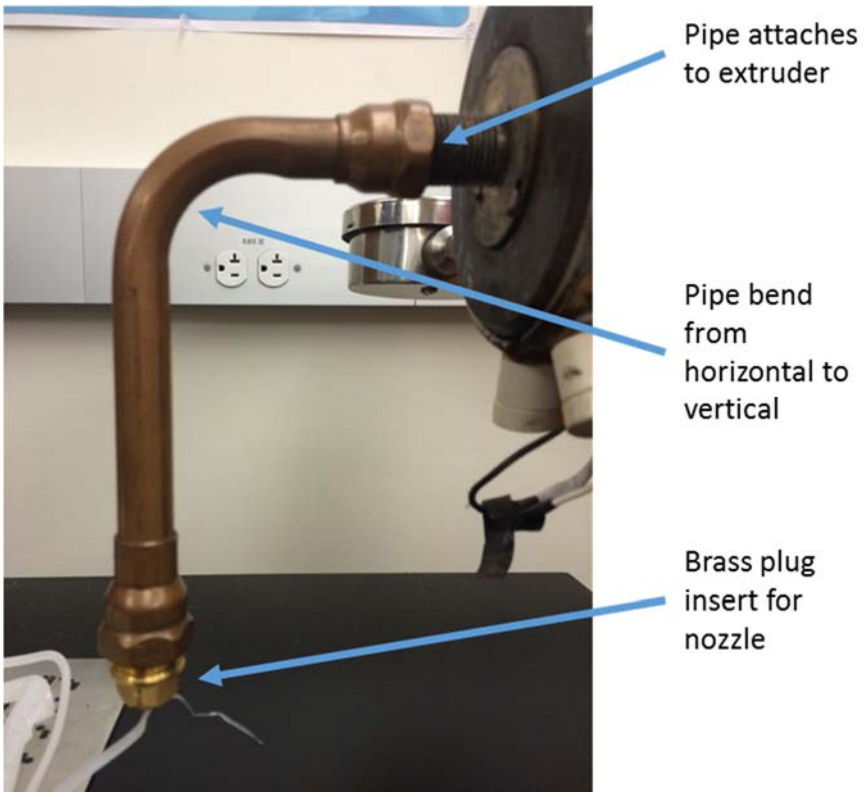

Figure 3.2. Brabender 90° attachment for vertical extrusion.

Using the 90° bend attachment to turn the polymer flow, another problem surfaced: the polymer flow through the nozzle was cooling before exiting, causing a significant amount of back pressure into the screw as well as cooling the polymer flow too much to be useful in an FFF process. To overcome the cooling problem, the nozzle was heated using flexible resistive wiring heat tape with a temperature actuator, as shown in Figure 3.3.

Even with improvements to the Brabender to retrofit it into an FFF extruder, it became apparent that a different piece of equipment would be necessary to create a viable large scale FFF system. Focus turned to finding an extruder that was specifically designed for FFF, which led to a partnership with HapCo Inc. (Hewitt, TX) and the acquisition of the Exon8 Single Screw Extruder [56]. The Exon8 extruder is the same

model used by Oak Ridge National Laboratory to print the Strati car chassis, and was a good fit for the FFF system [4].

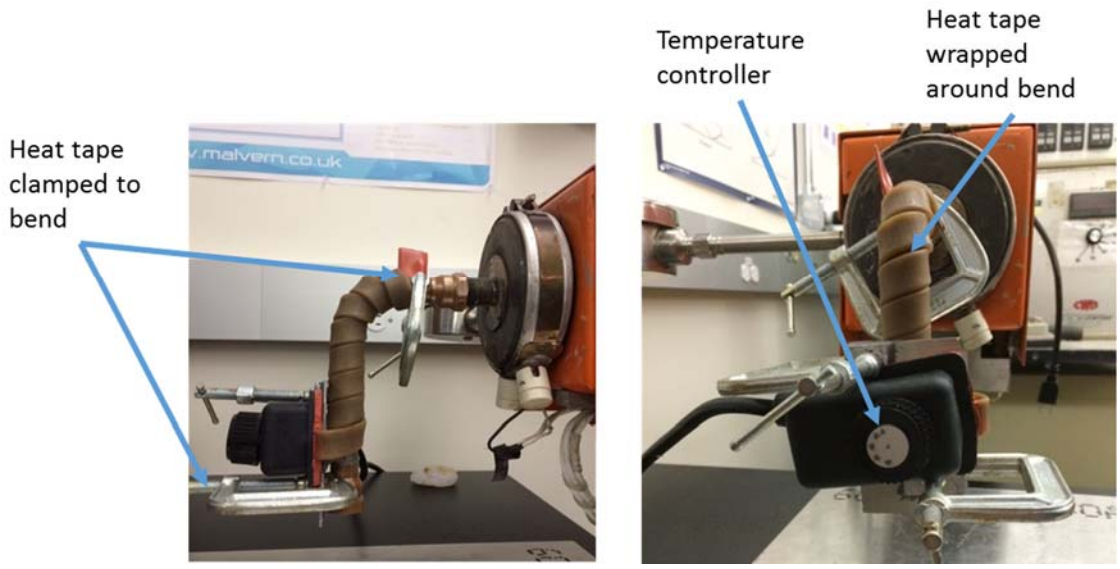

Figure 3.3. Brabender 90° attachment with resistive wiring heat tape.

There are two main aspects to most FFF systems, specifically the extruder feeding region that includes a mechanism to accept polymer, heat the polymer to melt, and extrude the polymer out of a nozzle, and a platform with three degrees of freedom to allow the nozzle to occupy any position relative to the platform within the build volume. During an FFF print, each layer is printed in a horizontal plane until the layer is complete, and upon completion, the third axis is incremented to allow a new layer to be printed on top of the previous layer. FFF systems can accomplish these degrees of freedom in different ways as long as the nozzle and table can change position relative to one another. For example, the MakerBot Replicator 2X uses a nozzle that moves on belts in the *X*- and *Y*-directions, while the platform increments in the *Z*-direction [1]. Alternatively, the computerized numerical control (CNC) system used by Oak Ridge National Labs at

IMTS 2014 moves the nozzle in all three dimensions while holding the build platform stationary. Both of these methods are viable and logical given the relative scale of the systems. For the Replicator 2X, the size of the nozzle and the build volume are both small, and moving one or the other relative to each other is not difficult. However, given the much larger scale of a car chassis (~10 m^3) compared to a single screw extruder (~1 m^3), it logically follows that Oak Ridge would move the relatively small extruder in all three dimensions to avoid having to move the much larger car body.

In our work, an extruder support frame was built to suspend the extruder with a *Z*-axis translation screw to adjust the nozzle height (Figure 3.4). Specific details on the design and operation of the stand can be found in Appendix A, which has a 12 in. adjustment range. During initial testing of the Exon8, several modifications were made to improve the efficiency and processing of the system, as outlined here.

The first adjustment to the Exon8 extruder was to alter the angle of the hopper that feeds pellets into the screw. The initial angle of the hopper was 45°, which created two undesired results: 1) the slanted design did not take full advantage of feeding pressure, where pellets from the top of the hopper push on the pellets below and maximize pressure, and 2) due to the convergent shape of the hopper, some pellets at the bottom of the hopper were actually below the elevation of the feeding hole into the screw, and prevented them from passing into the extruder (Figure 3.5). The hopper feed angle was rotated from 45° to 90° to improve pellet feed pressure and avoid trapped pellets.

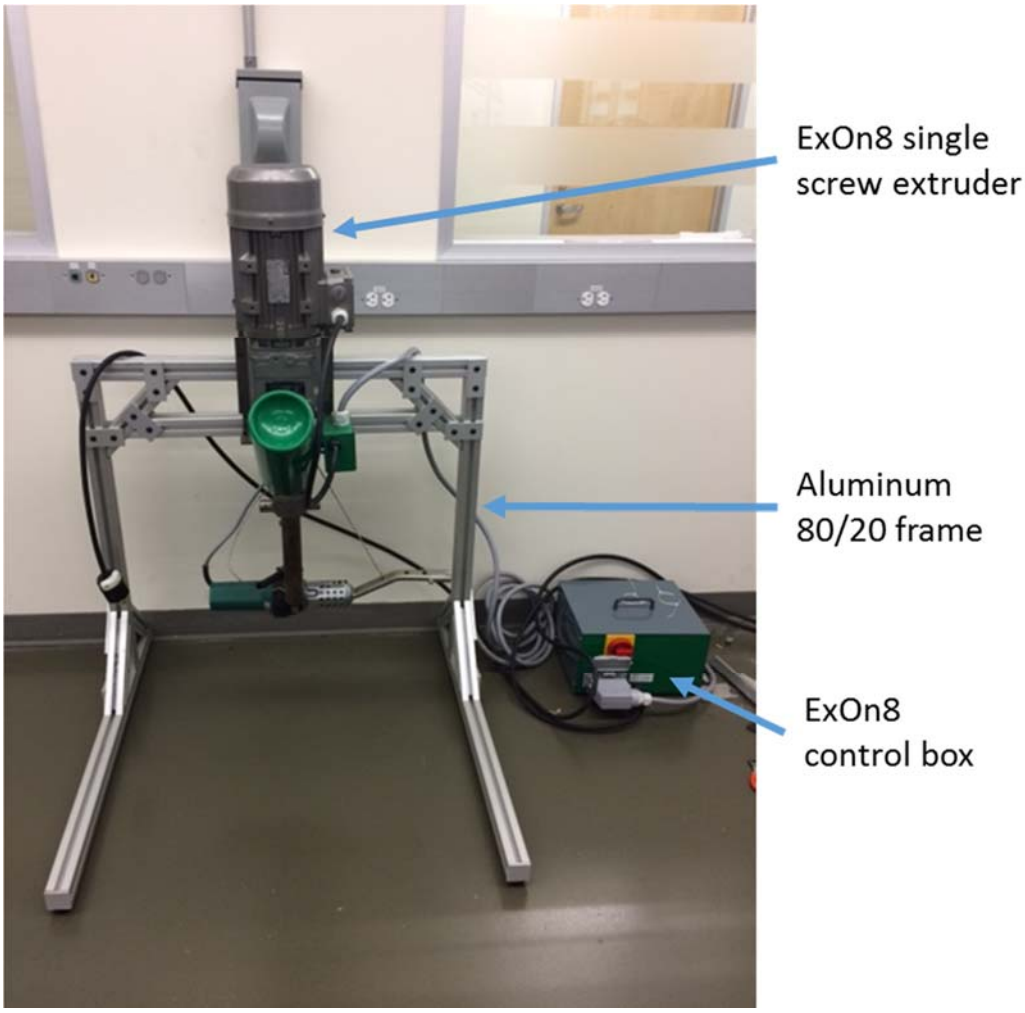

Figure 3.4. Exon8 mounted on suspension stand.

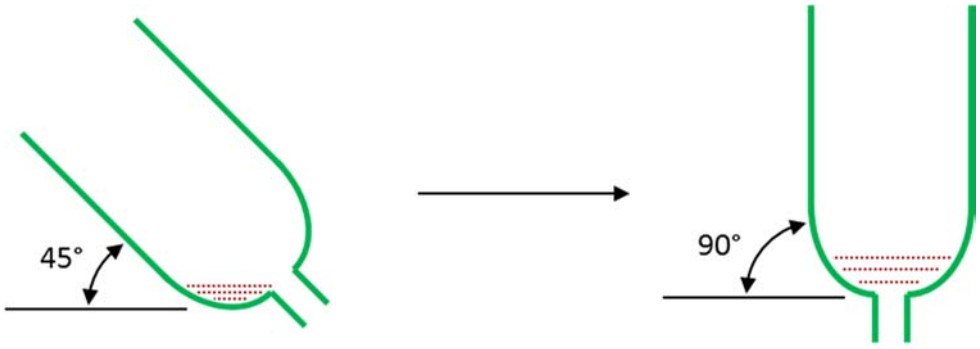

Figure 3.5. Hopper rotated from 45° to 90° to increase feeding pressure and allow all pellets to feed into extruder.

Another adjustment was made to the Exon8 extruder because it was observed that under certain extrusion parameters, the polymer exiting the nozzle had a pulsing effect, where the volumetric flowrate out of the nozzle varied significantly. The pulsing effect was primarily observed while extruding the Amphora™ polymer by Eastman Chemical Company (Kingsport, TN). During Amphora™ extrusion, the pulsing would increase in severity over time, and eventually polymer would stop flowing out of the nozzle even though the screw was still turning. Partially melted pellets were found to clog the entrance to the screw as seen in Figure 3.6.

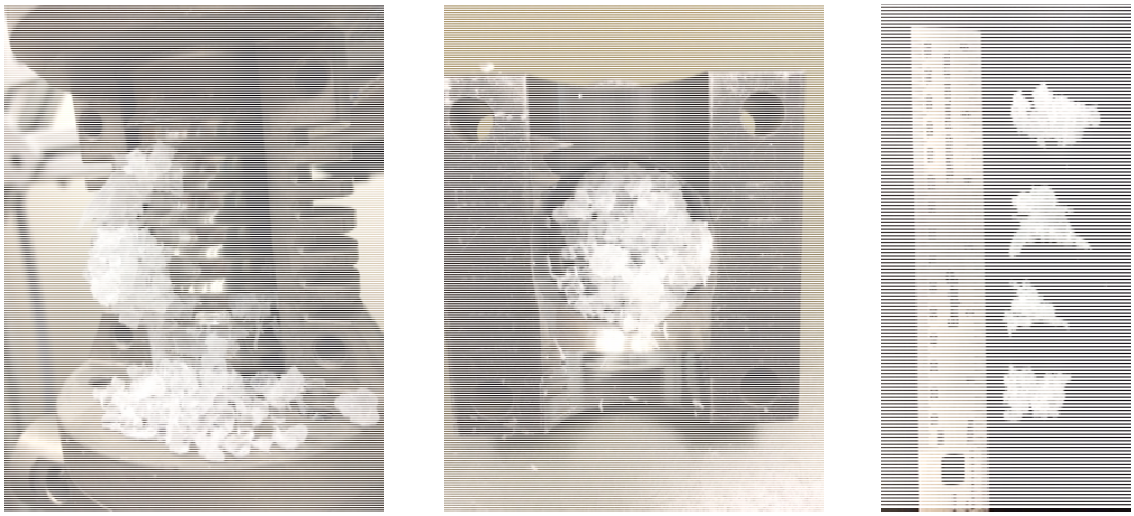

Figure 3.6. Amphora™ polymer clogs in the feeding section of the hopper where it connects to the first flight of the extrusion screw.

Clogs were forming against the first flight of the screw, and as the clogs grew in size, pellets were prevented from entering the extruder. Finally, the clog would become large enough so that no pellets could pass, and the screw would stop extruding polymer. Several attempts were made to resolve this issue, including vibrating the hopper to improve feeding, cooling the top section of the screw where the pellets fed into the

extruder, and inserting a wire into the hopper to agitate the pellets and facilitate flow. Ultimately, the mechanism that created the clogs was found to be excess heat propagating up the length of the screw into the feeding flight, prematurely heating pellets and fusing them together inside the opening of the hopper. It was determined that polymer pellets were not passing through the entry fast enough to avoid clumping, which was causing the screw to "starve" for pellets. It was observed that the cross-sectional area of the feeding tube exit formed an oval shape as it presented itself to the screw, while the cross-sectional area of the screw itself was rectangular in shape. As a result, only a portion of the flight of the screw was being presented with impinging pellets, not taking full advantage of the area available for feeding pellets into the extruder. To increase the area of impinging pellets against the screw flight, small aluminum spacers were placed between the hopper and the screw where the assembly feed tube attaches to the screw housing against the first screw flight (Figure 3.7. (a) Initial oval cross-sectional area of impinging pellets, (b) placement of aluminum spacers, and (c) resulting pellet impingement area.

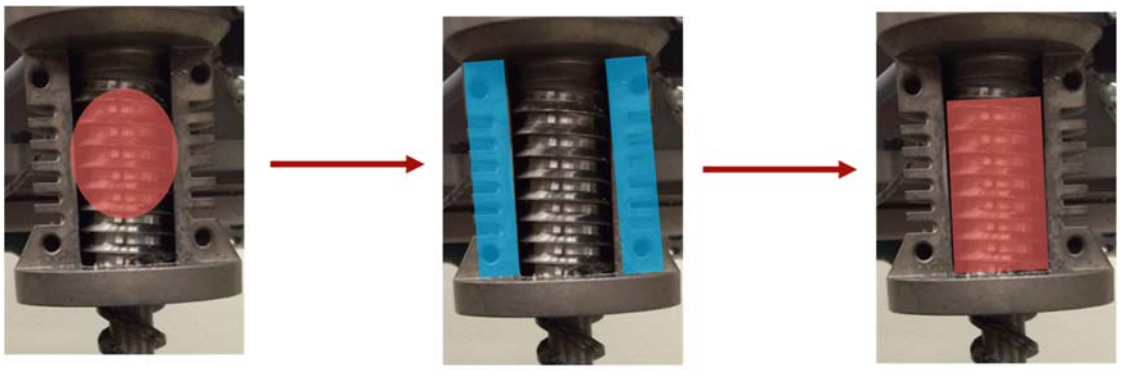

(a) (b) (c)

Figure 3.7. (a) Initial oval cross-sectional area of impinging pellets, (b) placement of aluminum spacers, and (c) resulting pellet impingement area.

3.1.2 Table Design and Improvements

The second aspect of an FFF system is the translation platform. As mentioned in Section 3.1.1, an FFF system requires three dimensions of translation that may be accommodated in different sections of the system. Our FFF system uses two automated translation screws for (*x,y*) movement that are connected to a moving platform. A custom translating build platform was designed and built for this purpose. Our translation platform is controlled by three NEMA 14, 750 RPM, 10.2 in-oz torque stepper motors and an R256 controller for each automated axis. Further specifications for the custom build platform can be found in Appendix A. As with the Exon8 extruder, the platform also underwent several design iterations before achieving full functionality.

The initial proof of concept design only had one automated axis, which was controlled with one stepper motor along 2 ft. of translation screw. The second axis was constructed using drawer slides, which could be moved and locked into position to allow extrusion along any section of the platform (Figure 3.8). The drawer slides proved the concept of the moveable platform, but it quickly became apparent that a second automated axis would significantly improve the functionality of the system, allowing for fully programmable in-plane translation capability. Additionally, the *x*-axis that translates the entire platform as well as the mechanisms for the *y*-axis would occasionally halt because friction would overcome the amount of torque provided by one stepper motor. Adding a second motor on the opposite side of the *x*-axis screw allowed the axis to have twice as much torque and reliably translate without “sticking”. The fully automated system is shown in Figure 3.9. Translation platform with two automatic axes.

The entire translation platform is constructed from 80/20 aluminum extrusion that allows for ease of construction and modification without the need for heavy steel supports and welding [57].

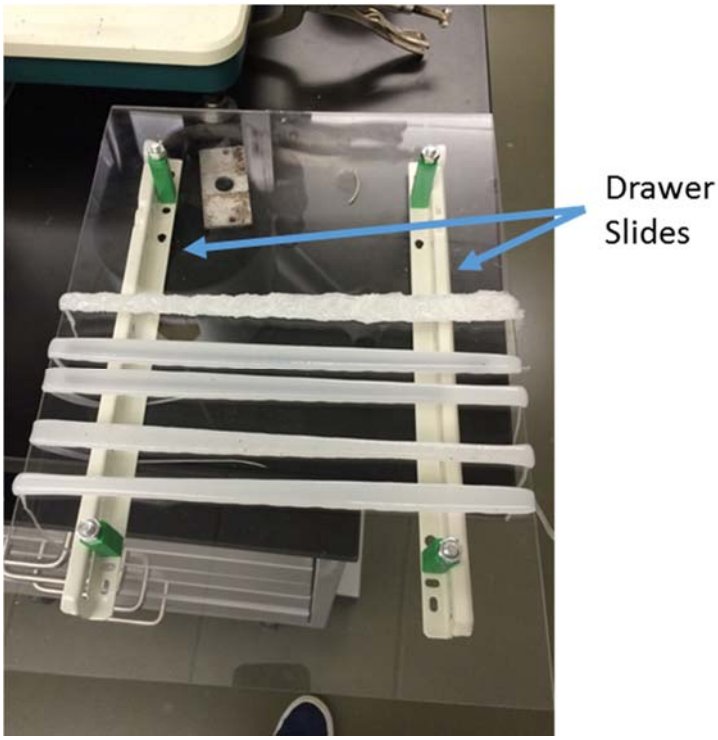

Figure 3.8. Initial platform using drawer slides to translate second axis.

While the 80/20 extrusion had many bracket and attachment components, some custom features for the table were required that presented an opportunity to demonstrate the current performance capabilities of small-scale FFF. To demonstrate the capabilities of small-scale FFF, several components of the automated table were designed in-house using 3D modeling software and then printed on the MakerBot Replicator 2X. A few of these designs are outlined here.

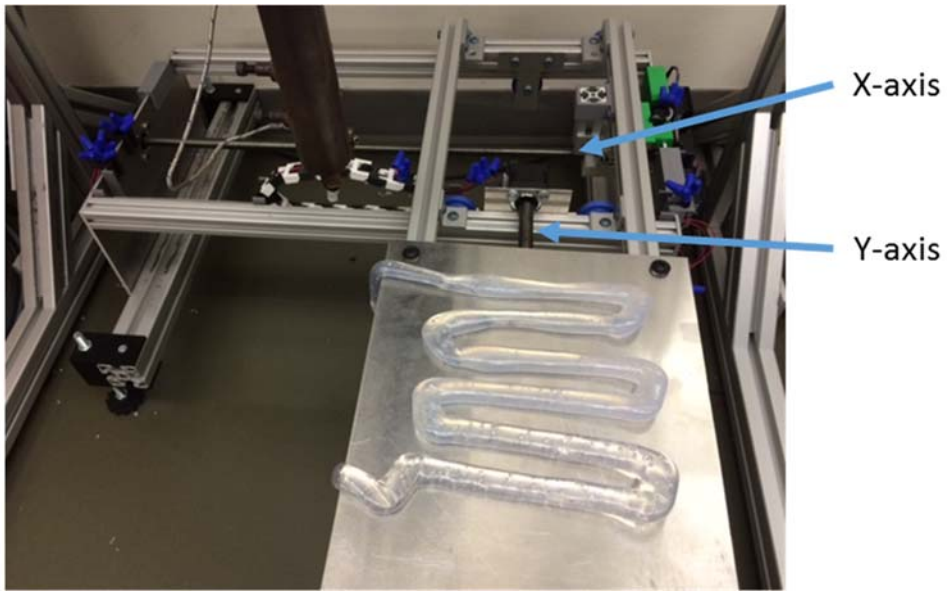

Figure 3.9. Translation platform with two automatic axes.

Custom fixtures were designed and printed to localize wiring on the side wall of the table. FFF printed brackets drape over the aluminum lip of the wall, and electronic components are attached using small screws (Figure 3.10).

The translation screws span a distance of 18 in. each, and are not perfectly axial. Therefore, as they rotate, the path of anything directly attached to the screw is a small circle instead of pure rotation, which can create unnecessary friction when using rigid attachments. To remove added friction, each screw translates only in its primary axis of motion to attachments using a piston design, where the two secondary axes resulting in the small circular motion are allowed to move freely (Figure 3.11). As the screw rotates, the piston moves freely in a sleeve while pushing in the primary direction. The sleeves were also designed and printed on the MakerBot Replicator 2X.

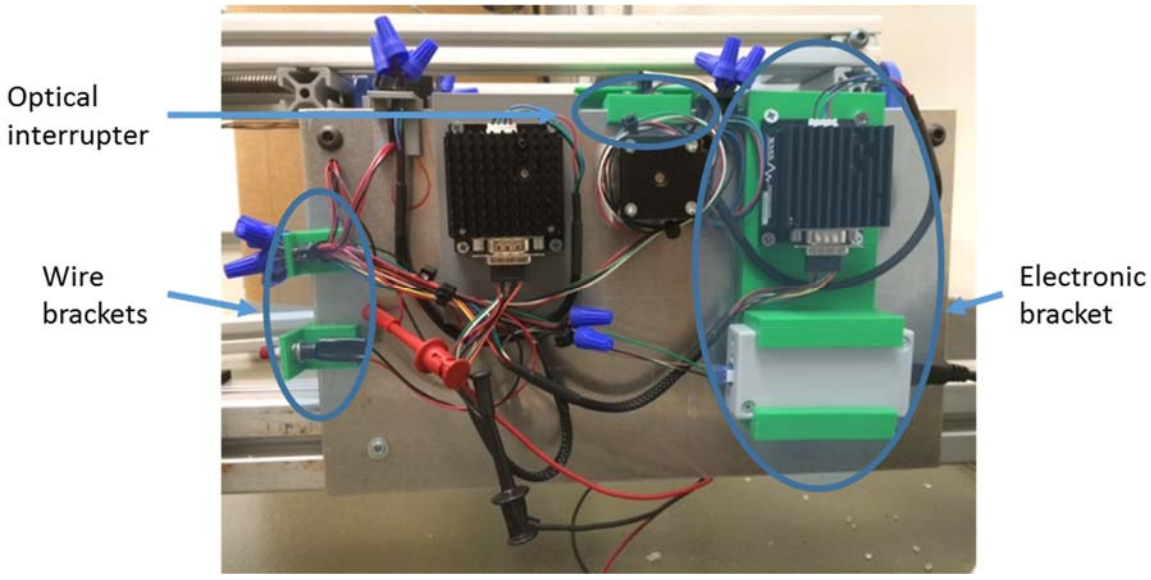

Figure 3.10. Brackets printed on the MakerBot Replicator 2X to attach electronics.

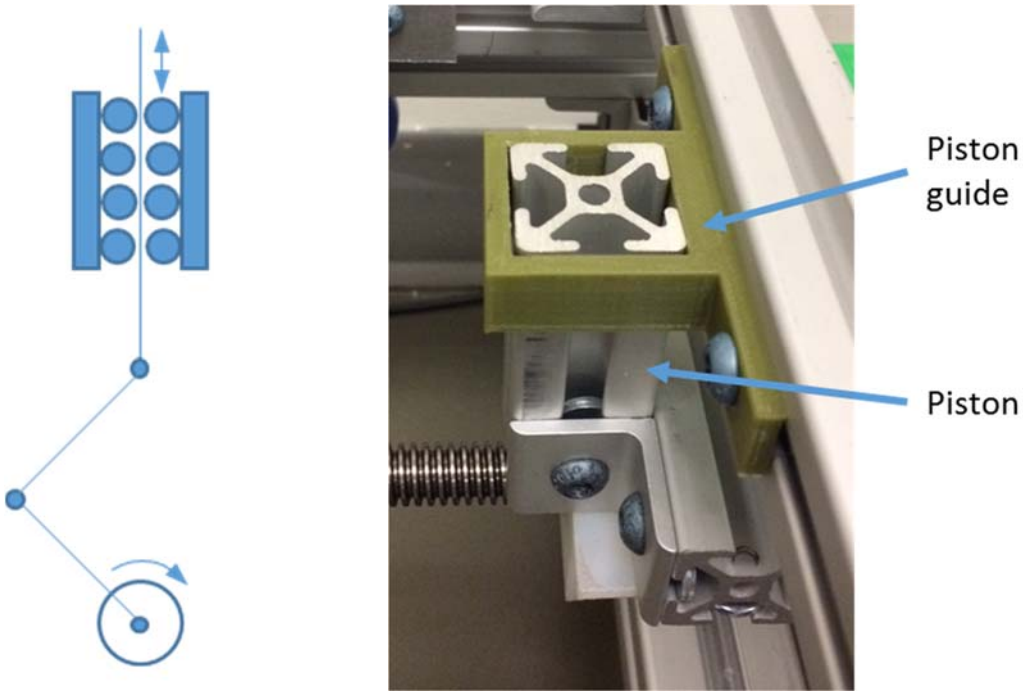

(a) (b)

Figure 3.11. Diagram of (a) piston motion allowing for two degrees of freedom, and (b) MakerBot printed piston sleeve.

The *y*-axis assembly moves linearly along the *x*-axis by necessity of design, meaning that all of the wiring for the y-axis must also move to whatever position the platform is in. Therefore, the wiring has to unfold over itself as the platform moves further away from home position, requiring a cable carrier system to ensure the wiring does not get caught in the movement. The standard design for a cable carrier is essentially a hollow chain link that only bends in one direction, so that when the links are connected the wires thread through the center of the links and the entire cable unfolds with the connected links. Cable carrier links for the translation system were designed and printed on the MakerBot Replicator 2X, and assembled as shown in Figure 3.12. Cable carrier with individual links printed using FFF.

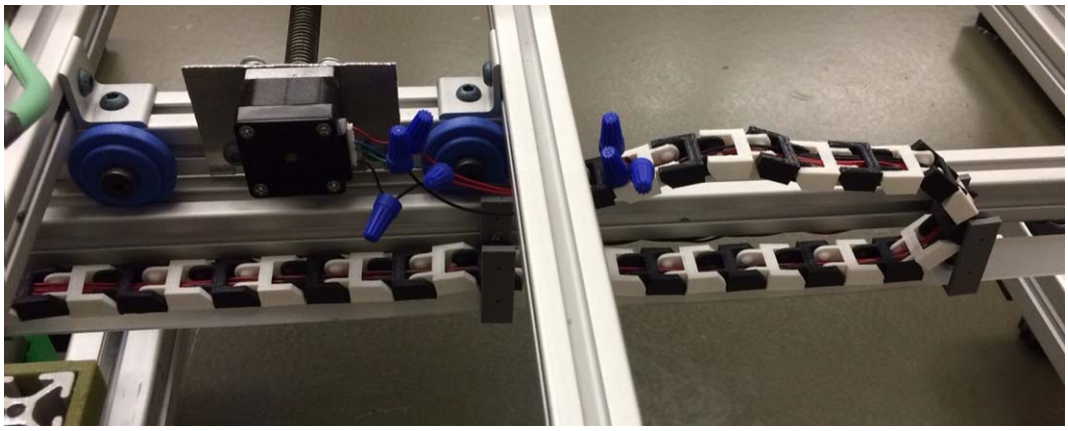

Figure 3.12. Cable carrier with individual links printed using FFF.

The extrusion platform itself is also important in the table design, because the platform material and temperature significantly affect how well printed beads adhere to the plate. The build plate initial design was a 1/8 in. thick sheet of clear acrylic, which was effective for polypropylene bead deposition during preliminary testing. However, the Amphora™ polymer permanently bonded to the acrylic plate during extrusion, and heat

from the extrusion process caused the acrylic plate to warp. For these reasons the platform material was changed to aluminum, which would not permanently bond with the polymer and allowed heat to dissipate more efficiently.

Similarly, with the platform at room temperature the beads experience a higher thermal gradient change during the deposition process than if the platform were heated, causing warping and not allowing the polymer to stick to the platform. Therefore, design of a heated bed began by using the preheat function of the Exon8, which is intended to provide heated air to an enclosed build volume. The preheat air supply was redirected to heat the platform by spacing two aluminum plates ½ in. apart and funneling the heated air between the plates through a predetermined path. The air temperature controller was set at 65°C and heated air traveled through a flexible hose to reach the platform. Unfortunately, air exiting the platform heat exchanger had cooled to nearly 30°C. As a result, the heated air from the Exon8 was not sufficient to maintain a uniform temperature on the build platform. An alternative heating method was designed using a 150V flexible high-resistivity wire heating pad, an AGT-25DA steady-state drive, and a JLD612 temperature controller. The heating pad was placed between the two aluminum plates, with the bottom insulated. This new heating system effectively reached and maintained desired temperatures in the range of 60-75°C uniformly over the build platform. The aluminum allows the heat to propagate evenly through the plate due to high thermal conductivity, and the temperature controller provides the user the capability to define a steady state curve that is appropriately damped based on application. For example, the user can define an underdamped temperature control curve that oscillates near the desired temperature, or an over-damped case with little to no temperature oscillation.

3.2 Sample Preparation and Manufacturing

Once the FFF system was fabricated and tested for reliability, it became capable of printing beads which could be used to study large scale FFF deposition by altering specific deposition parameters. The first step in the parameterization process was to implement a sample preparation method that ensured viable comparison data across deposition parameters.

3.2.1 Sample Preparation

One of the main concerns with processing thermoplastic polymers in large scale FFF is determining that the polymer is dry before processing. Many polymers are hydrophilic, meaning that they have a tendency to attract water molecules in the air due to ion charges. During the extrusion process, water molecules turn to gas and create bubbles in the polymer flow, which lead to voids in the finished part. Evaporating water inside an extruder also causes cavitation, which can damage the extruder. To avoid the creation of voids and cavitation, polymer pellets must be dried before processing.

TGA Analysis. To determine appropriate drying temperatures and times for each of the four polymers used in this study, published material documentation was used in conjunction with TA Instruments' Thermo-Gravitational Analyzer (TGA) test data (TA Instruments, New Castle, DE). A standard TGA test involves heating a polymer at a specified rate of temperature rise, holding the polymer at the specified temperature, and continuously measuring the polymer mass as a function of time and temperature. To obtain parameters needed to dry a polymer, the goal is to find a steady state temperature at which the polymer can be exposed for a specific period of time to evaporate all

moisture from the polymer. Polymers are typically dried between 50-70°C for as little as two hours or as long as twelve hours. Figure 3.13 shows TGA test results for the four polymers used in this study: Amphora™, Neat ABS, 13% Carbon Fiber filled ABS, and 10% Carbon Fiber filled ABS. In our TGA tests, shown in Figure 3.13, percentages of the initial sample mass are recorded over time, and the ratio between current sample mass and initial sample mass declines slightly before approaching steady state. At the point where minimal mass difference is measured over a significant amount of time, the polymer can be said to be sufficiently dry. Amphora™ is dried for 12 hours at 50°C based on documentation by Eastman [24]. The various blends of ABS, with and without carbon fiber, are dried at 70°C for four hours.

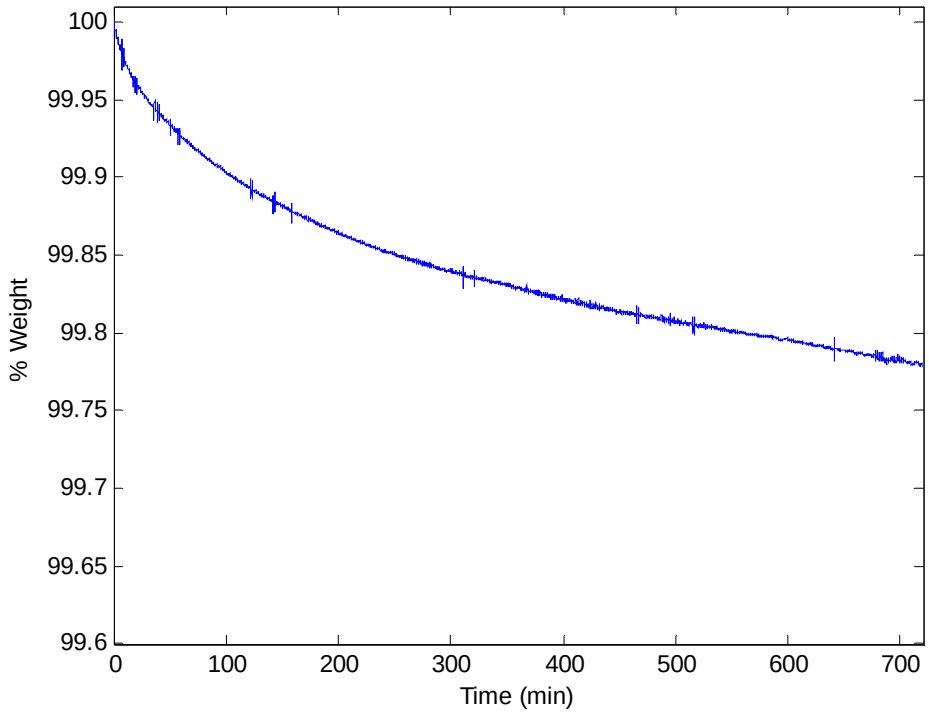

(a)

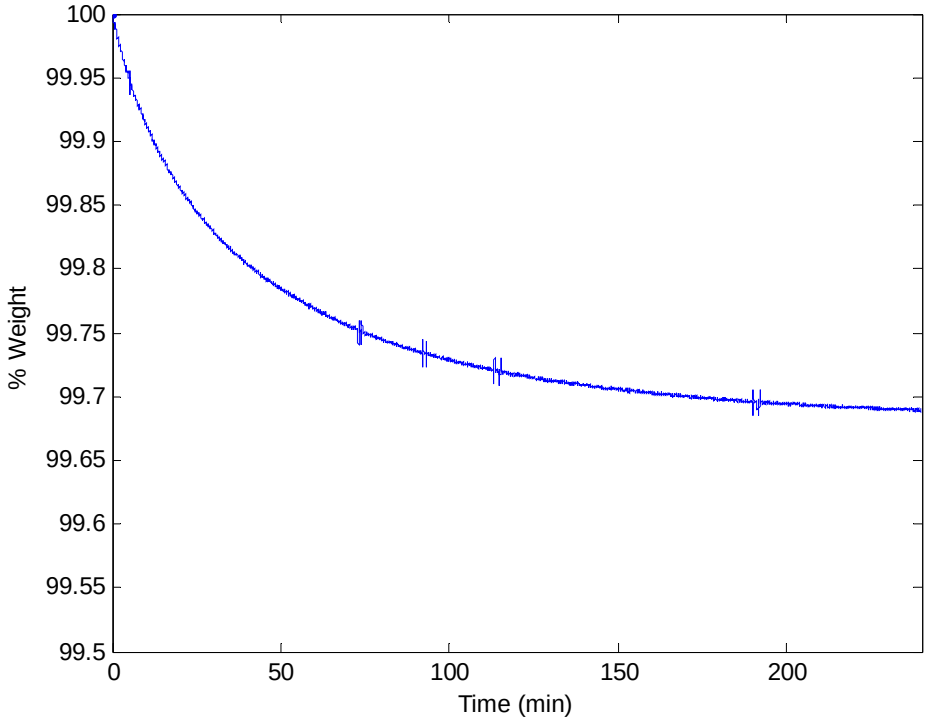
100
99.95
99.9
99.85
99.8
99.75
99.7
99.65
99.6
99.55
99.5
% Weight
0
50
100
150
200
Time (min)

(b)

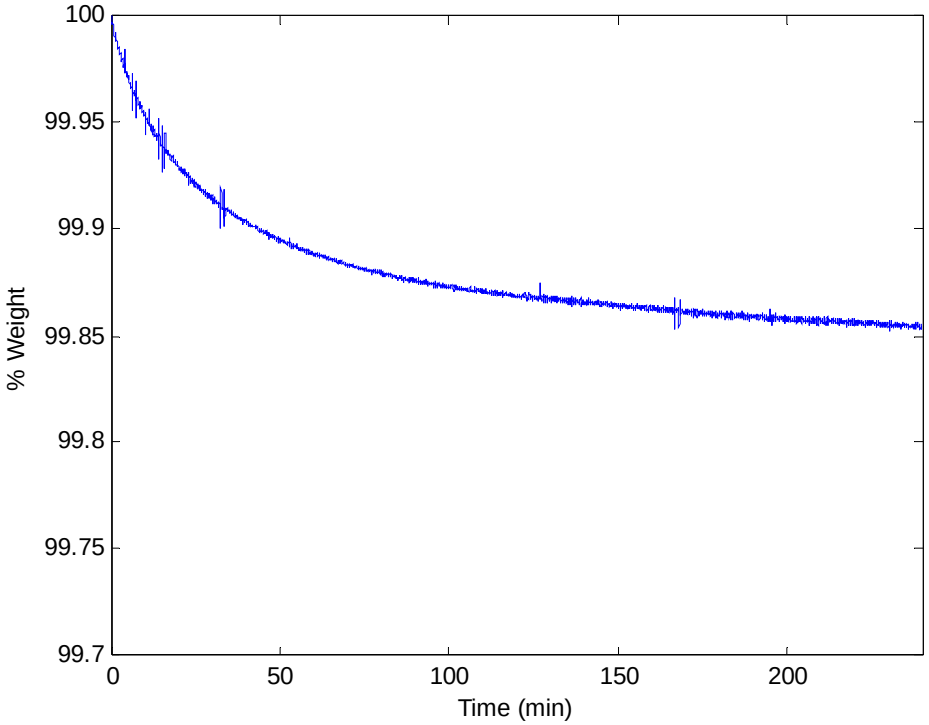
100
99.95
99.9
99.85
99.8
99.75
99.7
% Weight
0
50
100
150
200
Time (min)

(c)

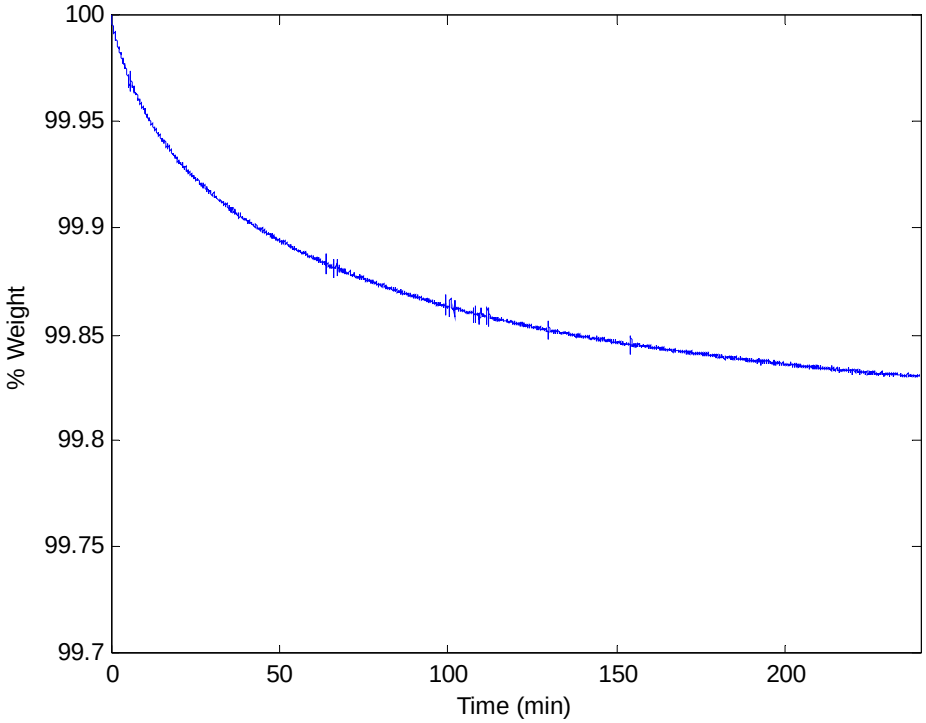

(d)

Figure 3.13. TGA drying tests for (a) Amphora™, (b) Neat ABS, (c) 10% Carbon Fiber filled ABS, and (d) 13% Carbon Fiber filled ABS.

Results in Figure 3.13 show each polymer exponentially decaying toward steady state mass within their specific time and temperature ranges, proving that the specifications used in each test are appropriate drying conditions for the polymers. The definition used for "dry" for each polymer is such that 10% or less of the initial moisture in the bead remains after drying. Once dried, polymer pellets should be used immediately to avoid potentially absorbing moisture from the air and requiring re-drying.

The TGA can also be used to determine mass percentages of different materials in a blend such as the carbon fiber filled ABS pellets. Mass percentages are determined by heating the composite pellet to a temperature at which one material will thermally degrade while other components remain unaffected. Literature search provides information on the thermal degradation of carbon fibers, indicating that fibers begin to

thermally degrade above 500°C [58]. Therefore, TGA tests should be run with carbon fiber inclusions at or below this threshold temperature. A TGA test was run to determine the burnoff properties of neat ABS (Figure 3.14).

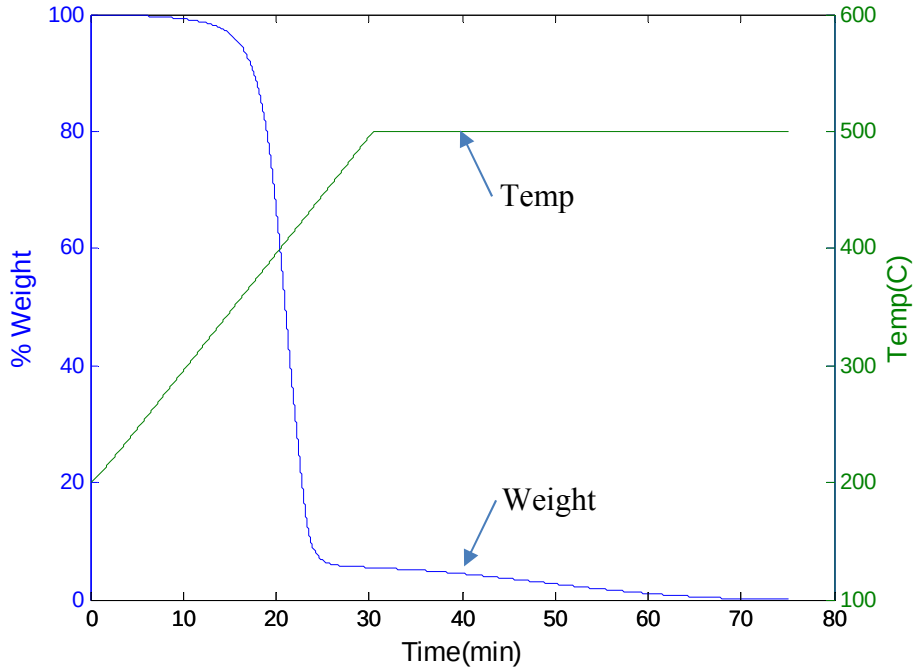

Figure 3.14. Burnoff test for neat ABS ramped up to and held at 500°C for 80 mins.

The data shown in Fig. 3.14 indicate that the neat ABS burns away completely during the test, such that there is no mass remaining after 70 minutes at 500°C. A similar TGA test was performed on the 13% carbon fiber filled ABS pellets to determine the percentage mass of carbon fibers in the pellets (Figure 3.15). Results from the 13% carbon fiber filled ABS pellets show the fiber percentage by mass to be 12.6% on average over three trials, which compares well to the vendor stated 13% value.

The same procedure was followed for the 10% Carbon Fiber Filled ABS pellets to determine percentage be mass of fibers. Results displayed in Figure 3.16 show that the

average fiber percentage by mass is 10.4% as the test reaches steady state after ten minutes.

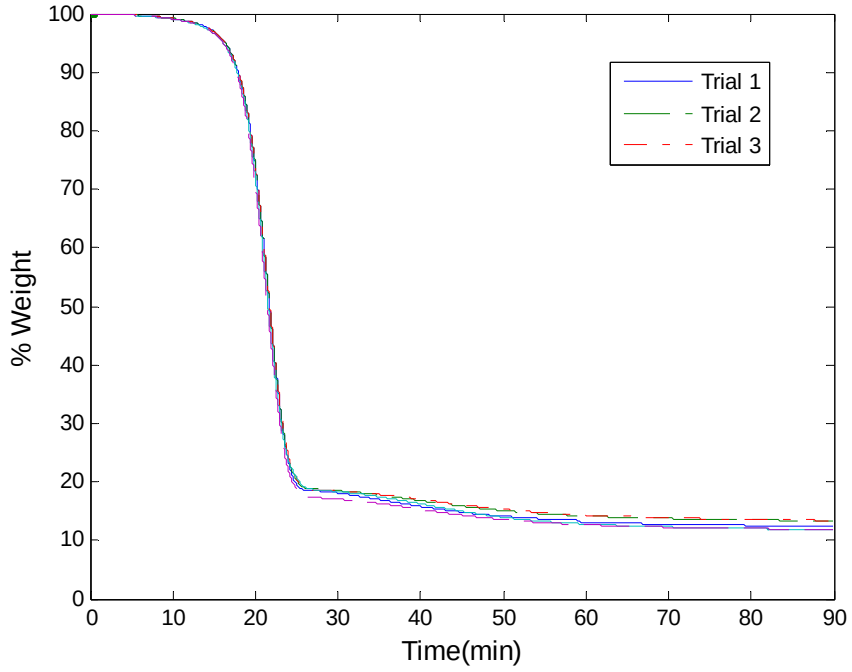

Figure 3.15. Burnoff test for 3 pellet samples of 13% carbon fiber filled ABS ramped to and held at 500°C for 60 mins.

DSC Analysis. The Differential Scanning Calorimeter (DSC) measures the amount of heat required to raise the temperature of the polymer using an empty reference sample. The DSC may be used to measure the glass transition temperature (T_g) of a polymer, which may appear as the first kink in the otherwise smooth plot of heat input versus temperature. It may also be used to determine the amount of heat required to increase the polymer temperature from room temperature to melt temperature, which quantifies the total amount of heat required to process the polymer. Figure 3.17 shows DSC tests for each polymer, along with their labeled T_g.

The DSC test results in Figure 3.17 should show two features, an initial kink in the curve that indicates the polymer's T_g, and a second, larger dip that represents the melting temperature (T_m) of the polymer. The plots in Figure 3.17 of the neat ABS and 10% carbon fiber filled ABS clearly show these features, but in the Amphora™ and 13% carbon fiber filled ABS plots the second dip representing T_m is not apparent, which is not typical when compared to other thermoplastics. The lack of a distinct melt temperature typically occurs when a polymer is a blend of several different individual polymers, with each constituent polymer having its own T_m. There is strategic advantage to designing a polymer with no specific T_m, allowing processors a broad range of operating temperatures during processing instead of having to maintain a specific range for melt.

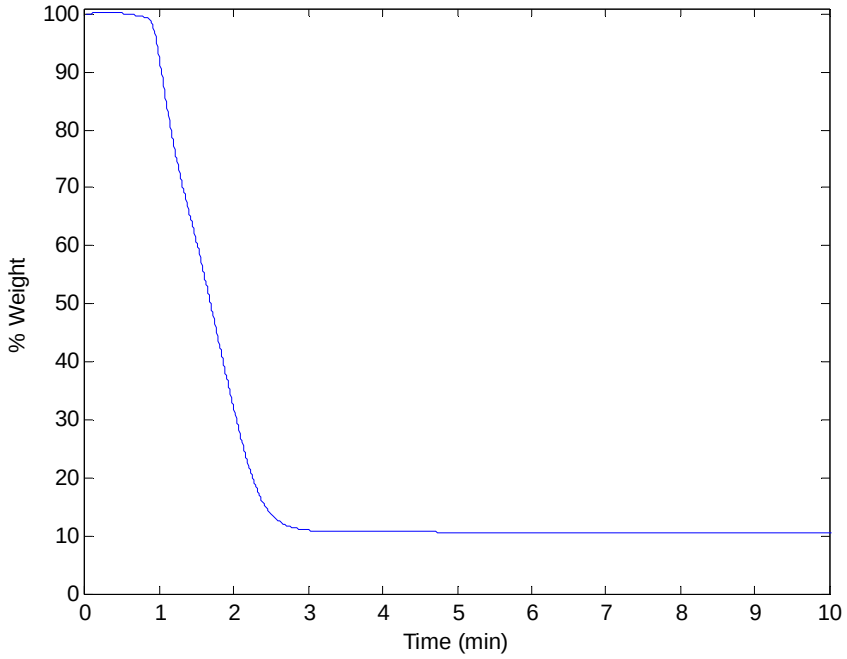

Figure 3.16. Burnoff test for 10% Carbon Fiber Filled ABS ramped up to and held at 500°C for 60 minutes.

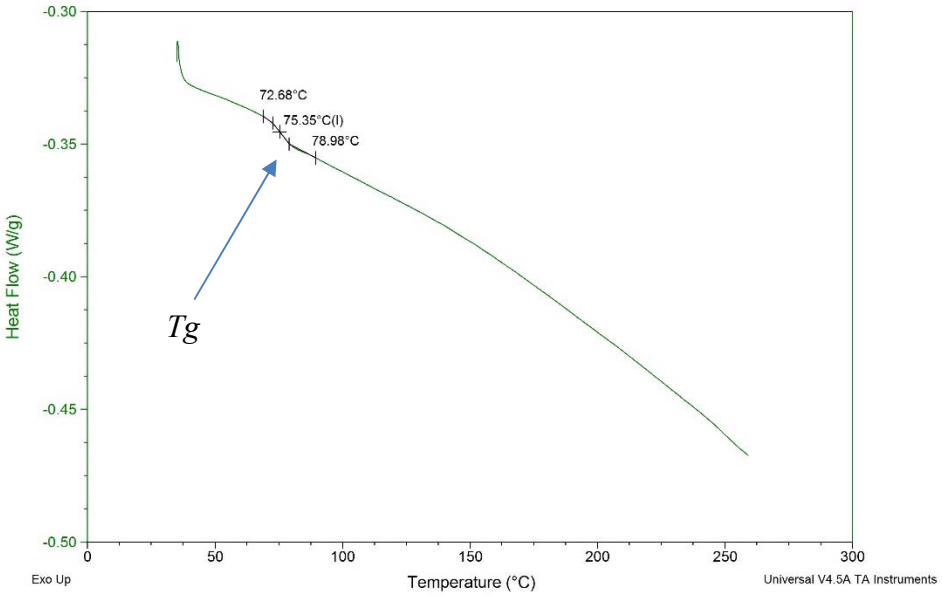
72.68°C
75.35°C(l)
78.98°C
Tg
Heat Flow (W/g)
Temperature (°C)
Exo Up
Universal V4.5A TA Instruments

(a)

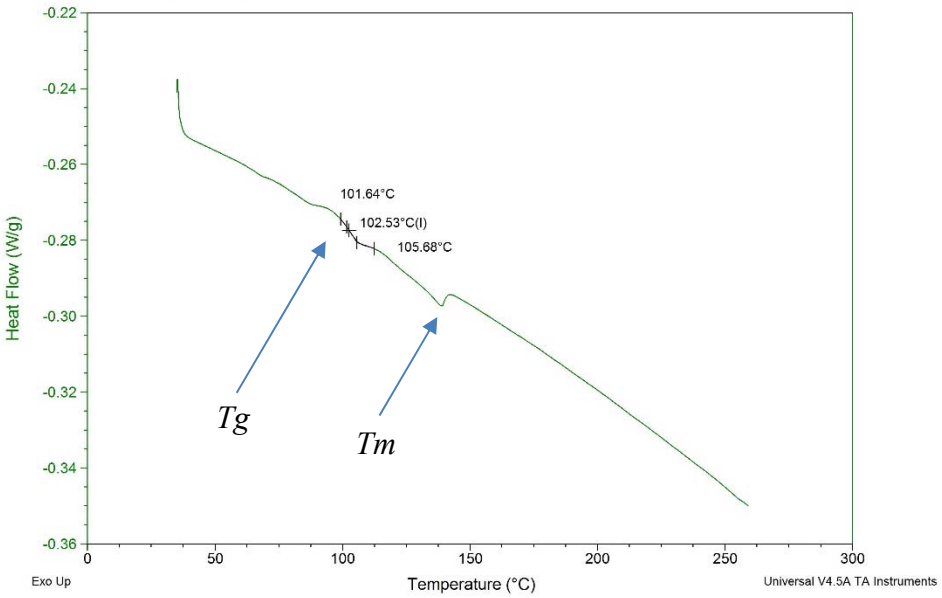
101.64°C
102.53°C(l)
105.68°C
Tg
Tm
Heat Flow (W/g)
Temperature (°C)
Exo Up
Universal V4.5A TA Instruments

(b)

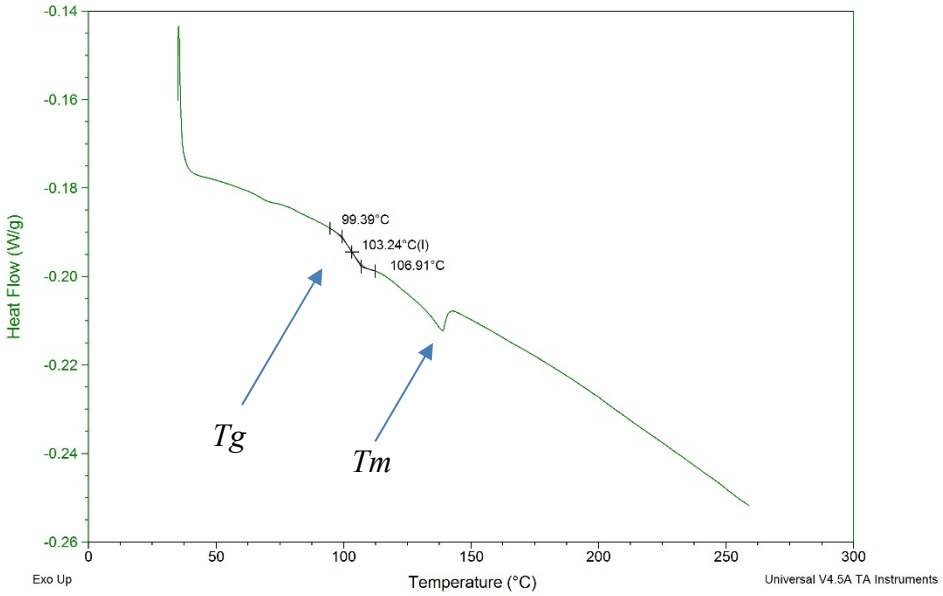

(c)

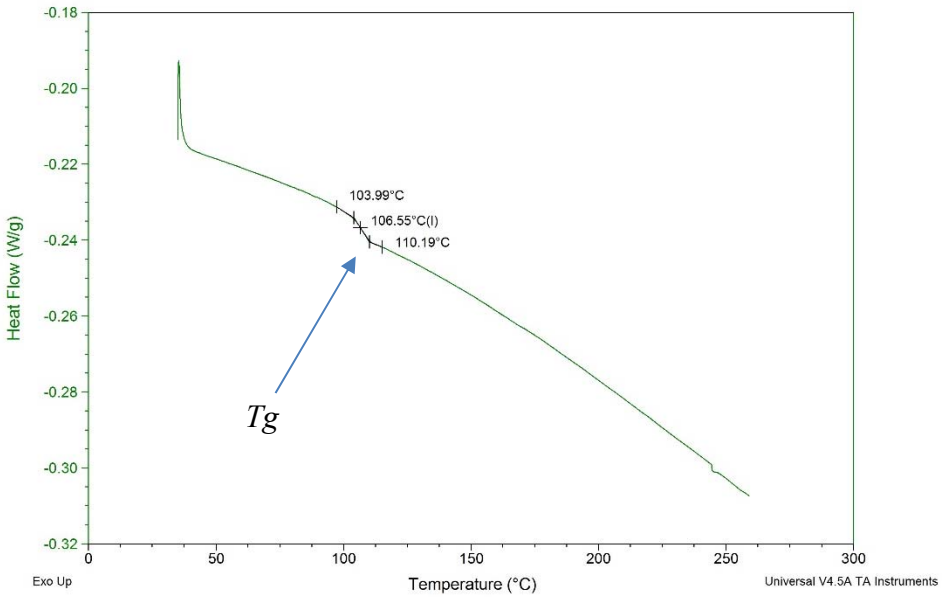

(d)

Figure 3.17. DSC tests showing T_g and T_m for (a) Amphora^{TM}, (b) Neat ABS, (c) 10% Carbon Fiber filled ABS, and (d) 13% Carbon Fiber filled ABS.

The primary result from Figure 3.18 is a comparison of the polymers used in this study. It is evident that while the 10% and 13% carbon fiber filled polymers are both ABS with carbon fiber inclusions, the base polymers are significantly different because the Amphora™ and the 13% carbon fiber ABS do not have a specific melt temperatures. Therefore, in comparing the polymers used in this study, it is important to keep in mind specifically that the 10% and 13% carbon fiber filled ABS are different blends of polymer and cannot be directly compared.

The DSC can also be used to compare amounts of energy required to heat the polymer from room temperature to melt, indicating which polymers require the most heat and are therefore more expensive to process. Figure 3.18 shows all four polymers on the same plot for required heat comparison.

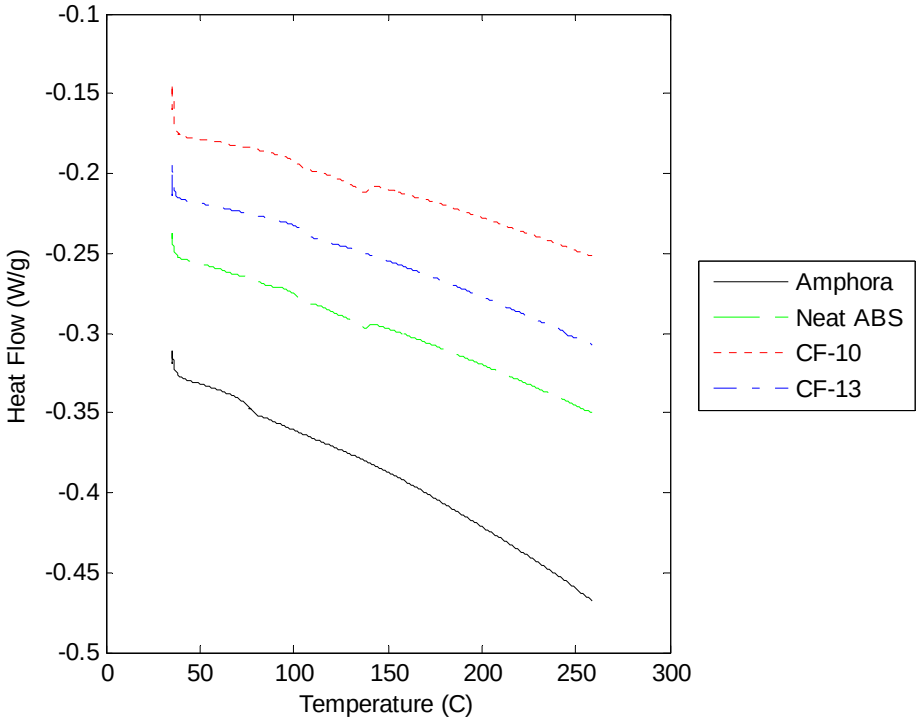

Figure 3.18. DSC comparison plot of required heat to process.

Based on the results from the DSC plots in Figure 3.18, Amphora™ requires the most heat for processing, at nearly twice as much heat as the 10% carbon fiber filled ABS. Interestingly, both carbon fiber filled ABS polymers require less heat than the neat ABS. The effect of carbon fiber filled composites requiring less heat is based on the difference in specific heat of polymers and carbon fibers, which highly affects the specific heat of the composite [59]. The type of ABS blend also effects the specific heat of the polymer, which could help to explain why the 13% carbon fiber filled ABS requires more heat than the 10% carbon fiber filled ABS even though an increase in carbon fiber volume should decrease heating energy. Differences between the two carbon fiber filled ABS blends are obvious when noting that the original DSC results in Figure 3.17 are significantly different between the two polymers.

Melt Flow Index Analysis. Obtaining viscosity data for each polymer may aid in interpreting polymer behavior results based on pressure losses in capillary flow, and is useful in understanding characteristics of the flow inside the extruder. Using a Melt Flow Indexer and following ASTM Standard D1238-13, data was collected for the four polymers at different temperatures, providing a measure of relative viscosities of each polymer based on differences in flowrate over a range of temperatures [60]. Figure 3.19 shows flowrate data for each polymer from the Melt Flow Indexer over temperature ranges seen inside the extruder. Results from Figure 3.19 show that Amphora™ has the lowest relative viscosity over the extrusion temperature range, while the 10% carbon fiber filled ABS has the highest relative viscosity. Theoretically, if all other factors were the same, the addition of more carbon fibers from 10% to 13% should make the 13%

carbon fiber filled ABS more viscous than the 10% carbon fiber filled ABS. However, as noted previously in this section, the DSC results demonstrate that the ABS blends are different between the two polymers. Additionally, differences in the carbon fiber inclusions could also contribute to a difference in viscosity, such as the 13% carbon fiber ABS possibly having smaller fiber lengths which could make the mixture less viscous than the 10% carbon fiber filled ABS.

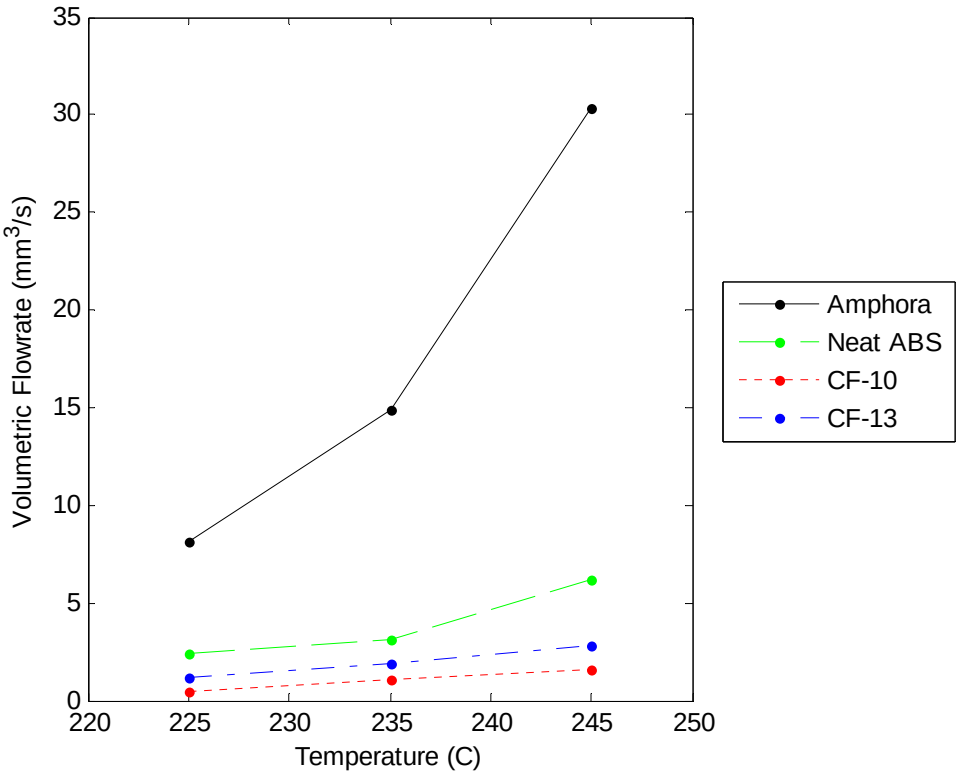

Figure 3.19. Melt Flow Indexer data for each polymer as a function of flowrate.

Fiber Length Distribution Analysis. For the 13% Carbon Fiber Filled ABS, a short study was conducted to determine the length and diameter distributions of chopped fibers inside the ABS pellets. Distribution information will give insight into the radius, length, and aspect ratio of the fibers, and help to understand the effects that these fibers will eventually have on bead geometry. To measure distribution information, a TGA

burnoff test as described in Section 3.2.1 was used to isolate the carbon fibers from the ABS pellets, resulting in a small sample of fibers from a single pellet. Fibers from the pellet were then placed on a piece of copper tape and placed inside a Scanning Electron Microscope (SEM) for magnified imaging. Traditional practice for SEM imaging requires that samples be sputter-coated to allow for good image resolution, but given that carbon fibers are electrically conductive, this procedure was not necessary for the desired resolution. The SEM settings used to obtain image data are shown in Table 3.1.

Table 3.1. SEM settings used to measure fiber distribution data for 13% Carbon Fiber Filled ABS pellets.

Parameter	Vacuum	Mode	Magnification	Voltage	Height
Length	High	SEI	220x	15kV	12mm

Three images were taken for both radius and length, giving a large sample distribution for both parameters. SEM imaging software allows the user to take manual measurements from an image based on the scale of the image, a tool that was used to take distribution measurements for every fiber that could be distinguished in each image. This measurement process resulted in a sample size of 213 data points for diameter and 361 data points for length. Figure 3.20 shows an example SEM image with measurements for fiber length.

The data collected from the SEM were recorded in data files and uploaded to MatLab to be processed and analyzed. Figure 3.21 shows each of the data sets as histograms, as well as the length data sets overlaid with a distribution curve for comparison.

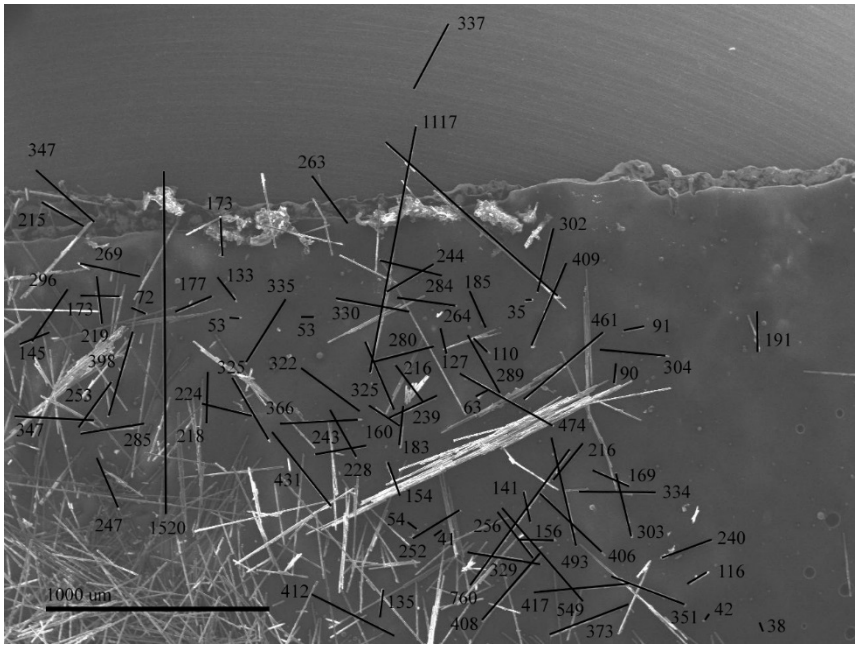

Figure 3.20. SEM images of carbon fiber lengths in μm.

As seen in Figure 3.21, the fiber length data set does not fit a normal distribution. A Chi-square analysis returns a rejection of the null hypothesis that the fiber length data are normally distributed at a confidence level of 90%. Lack of fit is caused by the nature of having chopped fibers, where if one long fiber is cut into two pieces, it creates two smaller data points when it would originally only have created one larger data point. As a result, many data points are seen at the smaller end of the data space, decreasing in frequency as the length increases, and finally ending at a maximum possible length of ~2000 μm. Interestingly, the length of a pellet is approximately 4000 μm, indicating that fibers do not span then entire length of the pellet.

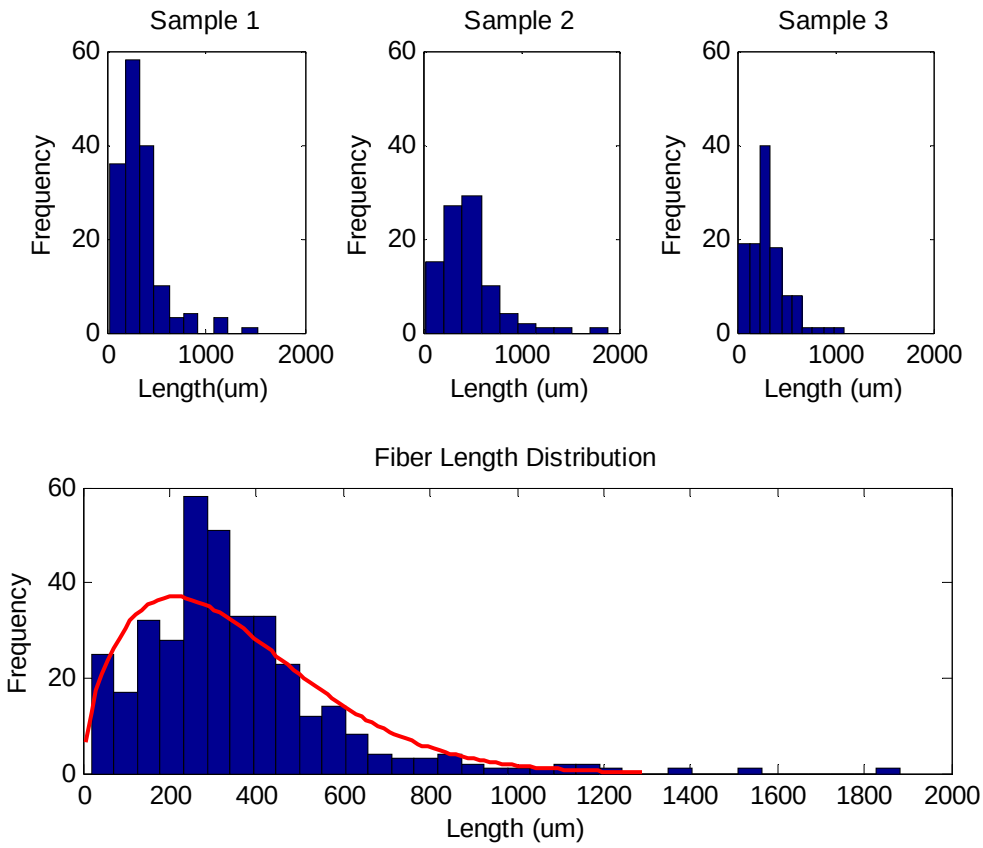

Figure 3.21. Individual sample fiber length distributions and combined distribution overlaid with a Weibull distribution curve.

To model the fiber length data set, a 2-parameter Weibull distribution was used. The lognormal distribution is also a potential candidate for measuring fiber length distribution, but the Weibull distribution allows for a shorter, thicker peak than the lognormal distribution:

$$f(l) = \frac{\beta}{\eta}\left(\frac{l}{\eta}\right)^{\beta-1} e^{-\left(\frac{l}{\eta}\right)^{\beta}} \qquad with\ \beta = 1.59,\ \eta = 394,\ l = fiber\ length \tag{3.2}$$

Fiber length distributions were also studied in fiber reinforced composites by Karsli [61], resulting in similar distribution patterns as those seen in Figure 3.21. Other carbon fiber

composites are expected to have similar fiber distributions to those shown in Figure 3.21, with some variation based on how the composite is processed.

3.2.2 Large Scale FFF Deposition

With data collected on how polymer samples should be prepared for FFF processing, the next step was to begin generating samples to determine an appropriate set of parameters for the system. The sample manufacturing process is described here, including methods for sample creation and some difficulties and observations during the manufacturing process.

Parameterization of the FFF design space for our study is defined in terms of four parameters that include screw RPM, nozzle height, table speed, and polymer. The range of interest of each parameter is listed in Table 3.2.

Table 3.2. Parameter settings defined using minimum, maximum, and intermediate values for each of the system settings, and four types of polymers.

Polymer Type	Screw RPM	Nozzle Height	Table Speed
Amphora™	20	1.5 mm	5 mm/s
Neat ABS	40	3.25 mm	10 mm/s
ABS 10% CF	60	5 mm	15 mm/s
ABS 13% CF	80	-	-

Using the parameter settings from Table 3.2, our large scale FFF system will be used to deposit beads and study the effects of these parameters on the deposition process. To accumulate enough data to fully define the FFF system, samples must be produced at each possible group of parameter settings for each polymer. One bead can produce more than one sample cross section, each taken at a different location on the bead to subdue local effects. Therefore, 36 samples should be created for each polymer, one for each

combination of RPM, speed, and height, which is then increased to 108 total samples by taking three cross sections from each bead. The generation of these beads follows the process outlined here.

The Exon8 single screw extruder and the heated platform must be turned on approximately 20 minutes before the start of testing, to allow for the screw and platform to heat to their prescribed temperatures. The processing temperature was set to 240°C for the Amphora™ per the Eastman processing guidelines [24], and the ABS pellets were set to a processing temperature of 230°C to be comparable to the small MakerBot system [62]. The platform temperature was set to 65°C to allow the polymers to better adhere to the plate, and remained constant for all polymer types. After the extruder and platform were fully heated, pellets were taken out of the drying oven after drying at settings as described in Section 3.2.1 and poured into the extrusion hopper, with excess pellets set aside to be used within a few hours to prevent absorbing moisture again. The screw was then turned on to the maximum RPM of 80, and run for two minutes to purge any previous polymer out of the screw before testing begins. After two minutes, the FFF system was ready to produce beads.

The most difficult aspect of the FFF system to alter is the nozzle height from the table, because it requires the user to manually raise or lower the extruder on the z-axis while checking nozzle height using aluminum gauges. Therefore, beads were created by cycling screw RPM and platform velocity through all possible combinations before altering the nozzle height. To create a bead, code was entered into the LabVIEW program that operates the platform, as described in Appendix A.

Platform Translation. LabVIEW code determines the speed at which the platform moves, as well as the total length of the bead. For example, the code in Figure 3.22 sets the platform velocity to V100000, or 5 mm/s, then travels to where the nozzle hovers over the starting corner of the platform, A1750000 on both of the axes. The platform then moves relative to the nozzle for the majority of its width, moving the primary axis P3000000 steps while the secondary axis waits 30,000 milliseconds, M30000. The secondary axis then moves P60000 steps while the primary axis waits 6,000 milliseconds, M6000. The primary axis retraces its path back across the platform relative to the nozzle D3000000 steps while the secondary axis waits, at which point both axes translate to bring the platform back to its home position. In effect, the code in Figure 3.22 creates a bead shaped like an elongated "U" on its side. The "R" character at the end of each line sends the code to be executed by the stepper motors, and the "\r" at the end of the line tells LabVIEW to start a new line to be executed simultaneously but separately from the first line. More in depth information on specific coding for the platform can be found in Appendix A.

Each bead was created by using a combination of LabVIEW platform codes with varying screw RPMs and nozzle heights. The screw was turned on as the platform moved to its starting position, allowing the polymer flow to reach steady state before the bead began printing on the platform. The bead was then created as the extruder laid polymer on the platform. The section that was sliced for cross sections generally came from the first path of the primary axis across the platform, assuming that the bead shape remained constant to demonstrate a steady state flow. In some cases, the bead shape did not become constant until the second path across the platform, in which case the second path

was used to cut cross sections. In an effort to conserve polymer, once a large enough section of steady state bead was printed on the platform to produce three cross sections with no end effects, the flow of polymer was cut off by turning off the extruder, and the platform would finish its path without extruding polymer. Once the platform was back in its home position, the bead was allowed to cool for two minutes before being removed from the plate, allowing enough time for it to solidify from the extrusion process before being moved. Care was taken not to deform the bead in any way, including bending, scratching, or twisting the bead, to preserve the shape of the cross sections that would be taken from each bead.

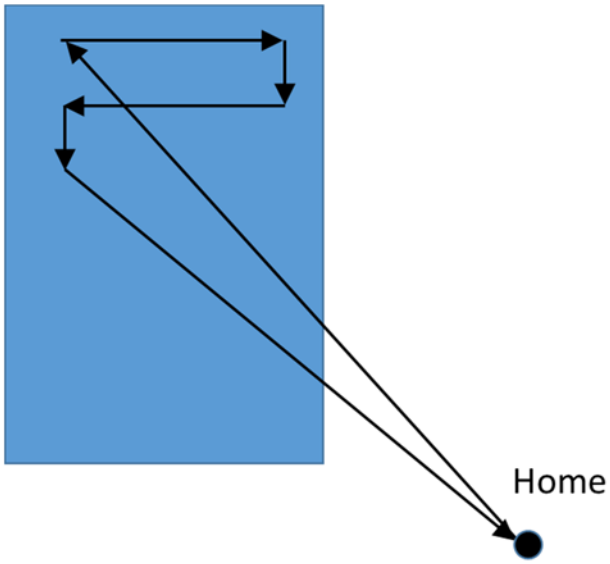


```
/AV100000A1750000gP3000000M6000D3000000M6000G1A0R\r
/3V100000A1750000gM30000P600000M30000P600000G1M3000A0R
```

Figure 3.22. Path generation of a single bead.

Manual Parameter Incrementing. Varying the table speed and screw RPM were accomplished simply by altering the platform code and the extruder's digital readout, but as mentioned previously, the nozzle height needed to be manually adjusted. Small aluminum gauges were created at each of the three nozzle heights, with their thickness equal to the required height. The screw was then raised or lowered to the desired height by rotating the axis' screw until the aluminum spacer was pressed lightly into the platform, ensuring the correct nozzle height. The aluminum spacers heat up quickly while in contact with both the heated platform and the extruder, and caution should be taken when handling them.

Bead Cross Section Selection. Selection of the area used to acquire bead cross sections followed a specific set of guidelines, to ensure accurate representation of the bead shape from a relatively small section of the bead. First, the cross sections should not be taken from first section of the bead where the extrusion has just started, approximately the first inch of the bead, for the bead shape and extruder to reach steady state and ensure consistency. Similarly, the cross sections should not be taken within approximately an inch from where the bead turns the corner, once again to avoid disturbances from steady state due to end effects. Based on the program used to create these beads, neglecting an inch on both sides of each print path leaves a section of approximately four inches from which to take cross sections. The next criterion is to visually inspect the bead for steady state sections. In some cases, especially at the higher RPM settings, the bead might take longer than the initial inch to reach a steady state cross section, and this should be obvious in the bead shape. If the bead takes longer than the initial inch to achieve steady

state, then sections should be taken from the area of the bead exhibiting the most uniformity.

For the ABS polymer beads, the selection process is easy because the beads exhibit a high degree of uniformity across most parameters. However, for the Amphora™ beads the process is significantly less objective. The extruder struggles more to process the Amphora™ pellets because they are significantly tougher than the ABS pellets, requiring the screw to work harder to rotate and shear the pellets into melt, which in turn adds to variability in the flow of polymer out of the nozzle. Results from the Melt Flow Indexer in Section 3.2.1 indicate that the Amphora™ has a lower viscosity once melt has been achieved, but the amount of energy required to achieve melt is significantly higher for the Amphora™ as indicated by the DSC results in Section 3.2.1. Therefore, finding a section of Amphora™ bead that is "steady state" is much harder because the bead shape is inconsistent, alternatively thickening and thinning depending on the flow. Discretion was used to determine the best sections to take from these beads, seeking small sections that remain relatively consistent. An example of a printed Amphora™ bead is shown in Figure 3.23

With the sections of the bead chosen for analysis, an IsoMet low speed saw was used to cut smooth cross sections from each bead. The saw allows the user to cut smooth cross sections using a thin 'wafer' blade, which eliminates the rough edges of a traditional saw cut and evacuates material from the cut as it progresses. Samples were clamped onto the saw arm so that the steady state section of the bead was placed over the saw blade, and four cuts were made. The first cut removes excess material from the end of the bead, and the subsequent three cuts each create a thin cross section of the bead.

The saw was run at a setting of 7, recommended for general cuts by the IsoMet manual, and the arm was incremented 1/10 in. for each cut using the built-in caliper, creating a section thickness of 1/10 in. [63].

Figure 3.23. Example bead printed with Amphora™, showing print path and flow pulsing.

Freestream Data Collection. To provide a baseline for comparison of the printed beads, data was also collected for the freestream flowrate of the screw at varying RPM's for each polymer. Freestream flowrate data provide a theoretical maximum flowrate of the Exon8 for each polymer based on RPM, and can be used to compare the bead geometry information against a baseline. For each polymer, the RPM was set at each of the four parameter settings used to create beads, and three samples were created with the extruder by simply extruding polymer without resistance from back pressure due to the platform. Samples were each extruded for a minute, and weighed to determine flowrate based on density for the specific polymer at that RPM setting. Freestream samples can be seen in Figure 3.26. The density of each polymer was experimentally determined using a

computational method outlined later, by determining the flowrate based on cross-sectional area, sample thickness, and sample mass.

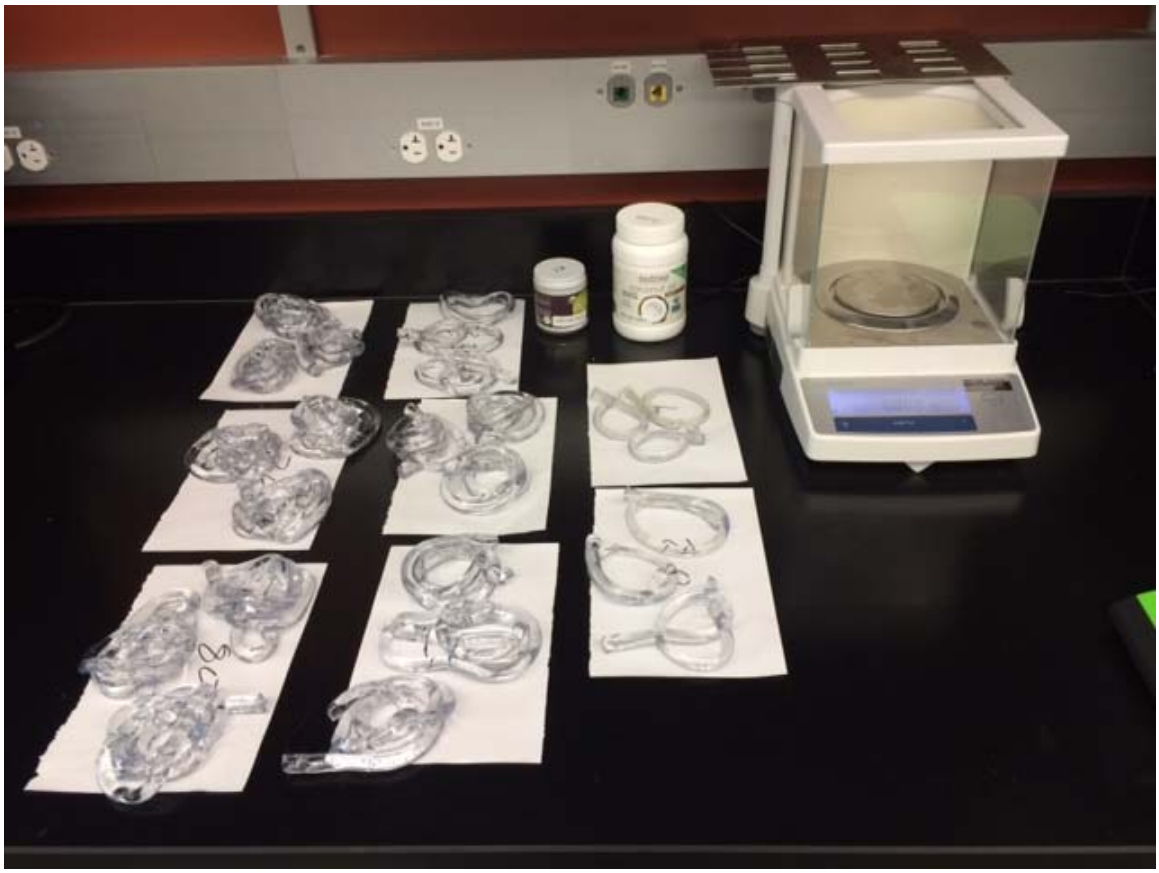

Figure 3.24. Freestream samples printed using Amphora™.

3.3 Image Processing

The goal of sample imaging in this section is to transform each bead cross section into data that can be evaluated to determine output parameters, and therefore characterize different aspects of the bead geometry. To generate descriptive geometry parameters in MatLab, the image needs to be converted into a numerical representation, the process for which is outlined here.

3.3.1 Imaging

Accurate images of each cross section are required to ensure that each image precisely captures the geometry of the bead, as well as removing any adverse effects from imaging such as shadow, color distortion, and stray pieces of polymer still attached to the bead. Before imaging, each cross section was gently cleaned using a paper towel, removing any little pieces still attached after the saw cut. Because a low speed saw was used, these pieces were minimal, and the edges of the cross section relatively smooth.

A desktop DinoLite optical microscope was calibrated such that the largest cross section could fit easily into its frame of view, and focused such that the images would be clear. Because each cross section has a uniform thickness, the microscope needed only to be calibrated once for each polymer type based on the largest bead from that polymer. Before imaging samples, a calibration slide was placed in the microscope and imaged. The slide has precise measurements printed on its face to determine the scale of the image. This scale stays the same as long as the microscope settings are not changed, and can be used as the scale for each cross section image as well.

Samples were placed in the microscope and imaged, taking care that the bottom of the bead was aligned parallel to the bottom of the image frame. Alignment was accomplished with built-in microscope software that allows users to create and manipulate lines over top of the image. By creating a horizontal line and placing it directly under the cross section, the microscope platform could be finely rotated to align the bottom of the cross section with the horizontal line. The horizontal line, then, could be shifted down so it would not interfere with the image processing later. A vertical line was also placed on the left hand side, and the slide shifted to place the bead in the

approximate center of the image. A sample image using this alignment technique is shown in Figure 3.25.

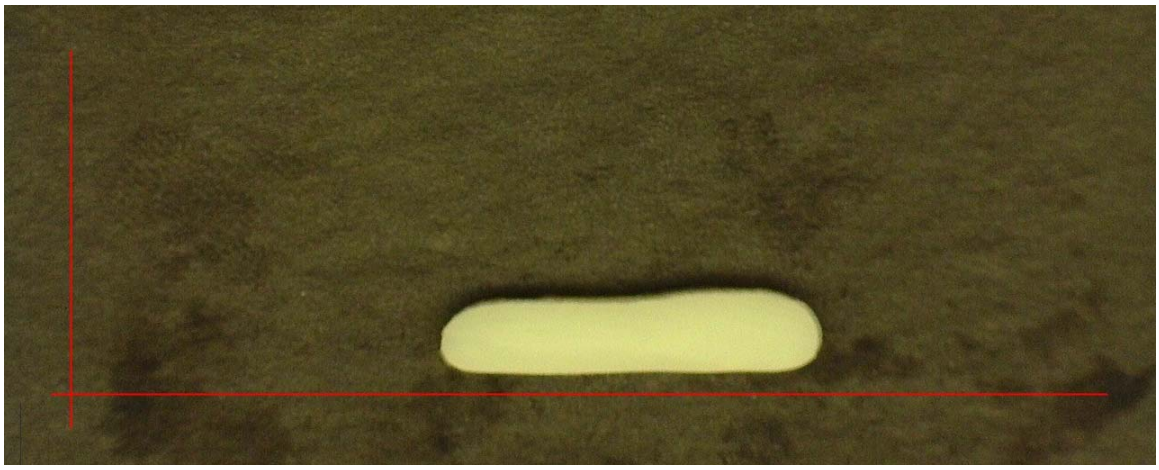

Figure 3.25. Sample ABS cross section showing horizontal alignment technique.

3.3.2 Image Processing

Once the sample is properly aligned in the image frame, the image is saved and ready for processing in MatLab. The processing is done using the "im" program suite, which allows MatLab to upload and manipulate images. Each image is read into a master file and cropped based on the size of the largest bead cross section for each polymer. Using a threshold value between zero and one, the image is converted to a black and white image where all pixels darker than the threshold value are converted to black pixels, and all pixels lighter than the threshold value are converted to white pixels. The threshold value varies by polymer but is approximately 0.5. In the case of Amphora™, to achieve the desired color contrast using the threshold method, the cross sections were dyed with black ink because the beads are naturally transparent, and imaged on a white background. The neat ABS beads were imaged on a black background, as seen in Figure 3.23, while the carbon fiber filled ABS sections were imaged on a white background

because they are naturally dark due to their carbon fiber content. Slight differences in imaging also create different black and white images. The Amphora™ and carbon fiber images show black bead outlines on a white background, and the neat ABS show white bead outlines on a black outline. To make all the images consistent, the neat ABS images were then inverted to also show black outlines on a white background. Finally, any holes in the bead image were filled in so that the image showed the completely filled black shape of the bead cross section on a white background.

Once black and white images are produced, another "im" suite command called "bwboundaries" examines the image and determines the outline of the shape based on where the black pixels give way to white pixels. Finally, this boundary is stored as a series of coordinates that define the bead outline as pixel locations along the outside of the bead. The array of coordinates is the primary mathematical representation of the bead that allows the user to manipulate and determine aspects of the cross section bead geometry. An outline of the imaging process is shown in Figure 3.26.

It should be noted that the "im" suite in MatLab will occasionally recognize a different main feature of the image, if there are any impurities on the sample slide other than the cross section itself, such as small pieces of polymer or ink stains. In these cases, the initial image can be altered slightly to remove this defect, and the imaging software will recognize the correct main feature. Another potential imaging issue is ensuring that the cross section and any shadow it generates are separated by the threshold value, such that the black and white image will include the cross section outline without including any surrounding shadow. Ensuring shadow is not included in the cross section image requires trial and error to determine a threshold value that separates any potential shadow

from the bead cross section. Once the right threshold value is determined for a particular polymer, the same value can be used for all the samples of that polymer type.

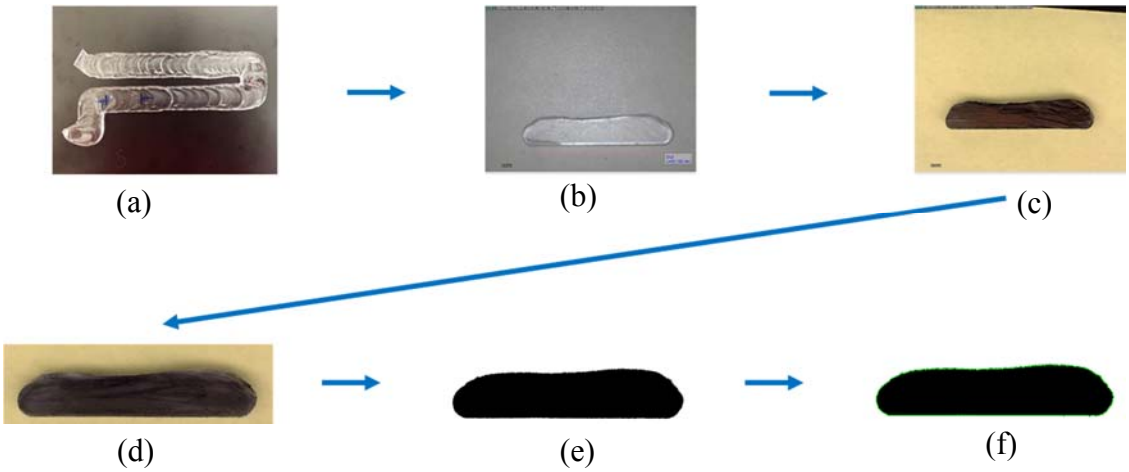

Figure 3.26. Imaging process of an Amphora™ bead cross section, from (a) printed bead to (b) cut, (c) dye, (d) crop, (e) black/white image, and (f) boundary trace.

CHAPTER FOUR

Data Analysis

Chapter Three describes the process by which polymer pellet samples were prepared through TGA testing and fiber distribution data, as well as how beads were printed on a moving platform. With samples printed and cut, the cross sections were then processed by imaging software and converted to coordinate data, which can then be analyzed using traditional mathematical software such as MatLab. Chapter Four describes the data analysis of the bead geometry, beginning with how data are created and stored in MatLab, and the evaluation of how each input parameter affects outputs of interest.

4.1 Flowrate and Freestream Analysis

With the images converted to boundary data arrays, the array data are easily available for manipulation to analyze and compare across parameters. The main goal of this thesis is to use cross section data to parameterize the large scale FFF system based on bead geometry and therefore gain a better understanding of large scale FFF deposition. Data analysis begins with a simple flowrate comparison.

4.1.1 Parameter Flowrate Analysis

To determine the flowrate for each cross section image, the cross-sectional area is calculated from the boundary. Area is easily determined using the “regionprops” command, which can store data about a region bounded by a perimeter, such as region

area and centroid. Once the area is calculated, flowrate is determined from the cross section thickness and plate velocity. To compare deposition flowrate values from bead cross sections, the density of each extruded polymer must be determined. Polymer density was calculated by summing the total area of all bead cross sections, multiplying by bead thickness, and dividing the total mass of all samples by their total volume:

$$\rho = \frac{\sum mass\_sections}{t * \sum bead\ cross\ section\ area} \tag{4.1}$$

The resulting density p was then used to calculate freestream flowrate by taking the freestream sample mass and dividing by the computed density:

$$V = \frac{\sum mass\_freestream}{\rho} \tag{4.2}$$

Figure 4.1 shows measured deposition flowrate compared to the freestream flowrate across the applicable ranges for nozzle height and platform velocity.

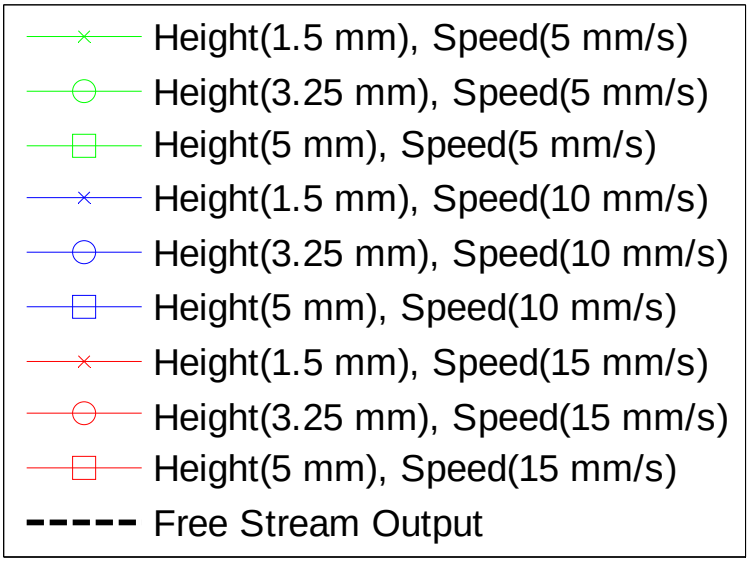

(a)

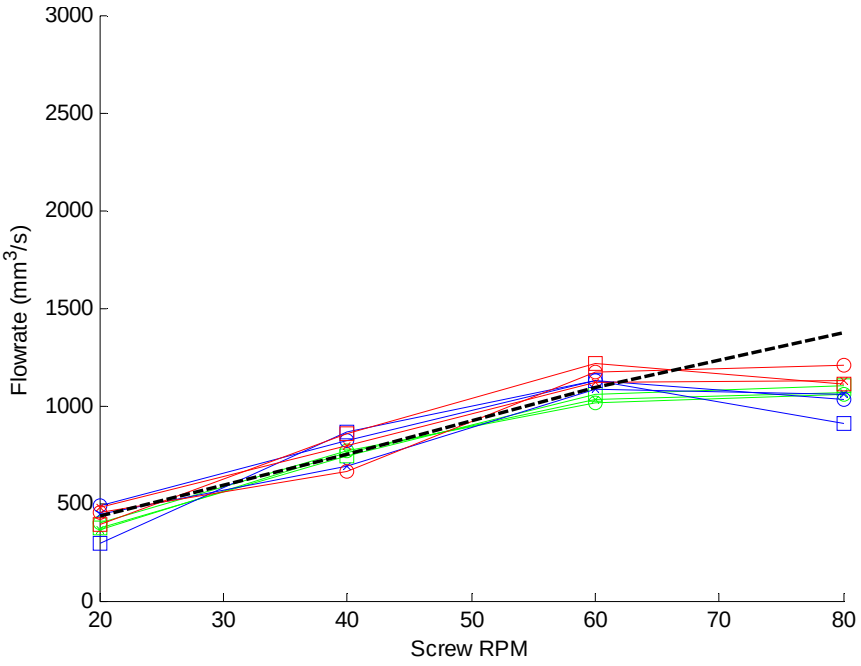
3000
2500
2000
1500
1000
500
0
Flowrate (mm3/s)
20
30
40
50
60
70
80
Screw RPM

(b)

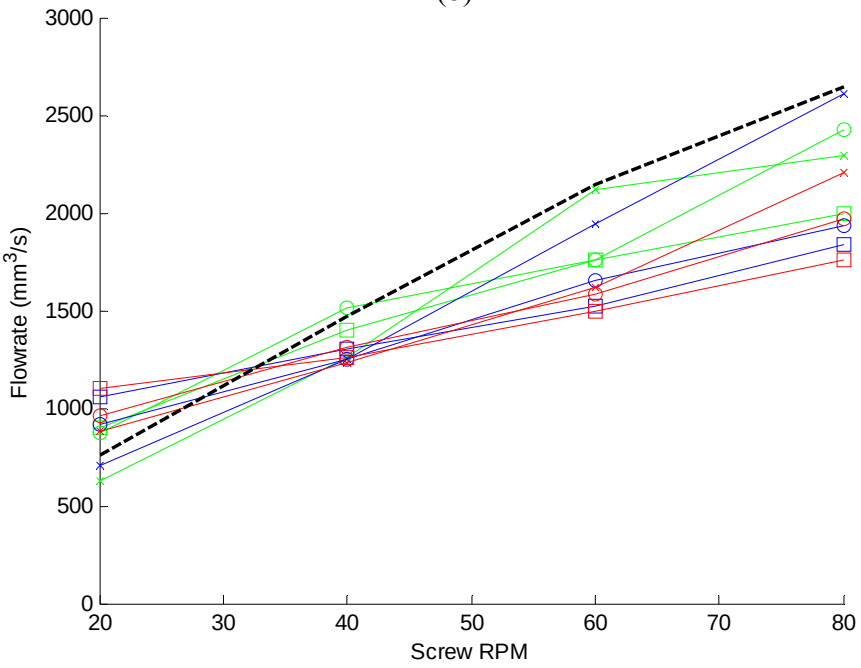
3000
2500
2000
1500
1000
500
0
Flowrate (mm3/s)
20
30
40
50
60
70
80
Screw RPM

(c)

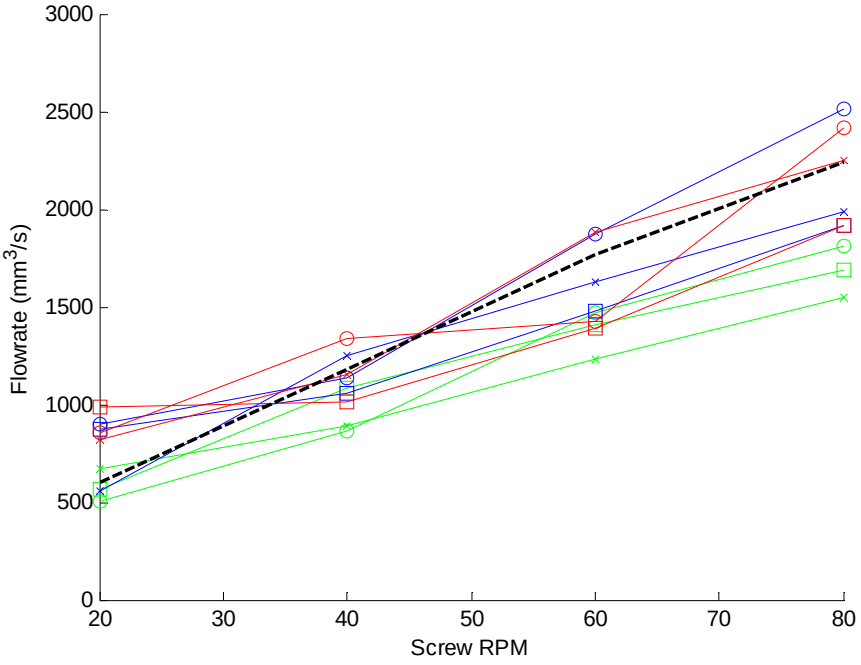

(d)

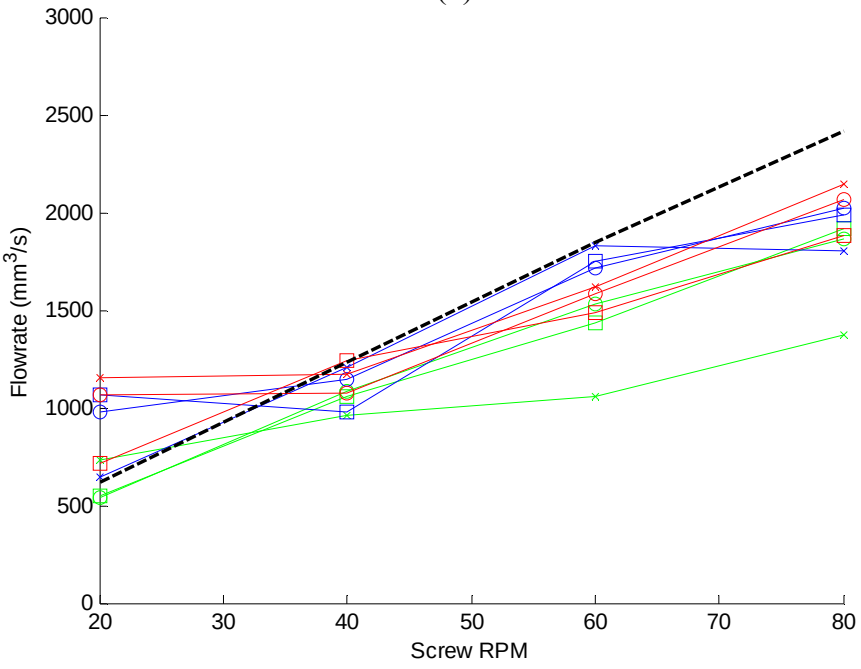

(e)

Figure 4.1. Interpretation legend (a) and freestream flowrate compared with bead flowrate for Amphora^{TM} (b), Neat ABS (c), 10% CF ABS (d), and 13% CF ABS (e).

The dashed black line represents the freestream output of polymer from the extrusion nozzle described in Chapter Three, indicating that the freestream flowrate creates an upper bound on the deposition flowrates at most parameter settings. There are a few exceptions, which are important to examine and clarify.

The first, most immediately obvious discrepancy is the freestream flowrate comparison for the Amphora™ polymer. The flowrate plot for Amphora™ shows the freestream output in the center of the bead geometry data, instead of creating an upper bound. As mentioned previously, the extruder flowrate pulsed when processing the Amphora™, which lead to the bead shapes having variation in width from deposition because the flowrate is constantly fluctuating. When analyzing individual beads and creating cross section slices, the effect of pulsing was minimized by selecting sections from a portion of a bead having a nearly constant cross section. Unfortunately, the flowrate data is still susceptible to fluctuation because the data for each RPM setting were collected using a constant stream of polymer over a period of three minutes. Therefore, the freestream data likely contain a notable amount of variability when compared to bead geometry data.

Five beads were printed at each RPM level and analyzed using image processing as described in Section 3.3.2. With the perimeter data of an entire bead, and assuming that cross sections are taken from the largest sections of each bead that represent the steady state flow region, a distribution of actual bead width can be estimated that indicates the volume lost due to pulsing. Freestream flowrate data were found to have decreased 12% from steady state flowrate based on the pulsing effect.

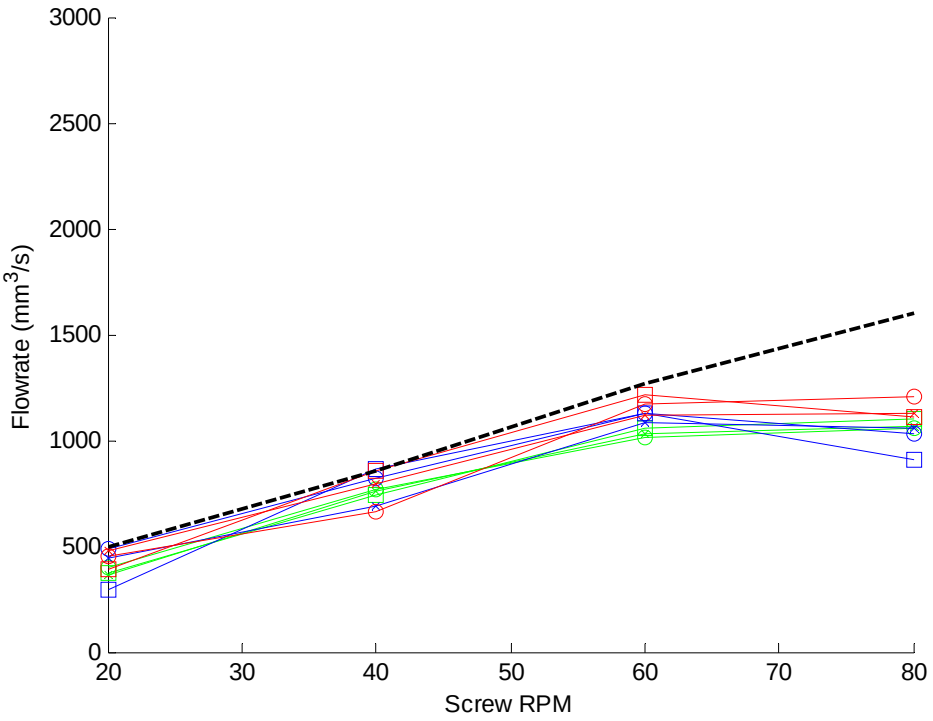

Figure 4.2 shows a revised plot of the freestream flowrate where the freestream data have been increased based on pulsing data, and the results indicate that pulsing had an adverse effect on freestream flowrate of Amphora^{TM}, and without the pulsing effect the freestream data create an upper bound for the Amphora deposition flowrate data.

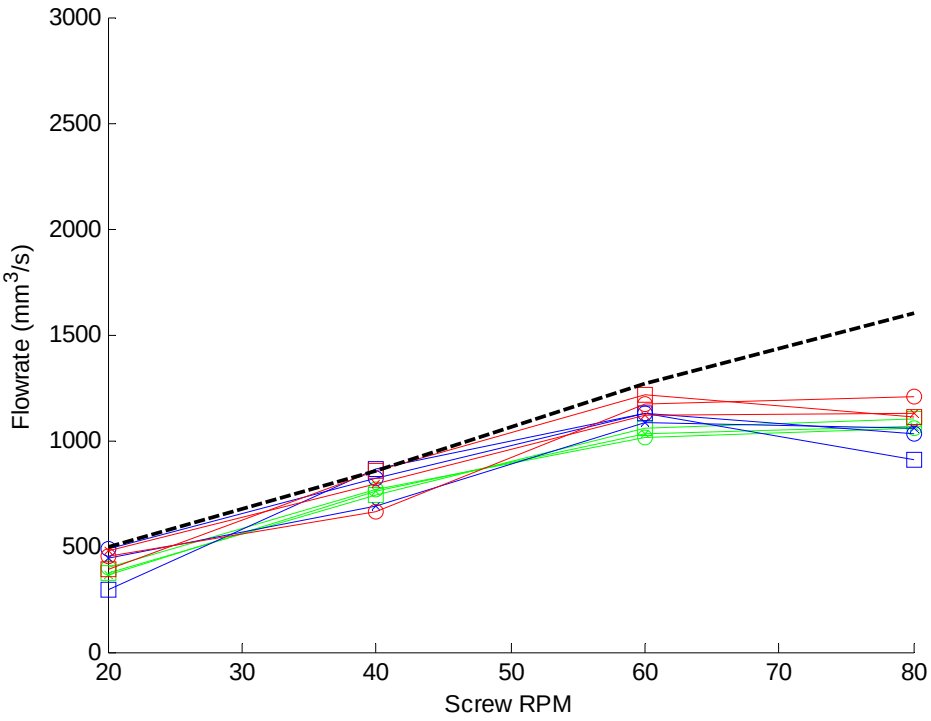

Figure 4.2. Revised Amphora™ freestream flowrate to compensate for pulsing effect.

Another important observation about the Amphora™ data is that the maximum flowrate is approximately 1500 mm^3/s, whereas the neat ABS and carbon fiber filled ABS polymers have maximum flowrates of approximately 2500 mm^3/s. In comparison with the Melt Flow Index data from Section 3.2.1, Amphora™ had the highest flowrate, suggesting an intrinsic difference between the flowrate mechanisms of capillary and extrusion flow because capillary dominated flow would suggest that the Amphora™ should have the highest flowrate. A large difference in maximum flowrates also supports the conclusions from Section 3.1.1 that the extruder does not process Amphora™ at rates as high as seen for the ABS blends. Also, the bead shape flowrate slope decreases significantly from 60 to 80 RPM over all parameter values studied for the Amphora™, which suggests that an upper bound on flowrate is likely as RPM is increased. A diminishing flowrate trend from 60 to 80 RPM is only observed in the bead flowrates as

compared to the freestream flowrate, which indicates that the increased pressure of laying the polymer on the plate, along with the increasing RPM, is creating a pressure drop that decreases extruder flowrate. The force required for the screw to slip relative to the molten polymer in the barrel becomes lower at high RPM than the force required to overcome the pressure differential from the platform, creating an upper bound on flowrate.

Additionally, it can be seen in Figure 4.1 that the flowrate values for Amphora™ at 20 RPM are slightly higher than the freestream flowrate at 20 RPM. Higher deposition flowrates than freestream flowrates are somewhat concerning because the freestream flow should create an upper bound on the possible flowrates for the platform beads. However, a similar effect also occurs at low both low RPMs with ABS and high RPMs with Amphora™, where the platform motion appears to influence flowrate. At low RPMs, the flowrate from the screw is significantly lower such that little polymer is being deposited on the platform. The platform moves at a constant speed for all RPMs, which generally means that the bead cross sectional area increases with RPM and decreases with platform velocity. Therefore, at low RPMs, the platform is moving quickly relative to the velocity at which the polymer is being extruded through the nozzle. At higher RPMs, the velocity difference causes the polymer bead to expand horizontally and vertically to accommodate the flowrate. However, at lower RPMs the platform is effectively pulling the bead along, slightly increasing the flowrate out of the nozzle as the friction forces in the barrel are partially negated by the forces required to stretch and neck the ABS bead. It can be observed that a majority of the parameter settings at the lowest speed are bounded by the freestream flowrate, while the higher speed parameter settings show an increase in flowrate due to the effect of the platform pulling the bead.

Based on the results from the melt flow indexer in Figure 3.19, the Amphora™ polymer has a significantly lower viscosity at operating temperatures than do the ABS polymers. At first observation, Amphora™, having the lowest viscosity, would suggest a conflicting result with the flowrates presented in Figure 4.1 because a higher viscosity should lead to greater pressure drop in the capillary-dominated flow in the nozzle. An examination of the characteristic screw equation for Newtonian fluids combined with capillary effects helps to resolve the flowrate vs. viscosity discrepancy [64]:

$$Q = \frac{\frac{1}{2}\pi D_b N cos(\varphi_b) WH}{1+(WH^3 \sin(\varphi)/(12\mu L_b K_D)} \tag{4.3}$$

where Q is the flowrate, D_b is the extrusion barrel diameter, W is the screw channel width, H is the screw channel height, N is the angular velocity of the screw, φ_b is the channel angle of the screw helix, φ is the mean screw helix angle, μ is the viscosity of the fluid, L_b is the extrusion barrel length, and K_D is the die characteristic constant. In the melt section of the screw, polymer flow is dominated by viscous drag, and toward the end of the screw pressure increases to overcome pressure drop in the nozzle. However, equation (4.3) indicates that pressure buildup has the opposite effect by reducing flowrate directly proportional to the pressure buildup along the length of the screw and inversely proportional to the viscosity of the fluid. From equation (4.3), it can be shown that increasing viscosity actually causes an increase in flowrate. It can be further inferred from the experimental results in Figure 4.1 that the flowrate losses due to capillary dominated flow in the nozzle, losses that increase proportionally with viscosity, are offset by pressure gains due to high viscosity in the screw section dominated by viscous drag forces. Results from the melt flow indexer show flowrate values for Amphora™ 4-6

times higher than the ABS blends, meaning that Amphora™ has a much lower viscosity and would produce lower extrusion flowrates as per equation (4.3).

4.1.2 Bead Cross Section Analysis

Bead cross sections are created over all parameter values studied for each of the polymer types, described here in terms of the aspects of bead shape that lend themselves well to FFF, and some of the aspects that are detrimental to the FFF process. A more in-depth analysis of specific shape parameters will follow in Section 4.2.

Amphora™ bead shapes. As previously mentioned, the Amphora™ polymer is specifically targeted for use in the FFF process, so ideally the bead shapes from this polymer would demonstrate a wide range of applicable parameter settings to make full use of Amphora's intended purpose. Figure 4.3. shows the Amphora™ bead shapes in subplots grouped by nozzle height.

Note that there is little variation in the shape characteristics of the Amphora™ beads. Amphora™ bead cross sections are somewhat rectangular with curved edges, and vary in aspect ratio based on nozzle height and flowrate. For example, the 1.5 mm nozzle height beads are thinner overall than the 5 mm nozzle height beads, but both sets retain a high degree of rectangular similarity.

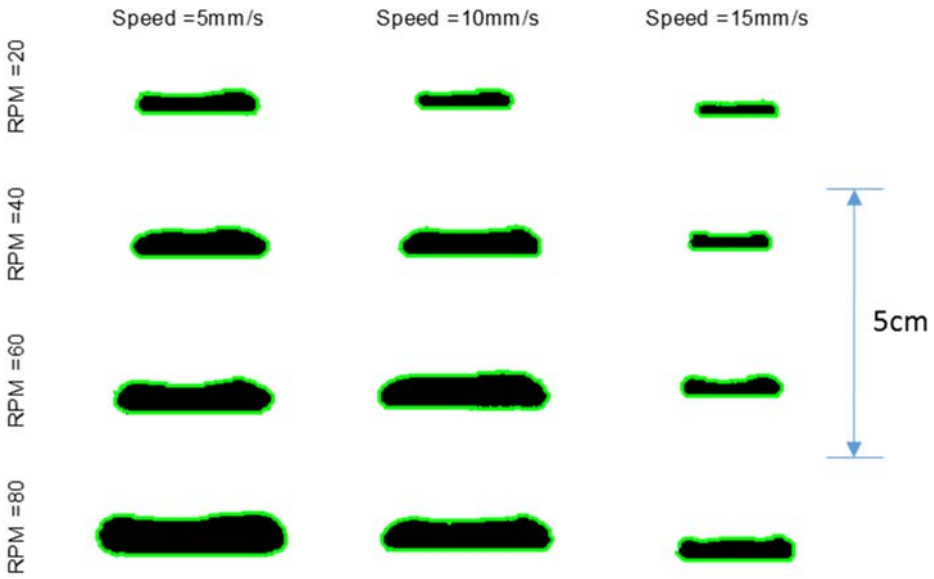
Speed =5mm/s
Speed =10mm/s
Speed =15mm/s
RPM =20
RPM =40
RPM =60
RPM =80
5cm

(a)

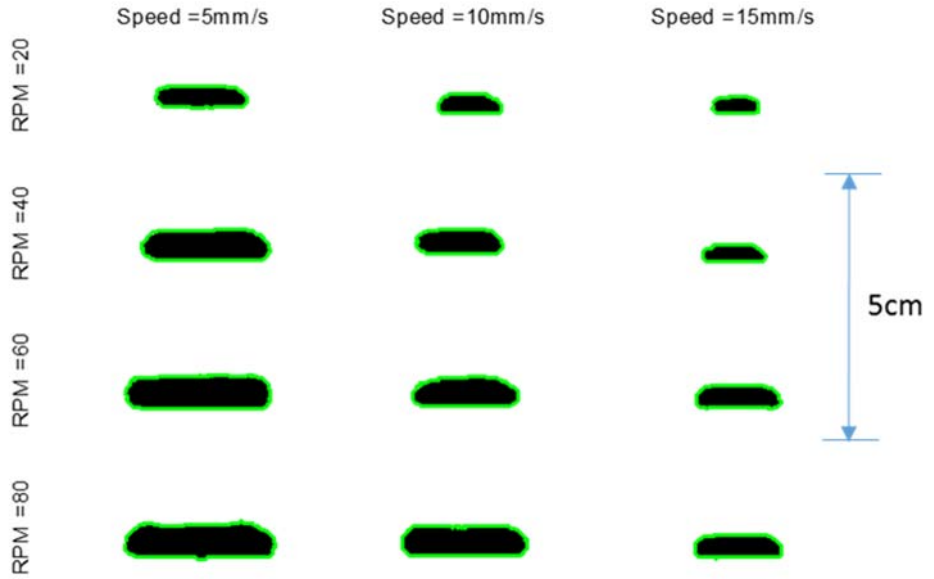
Speed =5mm/s
Speed =10mm/s
Speed =15mm/s
RPM =20
RPM =40
RPM =60
RPM =80
5cm

(b)

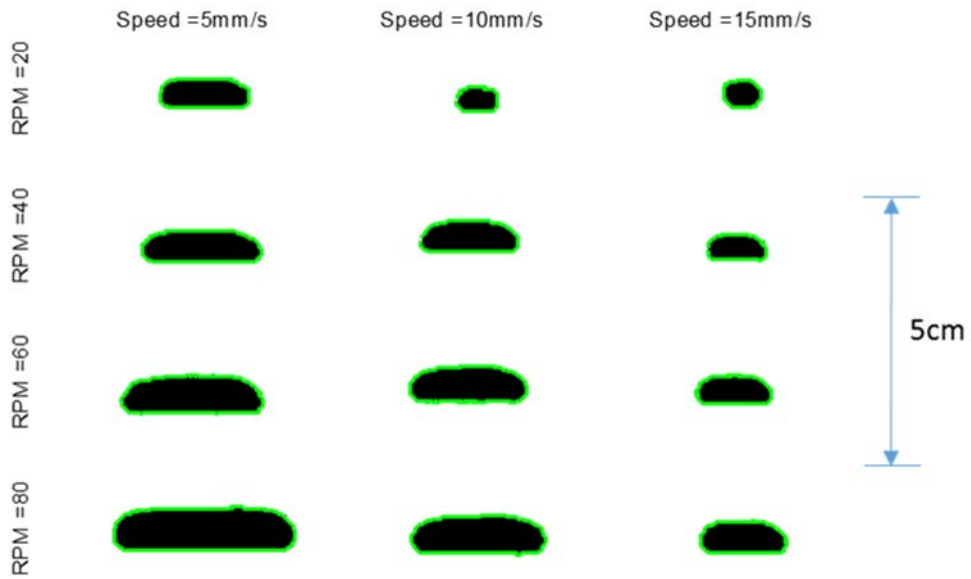

(c)

Figure 4.3. Amphora™ bead cross sections over all parameter values studied, at nozzle heights of (a) 1.5, (b) 3.25, and (c) and 5 mm. Printed at a platform temperature of 65°C and an extrusion temperature of 240°C.

A slight inward curvature can be seen on the top surfaces in the 1.5 mm beads, which is mainly an effect due to the swelling of the polymer near the outer edge of the bead. The minimal distance between the nozzle and the platform creates back pressure that decreases the flowrate, as shown in Figure 4.1, but the remaining polymer flow must be deposited onto the plate, causing expansion in the horizontal direction. For the lowest nozzle height (1.5 mm), the effect of horizontal swelling also creates a slight vertical swelling on either side of the nozzle, causing concavity at the top of the beads. Curvature along the top of the beads is not observed at the larger nozzle heights because the polymer has more vertical space between the platform and the nozzle.

Cross-sectional area was found to vary with RPM and table velocity, each of which directly affect the amount of polymer being deposited within a bead section.

Overall, bead area increases with increasing screw RPM and decreases with increasing table velocity. The two bead cross section settings that are most similar in area are the 60 and 80 RPM beads, which appear to maintain or even slightly decrease in area from the increase in RPM. In comparison to the plot in Figure 4.1, the flowrate slope over all parameter values studied decreased significantly as RPM increased from 60 to 80, which matches well with the similar area observation in beads at 60 and 80 RPM in Figure 4.3.

Trends in bead shape based on nozzle height are more difficult to determine because nozzle height does not directly contribute to a change in flowrate; rather, a change in nozzle height effects the shape of the bead more than it does area, and causes a change in the amount of backpressure experienced in the screw. The aspect ratio of the beads changes with nozzle height, where beads with the lowest nozzle height tend to have horizontally elongated shapes with minimal height, whereas beads from the highest nozzle height tend to be thicker rectangles with an aspect ratio closer to unity. For example, the bead cross section printed at 5 mm/s platform velocity, 20 RPM, and 1.5 mm nozzle height has an thin, elongated shape, whereas the bead cross section printed at 5 mm/s, 20 RPM, and 5 mm nozzle height is significantly more compact and square.

Neat ABS bead shapes. ABS is a common FFF material, used in many small scale FFF systems for general prints. Figure 4.4 shows the neat ABS bead shapes in subplots grouped by nozzle height.

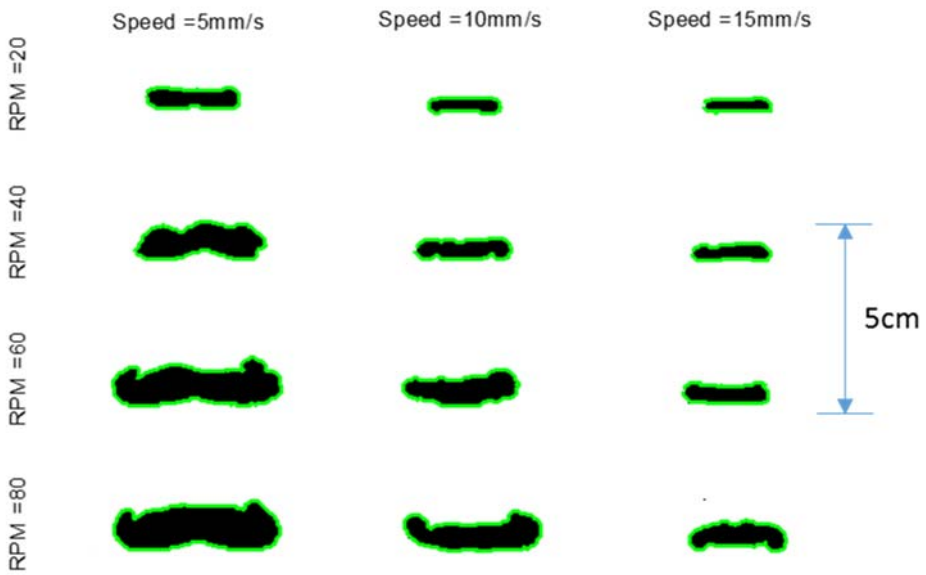
Speed =5mm/s
Speed =10mm/s
Speed =15mm/s
RPM =20
RPM =40
RPM =60
RPM =80
5cm

(a)

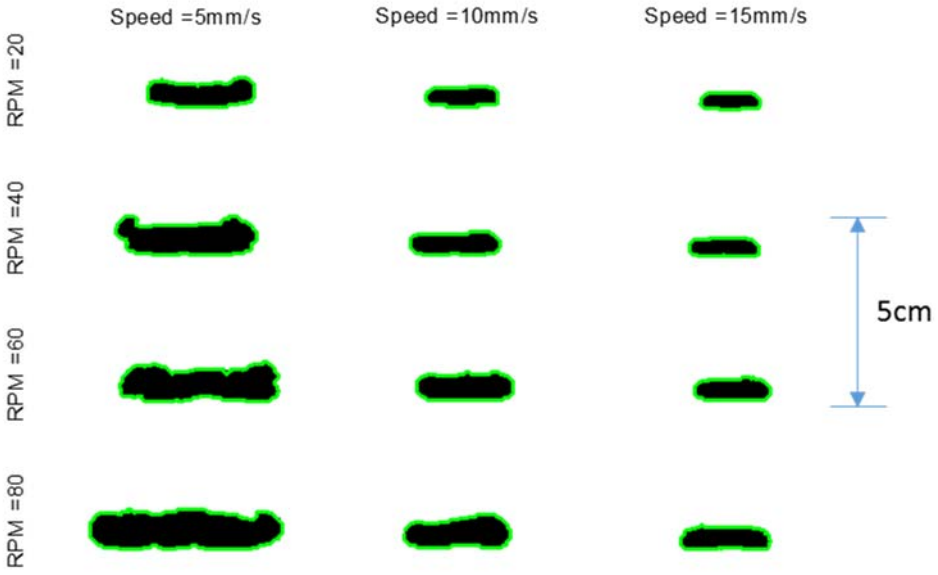
Speed =5mm/s
Speed =10mm/s
Speed =15mm/s
RPM =20
RPM =40
RPM =60
RPM =80
5cm

(b)

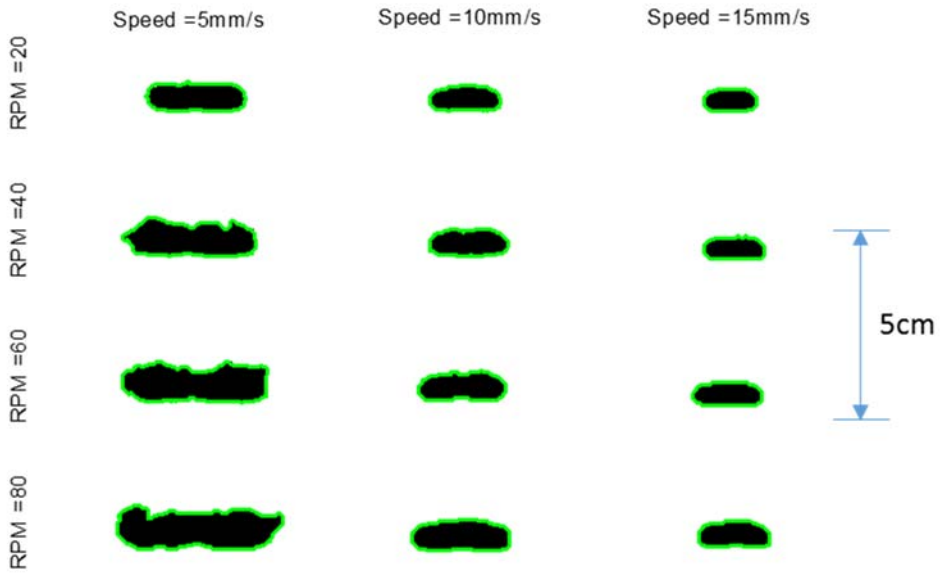

(c)

Figure 4.4. Neat ABS bead cross sections over all parameter values studied, at nozzle heights of (a) 1.5, (b) 3.25, and (c) and 5 mm. Printed at a platform temperature of 65°C and an extrusion temperature of 230°C.

Comparing Amphora™ and ABS beads, it is apparent that neat ABS exhibits more surface roughness when compared to Amphora™. While the Amphora™ beads have a highly regular, rectangular-oval shape, neat ABS beads can be irregular with projections and regions along the bottom of the bead that do not contact the build platform. Failure of the ABS bead to stick to the build platform is typical with FFF-ABS prints. One of the primary concerns with ABS printing is preventing the print from peeling off of the plate as it cools, which is more likely given ABS's high CTE.

Bead cross sectional area for the ABS follows similar trends to Amphora™, where cross-sectional area increases with increasing RPM and decreases with increasing platform velocity. A comparison of Figure 4.4 with Figure 4.1 reveals that the slope decrease between 60 and 80 RPM that exists for Amphora™ does not occur in the ABS

processing, indicating that the screw is not apparently not approaching its upper bound for processing flowrate with ABS. Confirming this observation, the neat ABS beads at 80 RPM are notably larger than those at 60 RPM.

The beads at the lowest table velocity appearing in Figure 4.4(a) are more asymmetric than those at higher speeds in Figure 4.4(b,c), revealing that the lowest platform speed produces undesirable cross sections for all parameter combinations, while the higher velocities produce more regular shapes. The higher velocities also tend to lay more flat against the platform and do not contract inward at the center or curl at the edges. For example, the bead deposited at 5 mm/s platform velocity, 80 RPM, and 5 mm nozzle height is much more eccentric than the bead deposited at 15 mm/s platform velocity, 80 RPM, and 5 mm nozzle height.

ABS bead aspect ratio varies with nozzle height, as with the Amphora^{TM}, but less notably due to the eccentric shapes. The lower nozzle height beads have higher aspect ratios, but also have more unusual cross sections, making aspect ratio a somewhat poor metric for comparison. Aspect ratio is calculated as the ratio of bead width to bead height, and irregularities in bead shape at lower platform velocities influence the ratio. Aspect ratio decreases with increasing nozzle height, a trend which is more evident at higher table velocities due to the abnormal shapes in the lower velocity beads.

10% carbon fiber filled ABS. The addition of chopped carbon fiber as a filler for ABS has two main goals: increase the modulus using carbon fiber's high Young's modulus relative to ABS, and decrease the high coefficient of thermal expansion of ABS by taking advantage of carbon fiber's negative axial coefficient of thermal expansion. For FFF prints with high expected loading conditions, it is imperative to strengthen the

polymer with reinforcing fibers, and therefore the addition of carbon fibers supports the application of FFF for industrial parts. The beads in Figure 4.5 were printed using neat ABS with 10% by mass carbon fiber, as confirmed in TGA tests from Chapter Three.

Cross sections in Figure 4.5 show that 10% carbon fiber filled ABS beads produce significantly different bead shapes than the neat ABS at comparable parameter settings. While the neat ABS polymer tends to make elongated beads with high aspect ratios, the carbon fibbed filled ABS tends to create curved bead geometries that are roughly "U"-shaped, indicating that there is a notable difference in processing carbon fiber ABS compared to neat ABS. It is speculated that embedded fibers in the polymer matrix during the extrusion process cause fibers to bend and twist, which creates internal elastic stresses. Internal stresses relax toward a zero stress state after exiting the nozzle, which causes the bead to curl as the fibers relax from being contorted in the extruder.

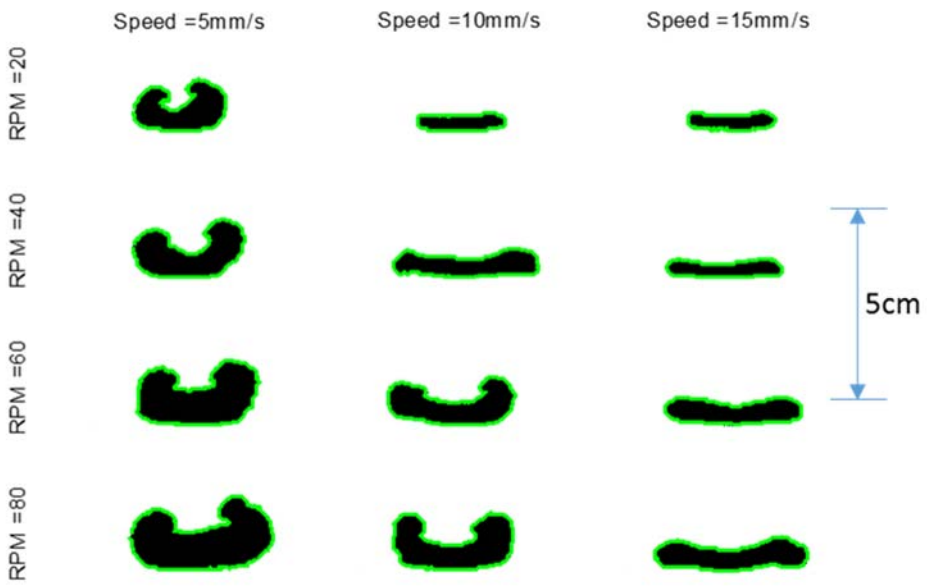

(a)

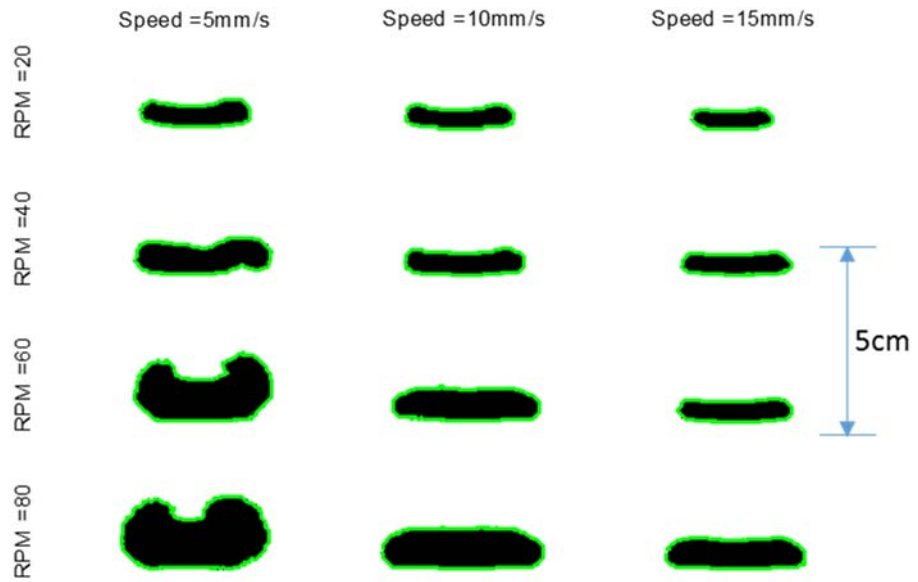

(b)

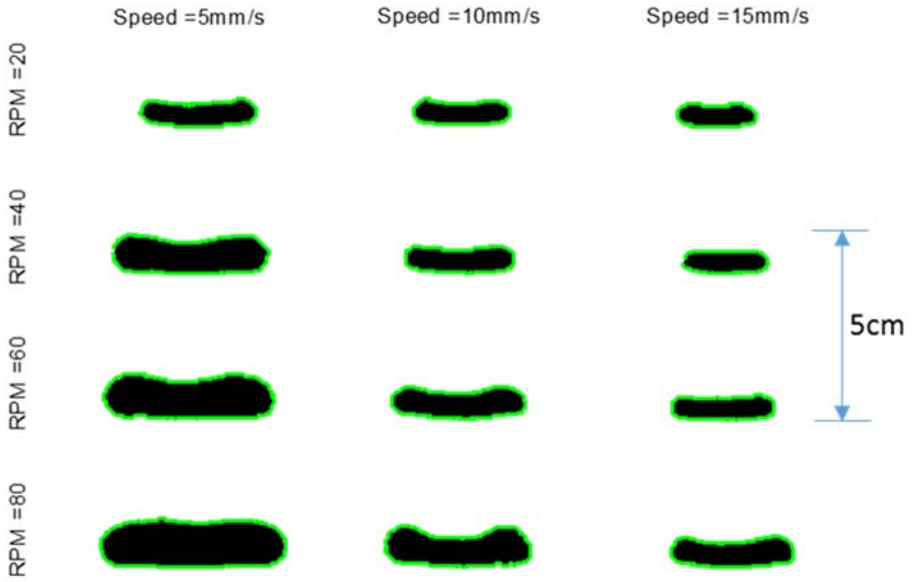

(c)

Figure 4.5. 10% carbon fiber filled ABS bead cross sections over all parameter values studied, at nozzle heights of (a) 1.5, (b) 3.25, and (c) and 5 mm. Printed at a platform temperature of 65°C and an extrusion temperature of 230°C.

Most of the beads at the 1.5 mm nozzle height show some degree of curling, seen primarily at the 5 mm/s platform speed with the effect lessening as the platform velocity increases. Some curling is still seen at the higher nozzle height of 3.25 mm, while little is seen at any parameters in the 5 mm nozzle height cross sections, which indicates a trend toward increasingly irregular shapes with decreasing nozzle height.

The 10% carbon fiber filled beads, while somewhat eccentric in shape, tend to have smoother boundaries than the neat ABS, indicating that the inclusion of fibers produces a smoother surface bead than ABS alone. Smoother cross sections with carbon fiber inclusions is likely due to the fiber reinforcement within the polymer matrix providing dimensional stability within the bead, making it less likely for small, rough surface features to form.

Cross-sectional area trends also exist for the carbon fiber filled ABS as with the neat ABS and Amphora^{TM} polymers, with increases in RPM resulting in increases in area, and increases in platform speed causing a decrease in area. In comparison with Figure 4.1, flowrate can be equated to area through the cross section thickness, and these trends can be observed as well.

Aspect ratio is more difficult to establish due to the curvature of the cross sections, which somewhat reduces the usefulness of aspect ratio as a viable parameter. However, it can be noted that the 10% fiber filled ABS beads tend to trend opposite than the neat ABS and Amphora^{TM} beads. Here aspect ratio increases with platform velocity and decreases with RPM, because higher RPM and lower platform velocities cause the beads to curl inward.

13% carbon fiber filled ABS. In this study, the observation of bead effects between 10% and 13% carbon fiber should give a good indication of the effects of changing volume fraction on geometry parameters, and help to determine a range of optimum values for carbon fiber filled polymers for FFF printing. It is important to note here that the base polymer blend of ABS used for the 10% and the 13% carbon fiber filled beads have inherently different chemistry, so all observations between these two polymers could also be caused by differences in inherent polymer chemistry. Bead cross sections for 13% carbon fiber filled ABS beads are shown in Figure 4.6.

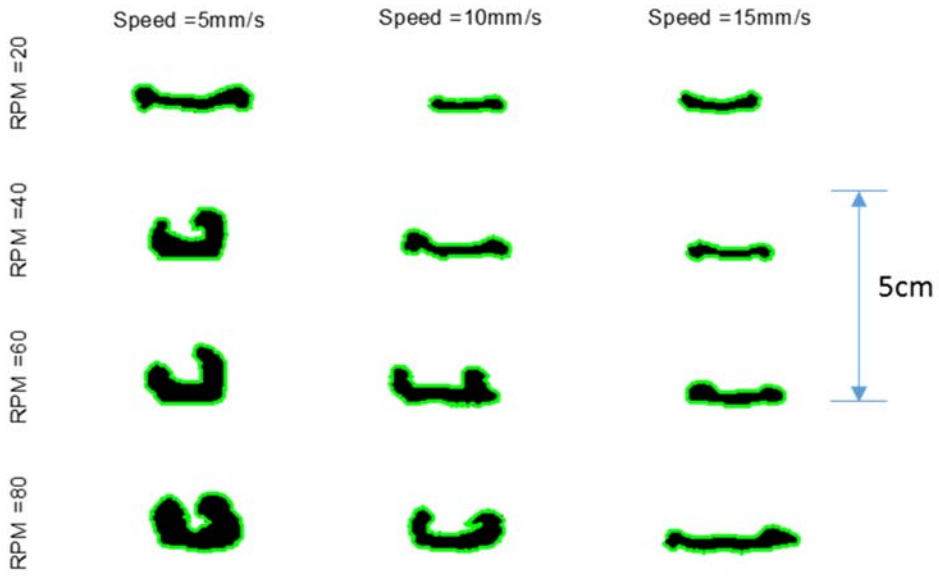

(a)

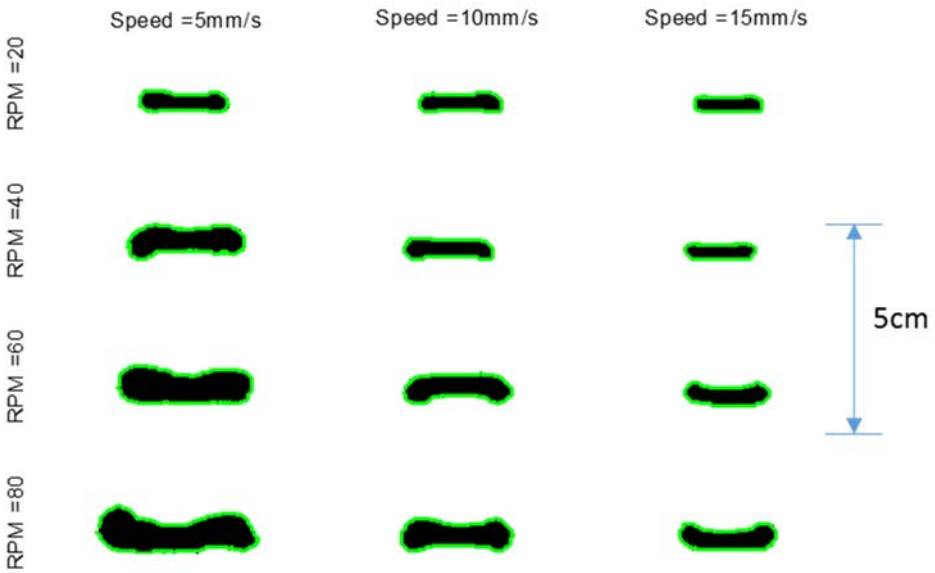

(b)

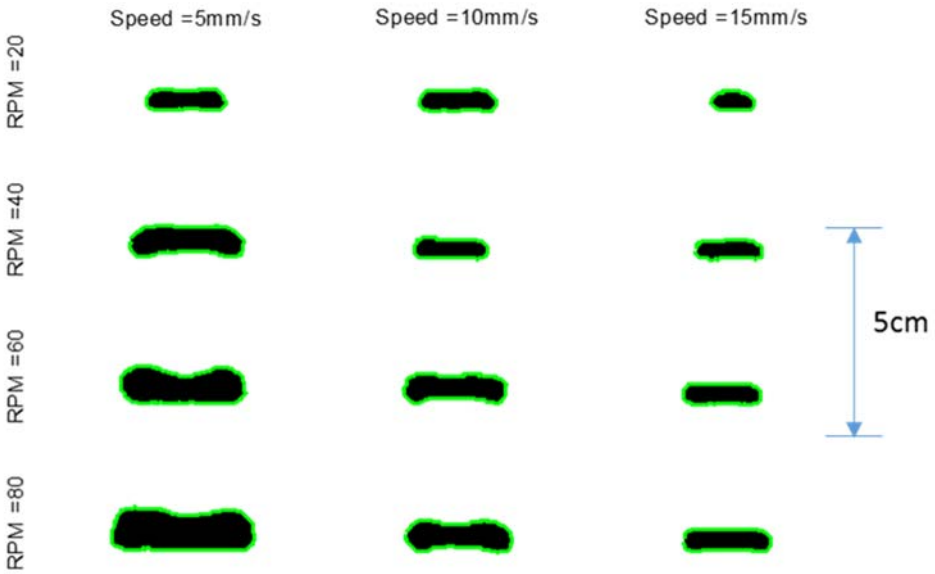

(c)

Figure 4.6. 13% carbon fiber filled ABS bead cross sections over all parameter values studied, at nozzle heights of (a) 1.5, (b) 3.25, and (c) and 5 mm. Printed at a platform temperature of 65°C and an extrusion temperature of 230°C.

Increased curvature exists in the 13% carbon fiber filled ABS beads as compared to the neat ABS beads. It follows that if the fiber inclusions are causing the curvature in the bead, then the 13% carbon fiber filled bead would exhibit similar curvature as those of the 10% carbon fiber filled beads, even though the two polymers are different blends of ABS. Curvature is more evident across a greater range of parameters in the 13% carbon fiber beads than in the 10% carbon fiber beads, demonstrating fewer parameters that produce acceptable bead shapes.

The reason for including carbon fibers is to increase dimensional stability and strength of printed parts by decreasing warping and altering the composite properties. While the print bead is still above melt temperature, however, the polymer matrix is susceptible to internal elastic stresses within the fibers, which, in turn, creates the curvature effect. To minimize curvature and take advantage of the improved mechanical properties due to fiber inclusions, process parameters need to be found that minimize bead curvature directly out of the nozzle before the polymer has a chance to cool and solidify.

Once again, cross sectional area tends to increase with RPM and decrease with table velocity, as can be seen from the cross sections as well as a comparison with the flowrates in Figure 4.1. Area also increases with increasing nozzle height, an effect of the decrease in backpressure created by having the platform close to the nozzle exit. As nozzle height increases, distance between nozzle and the platform is increased, providing less pressure loss and increasing flowrate, thereby increasing area.

ABS with 13% carbon fiber also exhibits boundaries that are also smoother than the neat ABS beads, indicating that the carbon fiber creates a smoother macro surface

finish than the neat ABS, and that the fibers do not facilitate the formation of eccentric surface features. Aspect ratio, as with the 10% carbon fiber filled ABS beads, is difficult to gauge due to the curvature of the beads. However, the trend is essentially opposite of the Amphora™ and neat ABS beads, where aspect ratio increases with increasing platform velocity and increases with increasing RPM.

4.1.3 Error Analysis

It is important here to examine the experimental error inherent in the data collected. Each data point shown in Figure 4.1 for flowrate analysis is an average of three data points taken from the deposited bead at each deposition parameter settings group. From these data points, the standard deviation of the data can be determined:

$$\sigma = \sqrt{\frac{1}{n}\sum_{i=1}^{n}(x_i - \mu)^2} \tag{4.4}$$

where σ is the standard deviation of the data set, n is the number of data points in the set, x_i is the specific data point in the summation, and μ is the mean of the data. All data was collected using the same experimental methods and MatLab code; therefore an examination of the freestream Amphora™ data error will give a good representation of the overall experimental error associated with our study. Plots of Amphora™ flowrate data separated by nozzle height are shown in Figure 4.7, with error bars included at $\pm\sigma$.

With one exception, the errors shown in Figure 4.7 are small compared to the flowrate data gathered. The largest error associated with the Amphora™ cross sections is at the nozzle height of 5 mm, platform velocity of 15 mm/s, and RPM of 80. This large error is most likely due to the data collection used for the Amphora™ beads, which was

slightly subjective because of the pulsing effect of the extruder on bead deposition. Therefore, the error associated with this data point is not a cause for concern.

To quantify the error in the Amphora™ plots from Figure 4.7, coefficient of variation was used which is the ratio of standard deviation in equation (4.4) to the mean of the data:

$$C_v = 100\frac{\sigma}{\mu} \tag{4.5}$$

where C_v is the coefficient of variation ratio. Values given by equation (4.5) are unitless because they are scaled by the mean of the data, giving a percentage of the data covered by the standard deviation. "Good" data have a low C_v, typically at or below 5%. Our data sets, with the exception of the one outlying data set, all have a coefficient of variation at or below 5%, indicating that the data sets have "good" experimental agreement. Coefficient of variation values for the Amphora™ are shown in Table 4.3.

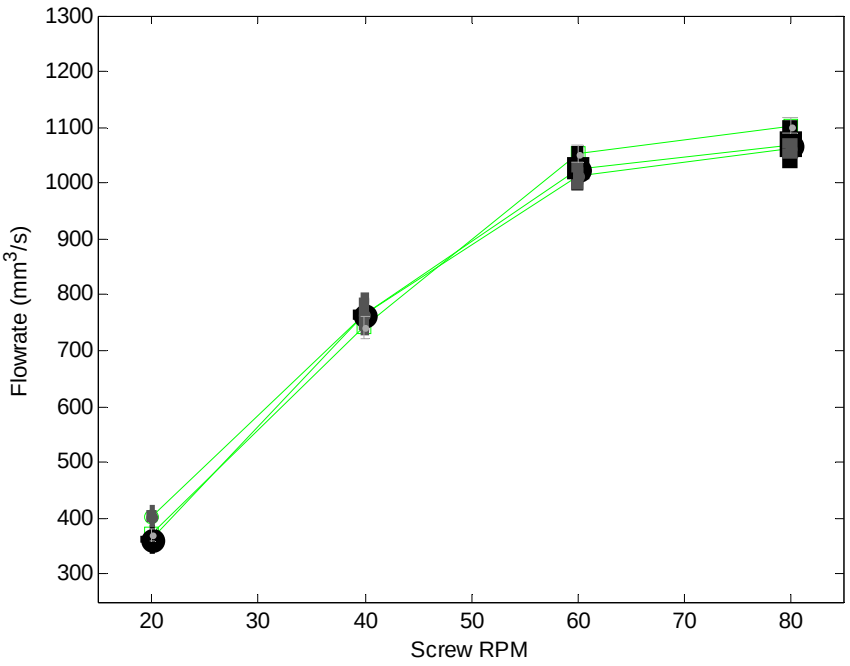

(a)

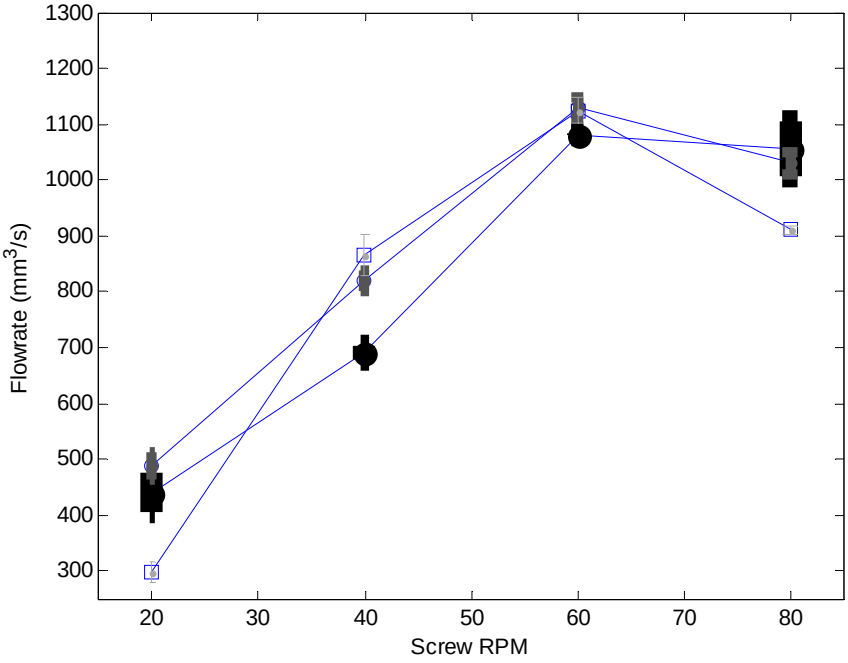

(b)

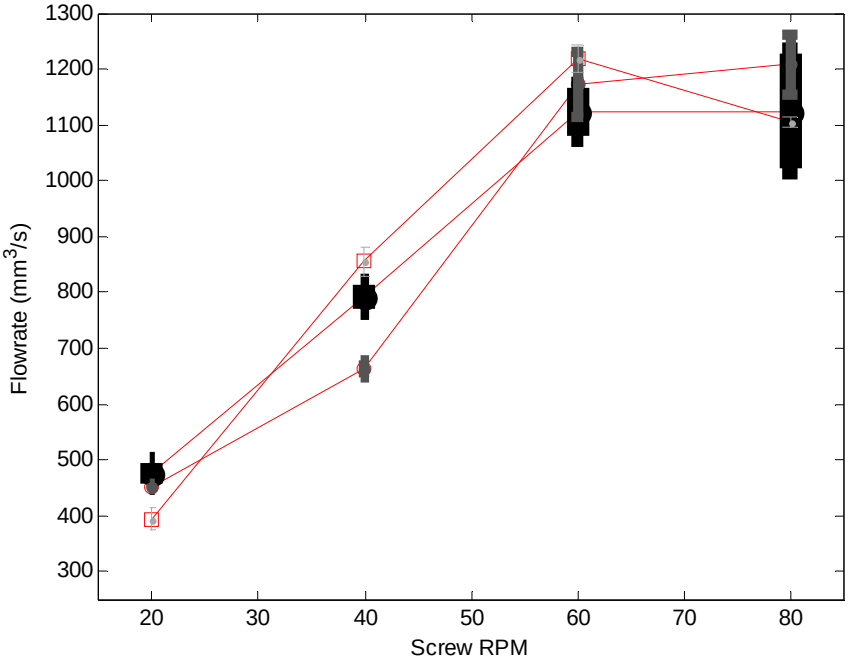

(c)

Figure 4.7. Amphora™ flowrate data with error bars for (a) 1.5, (b) 3.25, and (c) 5 mm nozzle heights.

Table 4.3. Flowrate Coefficient of Variation Values for Amphora™.

Platform Velocity	Nozzle Height	RPM			
-	-	20	40	60	80
	1.5 mm	2.71	3.77	1.52	0.88
5 mm/s	3.25 mm	1.31	2.15	0.26	1.97
	5 mm	1.32	2.05	2.60	1.60
	1.5 mm	0.26	1.56	4.85	1.53
10 mm/s	3.25 mm	0.87	1.09	0.93	3.53
	5 mm	0.99	0.97	1.02	0.52
	1.5 mm	0.67	2.77	1.48	2.47
15 mm/s	3.25 mm	2.02	1.07	1.16	2.95
	5 mm	0.94	0.95	0.92	1.11

An error analysis was also performed for the neat ABS, to compare the relative error between polymers. It is assumed that because the Amphora™ data is subject to the pulsing that affects cross section selection, it will have the highest error because the other three polymers, neat ABS, 10% carbon fiber filled ABS, and 13% carbon fiber filled ABS, all reach and maintain a reliable steady state deposition flow. Neat ABS flowrate data with $\pm\sigma$ error bars are shown in Figure 4.8.

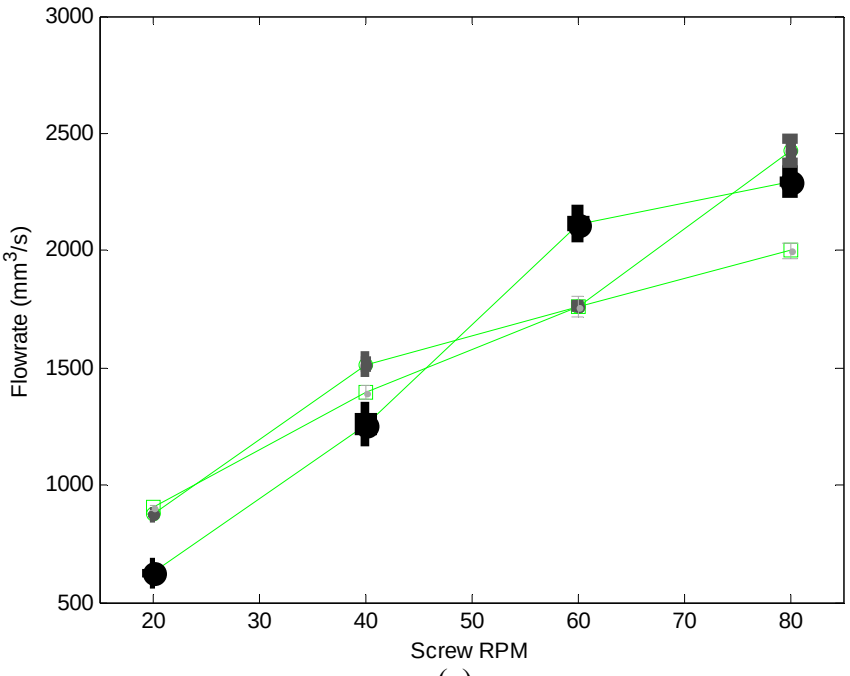

(a)

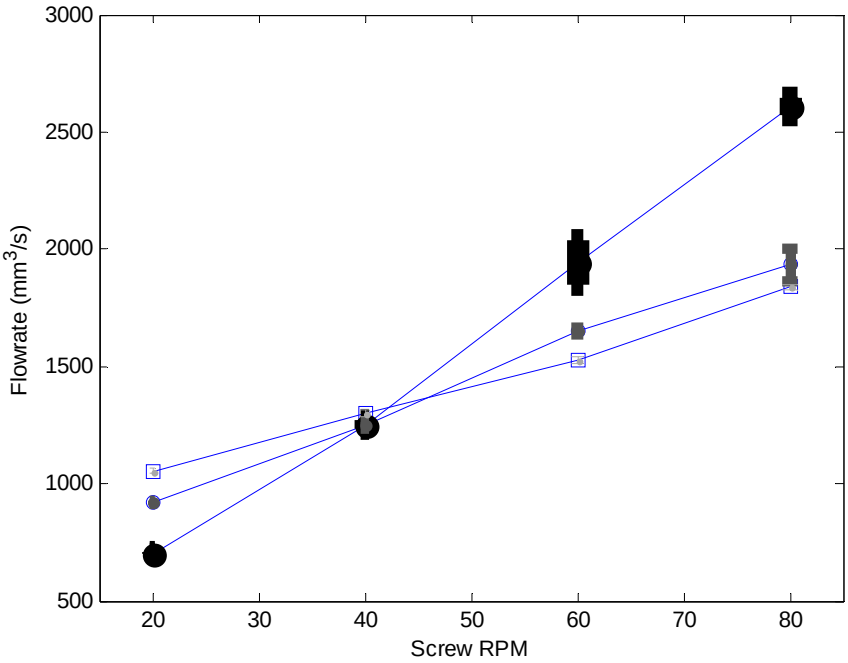

(b)

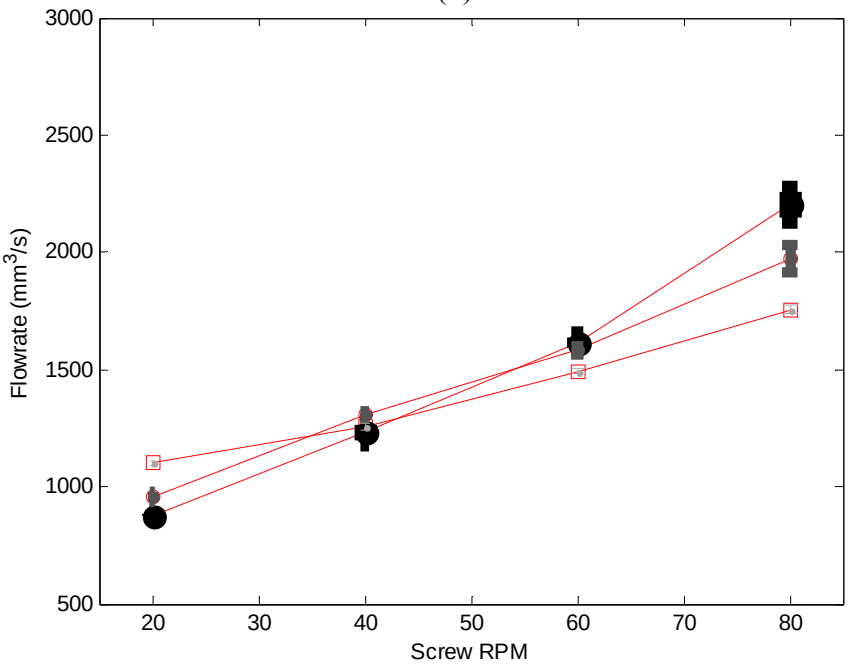

(c)

Figure 4.8. Neat ABS flowrate data with error bars for (a) 1.5, (b) 3.25, and (c) 5 mm nozzle heights.

As seen in Figure 4.8, the error bars for the neat ABS data are much smaller than the error bars for the Amphora™ data in Figure 4.7. Values for coefficient of variation

are also significantly smaller for the neat ABS, with C_v values at all parameter settings below 3%. Coefficient of variation values for the neat ABS are summarized in Table 4.4.

Table 4.4. Flowrate Coefficient of Variation Values for Neat ABS

Platform Velocity	Nozzle Height	RPM			
-	-	20	40	60	80
	1.5 mm	1.74	1.20	1.83	2.07
5 mm/s	3.25 mm	2.86	3.85	1.46	0.91
	5 mm	2.85	2.63	1.43	1.29
	1.5 mm	8.07	1.86	0.10	4.64
10 mm/s	3.25 mm	5.09	2.21	1.64	1.98
	5 mm	6.31	4.37	1.93	0.89
	1.5 mm	3.89	2.67	3.87	9.02
15 mm/s	3.25 mm	0.99	2.33	5.04	4.55
	5 mm	5.20	3.20	2.07	0.85

Finally, it is important here to discuss measurement error inherent in the image analysis process, to determine how accurately the images can be analyzed and identify any sources of error. All images were captured at a pixel resolution of 1280x1024 pixels, and image analysis creates the boundary array based on pixel location. Therefore, some small error may be introduced depending on where MatLab interprets the edge of the bead to be, especially if there is any shadow around the edges of the bead. However, this error is on the order of less than five pixels, which is much lower in magnitude than the error introduced by taking multiple samples, and therefore does not add to data error.

All data analyses in our study are based on the cross sections analyzed in Section 4.1 using the same image analysis techniques. Therefore, it is assumed that all analyses reflect the same error as described in this section.

4.2 Bead Geometry Parameter Analyses

In Section 4.1, deposition parameter dependent trends were discussed that apply to bead cross sections for each specific polymer. In this section, specific geometry parameters are examined to identify parameter settings that are "good", ideal for FFF printing, and "bad", having one or more aspects that are less than satisfactory for use in FFF. For all specific bead shape parameter plots in this section, refer to Figure 4.9 for a legend interpretation.

Figure 4.9. Interpretation legend for specific parameter plots.

4.2.1 Bead Aspect Ratio

A common measurement for comparing geometry is aspect ratio, defined as the ratio of the width to the height of the same shape. The equation for aspect ratio is:

$$A_R = \frac{W}{H} \tag{4.6}$$

where W is the width of the shape, and H is the height of the shape. A square has an aspect ratio of unity, while a horizontally elongated rectangle has an aspect ratio greater than one. By comparing aspect ratios of bead shapes at different parameter settings,

conclusions can be drawn regarding the effects of parameter settings on FFF. Beads with a large aspect ratio are less desirable because they do not lend well to surface finish, while aspect ratios tending toward one can create higher quality surface finishes [19]. Better FFF surface finish is achieved when a layer is able to better approximate the geometry of the part. Figure 4.10 shows plots for aspect ratio at the parameter settings identified in Figure 4.7 for each polymer, with each data point taken as the average value across three cross section samples from the same bead.

Amphora^{TM}. There is a correlation between platform speed and aspect ratio, as aspect ratio consistently decreased as platform speed increased over all parameter values studied. This is likely a result from the nozzle depositing more polymer in a smaller section at lower speeds, causing the cross sections to expand horizontally.

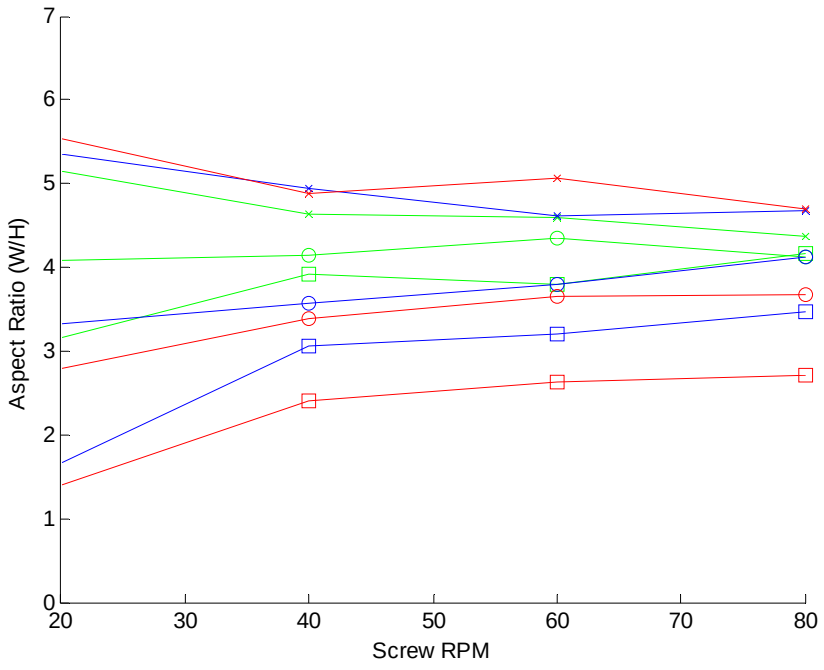

(a)

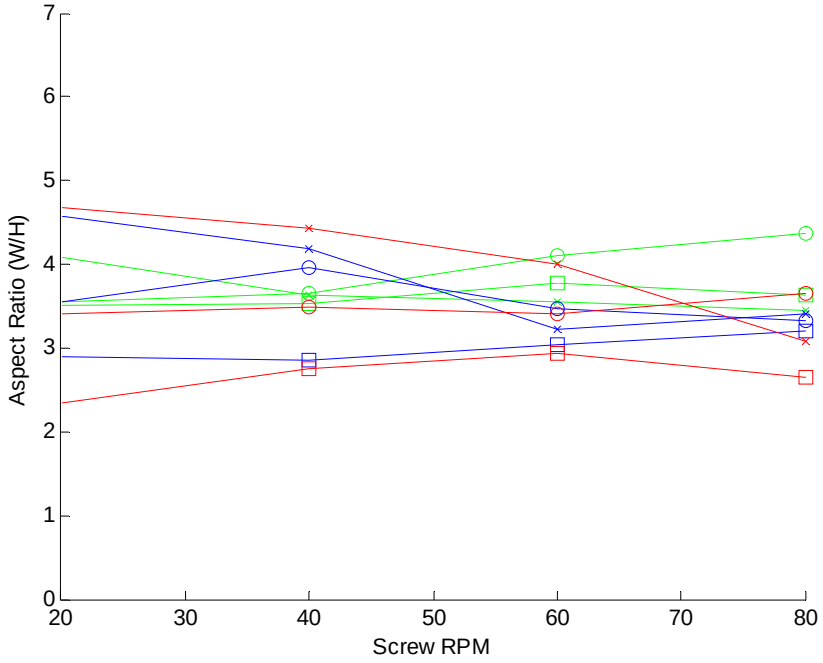
Aspect Ratio (W/H)
Screw RPM
0
1
2
3
4
5
6
7
20
30
40
50
60
70
80

(b)

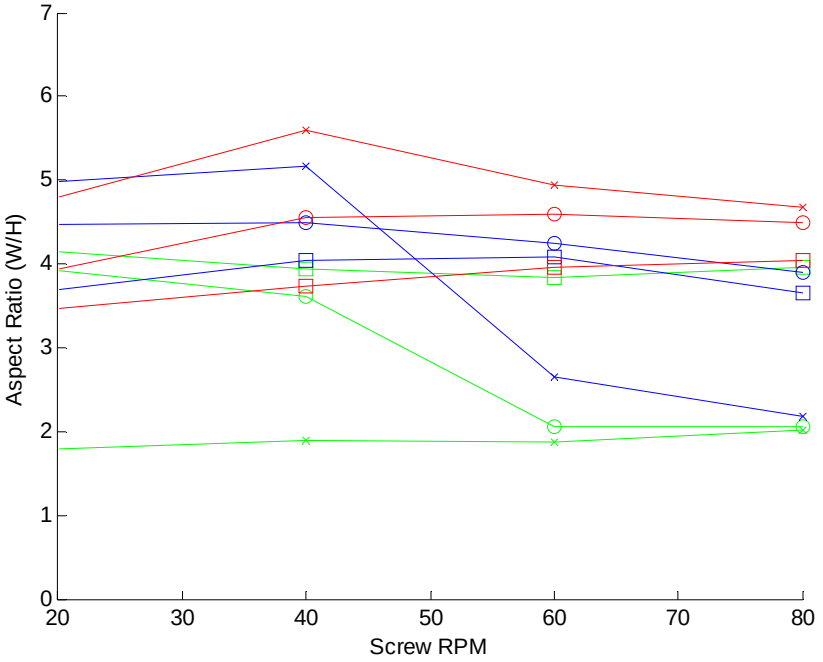
Aspect Ratio (W/H)
Screw RPM
0
1
2
3
4
5
6
7
20
30
40
50
60
70
80

(c)

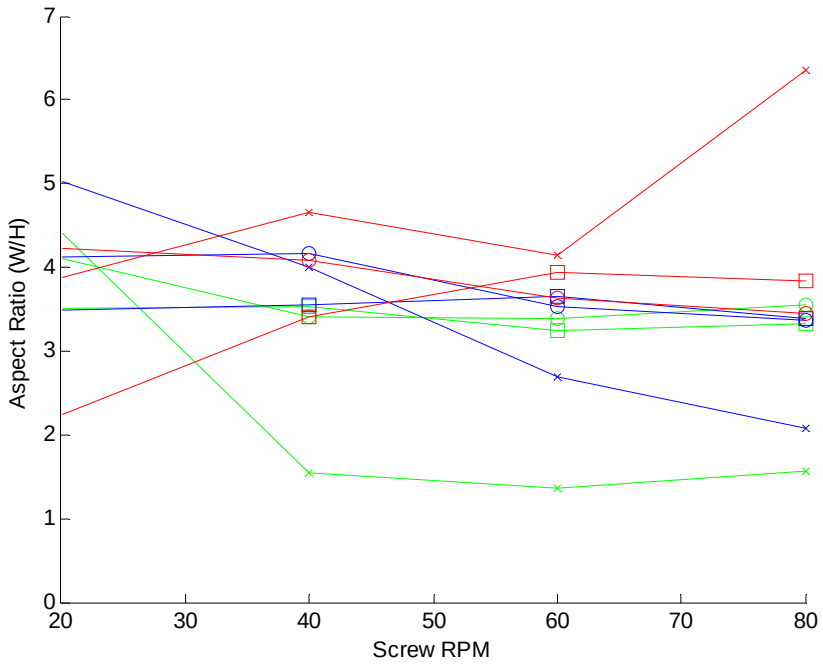

(d)

Figure 4.10. RPM vs aspect ratio for (a) Amphora™, (b) Neat ABS, (c) 10% CF ABS, and (d) 13% CF ABS.

Other trends are more difficult to identify because nozzle height and RPM do not show an obvious correlation with aspect ratio. However, there does appear to be a combined correlation for RPM and nozzle height, where as nozzle height increases, aspect ratio changes from decreasing with RPM to increasing with RPM, effectively creating a wide band of aspect ratios at low RPMs, which shrinks in variation as RPM increases.

Neat ABS. Neat ABS bead aspect ratios have less variability than those made with Amphora™, and show little variation with RPM, allowing trends due to the platform velocity and nozzle height to be more easily observed. At the lowest platform velocity of 5 mm/s, aspect ratio is relatively constant between 3.5-4.5, showing little variation with RPM or nozzle height. The variation of aspect ratios increases with platform velocity,

with the largest platform velocity showing the most variation in aspect ratio. Nozzle height is the most difficult parameter to examine because no clear trend exists. Aspect ratio decreases with increasing nozzle height, since the bottom surface of the bead is not adjacent to the platform as nozzle height increases. However, the 1.5 mm nozzle height aspect ratios do not follow the increasing trend. Instead, the 1.5 mm nozzle height corresponds to the lowest aspect ratio for the neat ABS beads, perhaps due to an increase in back pressure that allowed for less polymer to be deposited.

10% Carbon Fiber Filled ABS. It is important to note that aspect ratio is somewhat ill-defined for carbon fiber ABS since the bead shapes curve at some parameter settings and are very irregular, yielding aspect ratios that are not indicative of the actual shape of the bead. The lowest aspect ratios for the 10% carbon fiber filled ABS beads have the most irregular bead shapes; beads printed at a nozzle height of 1.5 mm have a high degree of curvature at the edges, yielding low aspect ratios for irregular shapes. Bead shapes for the Amphora™ and neat ABS were irregular at the 1.5 mm nozzle height, which is also true for the 10% carbon fiber filled ABS beads if consideration is given to warping as well as aspect ratio. Aside from the beads that show significant curvature, aspect ratio has a tendency to slightly increase with RPM, and decrease with nozzle height, similar to the Amphora™ and neat ABS polymers.

13% Carbon Fiber Filled ABS. As in the 10% carbon fiber samples, the carbon fiber inclusions tend to cause the beads to curve inward during the deposition process, rendering aspect ratio inconclusive for parameter settings where curvature is evident. Aside from curved cross sections, aspect ratio shows little variation due to any one

parameter. There is a slight decrease in aspect ratio with increasing nozzle height, which is difficult to interpret against the curved cross section ratios. Aspect ratio shows no observable relationship with RPM. Aspect ratio shows wider variation with increasing platform speed, not taking into account the bead aspect ratios at the 1.5 mm nozzle height and 5 mm/s platform velocity, which results in the most curvature during deposition.

Aspect Ratio Measured Error. Using the same method as in Section 4.1.3, measured error in aspect ratio is compared to determine the accuracy of measurements. Figure 4.11 shows error bars of $\pm\sigma$ for the Amphora™ polymer.

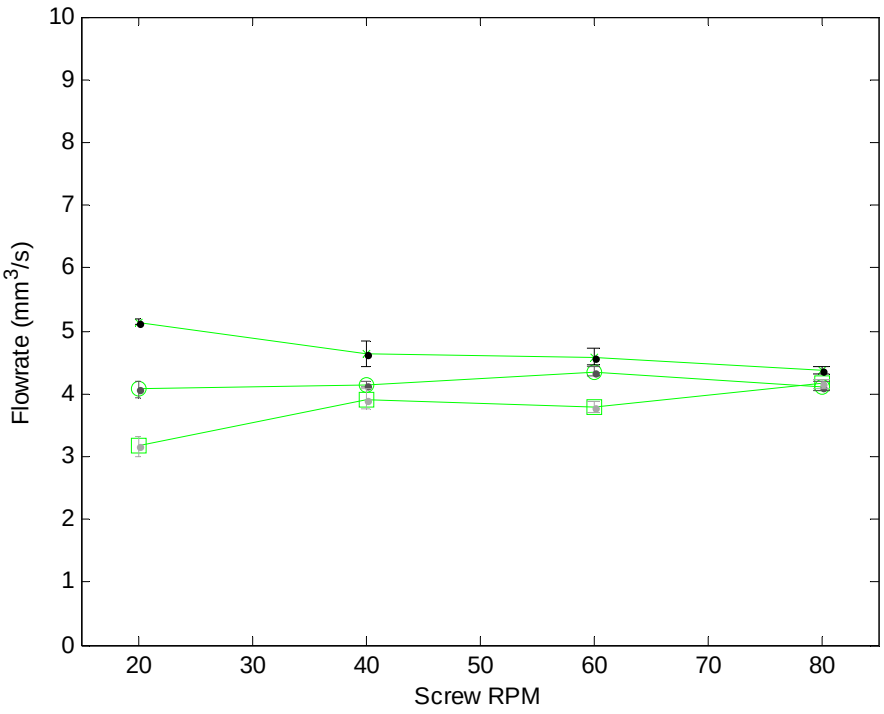

(a)

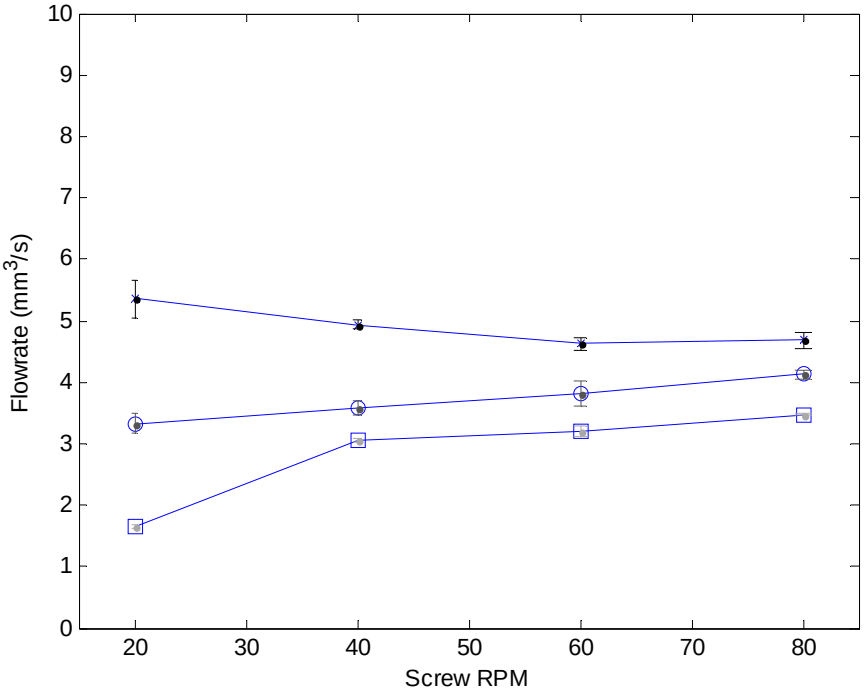

(b)

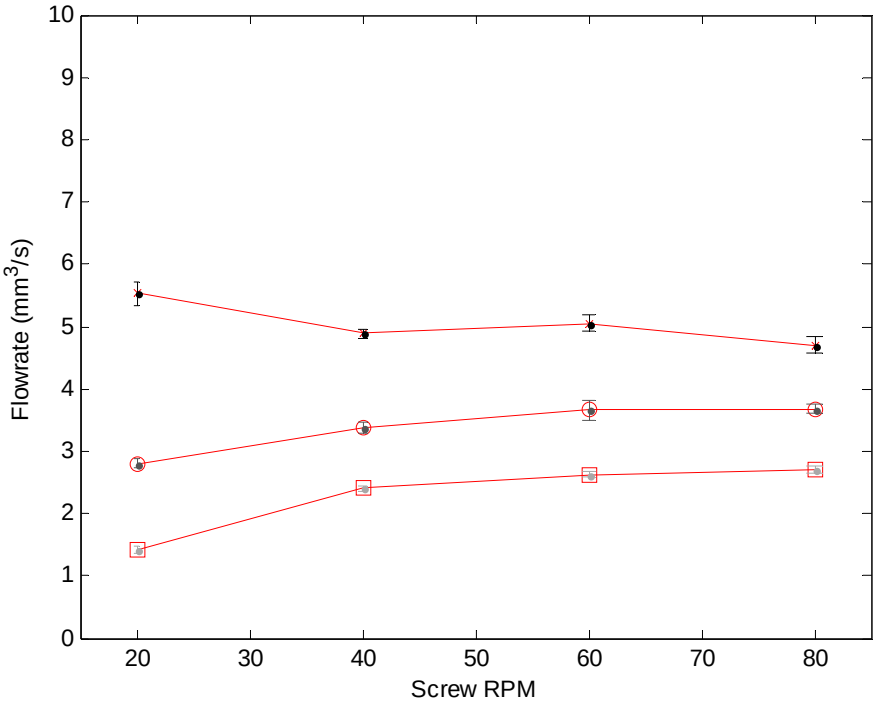

(c)

Figure 4.11. Amphora™ aspect ratio data with error bars for (a) 1.5, (b) 3.25, and (c) 5 mm nozzle heights.

Results from Figure 4.11 show that the error in the data for aspect ratio is minimal. To better quantify measurement variation, the coefficient of variation given in equation (4.5) for aspect ratio in Table 4.5.

Table 4.5. Aspect Ratio Coefficient of Variation Values for Amphora™.

Platform Velocity	Nozzle Height	RPM			
-	-	20	40	60	80
	1.5 mm	0.80	4.41	2.97	1.49
5 mm/s	3.25 mm	3.31	1.11	1.48	1.85
	5 mm	5.39	4.14	2.14	1.66
	1.5 mm	5.71	1.36	2.19	2.78
10 mm/s	3.25 mm	4.69	3.29	5.26	1.88
	5 mm	1.61	0.81	2.89	0.16
	1.5 mm	3.34	1.66	2.43	2.56
15 mm/s	3.25 mm	2.96	2.72	4.54	1.96
	5 mm	4.34	1.83	1.53	1.94

Results from Table 4.5 show that the coefficient of variation data for Amphora™ is significantly smaller than the error values produced for flowrate in Section 4.1.3. For comparison, error data is also analyzed for the Neat ABS to obtain a better understanding of the measurement error between polymers for aspect ratio. An analysis of the Neat ABS measurement error with $\pm\sigma$ error bars are shown in Figure 4.12.

Table 4.6 shows coefficient of variation for the Neat ABS aspect ratio data. Several of the values for the Neat ABS in Table 4.6 are slightly higher than the values for the Amphora™ in Table 4.5, indicating that the pulsing has little effect on the measurement accuracy of the Amphora™ data. Coefficient of variation values for the Neat ABS are mostly below 5%, with all values below 10%, showing that the aspect ratio data provides physical meaning to the system.

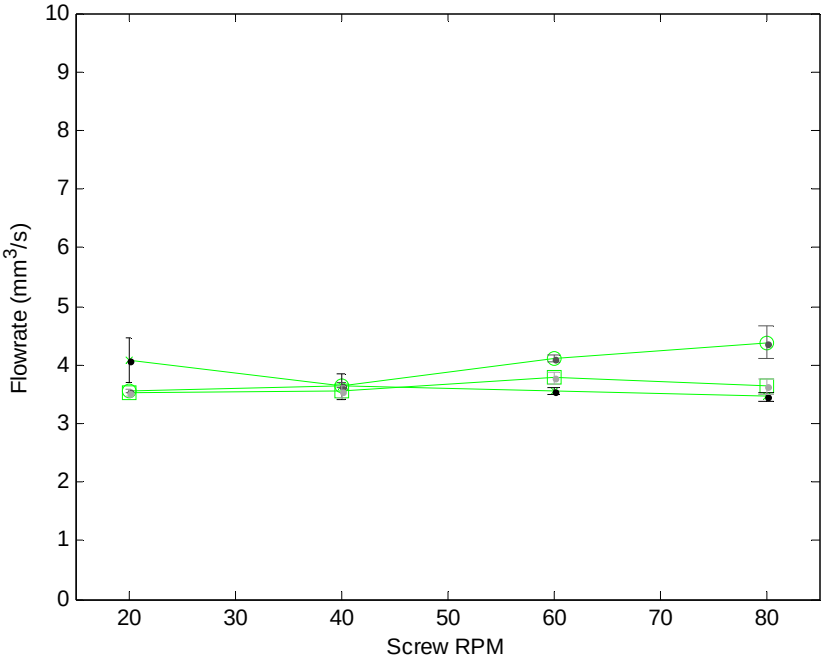
Flowrate (mm3/s)
Screw RPM
0
1
2
3
4
5
6
7
8
9
10
20
30
40
50
60
70
80

(a)

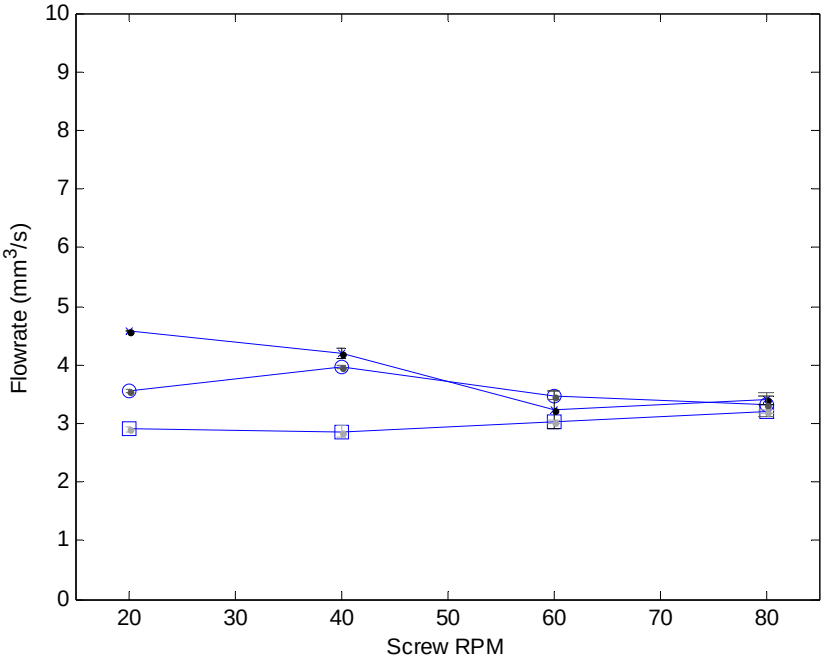
Flowrate (mm3/s)
Screw RPM
0
1
2
3
4
5
6
7
8
9
10
20
30
40
50
60
70
80

(b)

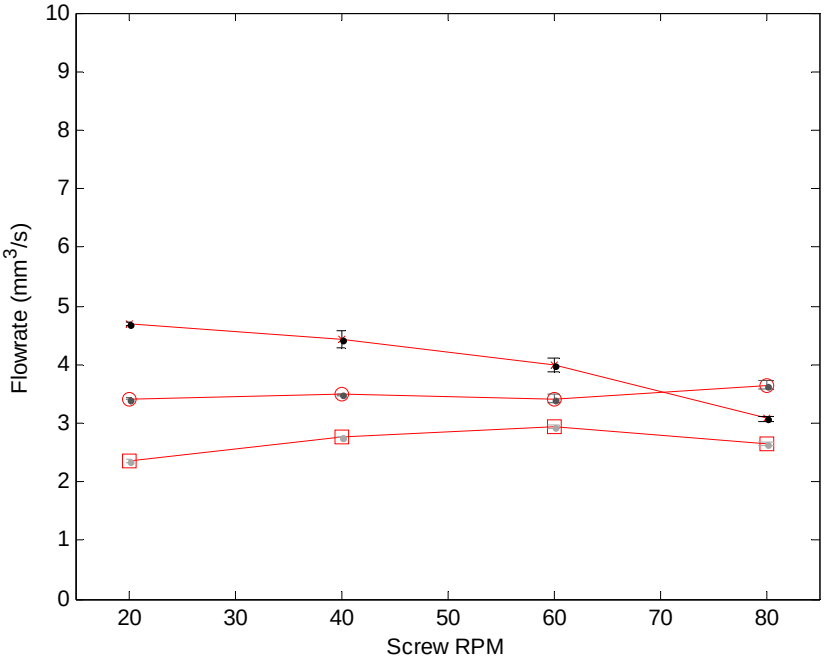

(c)

Figure 4.12. Neat ABS aspect ratio data with error bars for (a) 1.5, (b) 3.25, and (c) 5 mm nozzle heights.

Table 4.6. Aspect Ratio Coefficient of Variation Values for Neat ABS.

Platform Velocity	Nozzle Height	RPM			
-	-	20	40	60	80
	1.5 mm	9.59	6.14	1.61	2.15
5 mm/s	3.25 mm	0.48	1.26	1.65	6.47
	5 mm	1.91	2.77	2.68	3.76
	1.5 mm	0.08	2.07	9.99	2.14
10 mm/s	3.25 mm	0.90	0.87	2.04	6.01
	5 mm	1.09	3.52	1.18	1.27
	1.5 mm	0.59	3.27	2.84	1.43
15 mm/s	3.25 mm	0.46	0.23	2.13	1.95
	5 mm	1.37	0.33	1.33	1.22

4.2.2 Swell Ratios

A parameter related to aspect ratio are the swell ratios, comparisons of the final bead shape with the nozzle exit geometry. We define horizontal swell ratio as the fraction

of the bead width to the nozzle width, while vertical swell ratio is defined as the fraction of bead height to nozzle height. The calculation equation for horizontal swell ratio is:

$$S_h = \frac{W_b}{D_n} \tag{4.7}$$

where S_h is horizontal swell ratio, W_b is the width of the deposited bead, and D_n is the diameter of the extrusion nozzle. The calculation for vertical swell ratio is:

$$S_v = \frac{H_b}{H_n} \tag{4.8}$$

where S_v is vertical swell ratio, H_b is the height of the deposited bead, and H_n is the height of the extrusion nozzle from the platform.

Horizontal swell affects the potential surface finish capability of a printed part, while vertical swell affects the ability of the system to maintain printing intra-layer and during the course of an entire print over all layers. For example, if a bead vertically swells to twice the height of the nozzle once it has been deposited, the deposited bead height is then taller than the extrusion nozzle, and the bead can be impacted by the nozzle if the bead is crossed by the nozzle again before incrementing to the next layer. Similarly, after a new layer is started the vertical axis must increment at least the height of the vertical swell to maintain dimensional stability and avoid compounding error. Figure 4.13 shows plots of horizontal and vertical swell ratios.

Amphora™. The trends for horizontal and vertical swell are much easier to distinguish than those of aspect ratio for two reasons. First, swell ratios are independently measured against the height of the nozzle or width of the nozzle diameter, instead of divided into a single ratio, making them easier to individually interpret. There is a clear increasing trend for both horizontal and vertical swell ratio with RPM, caused by more

polymer being extruded from the screw, which increases the area of the cross section, and thus increases the dimensions of the cross section in both directions. There is also a clear trend of decreasing swell with increasing platform velocity across both vertical and horizontal swell, once again caused by the resultant volumetric output of polymer in a cross section from increasing platform speed. Finally, both swell ratios decrease with increasing nozzle height, indicating that the polymer can fill a more regular cross section at higher nozzle heights than at lower nozzle heights. Additionally, while horizontal swell ratio is dependent on a consistent value of nozzle diameter, nozzle height allows for a different comparison because the nozzle height changes with deposition parameters. Therefore, the FFF system has a degree of freedom to decrease vertical swell ratio with height.

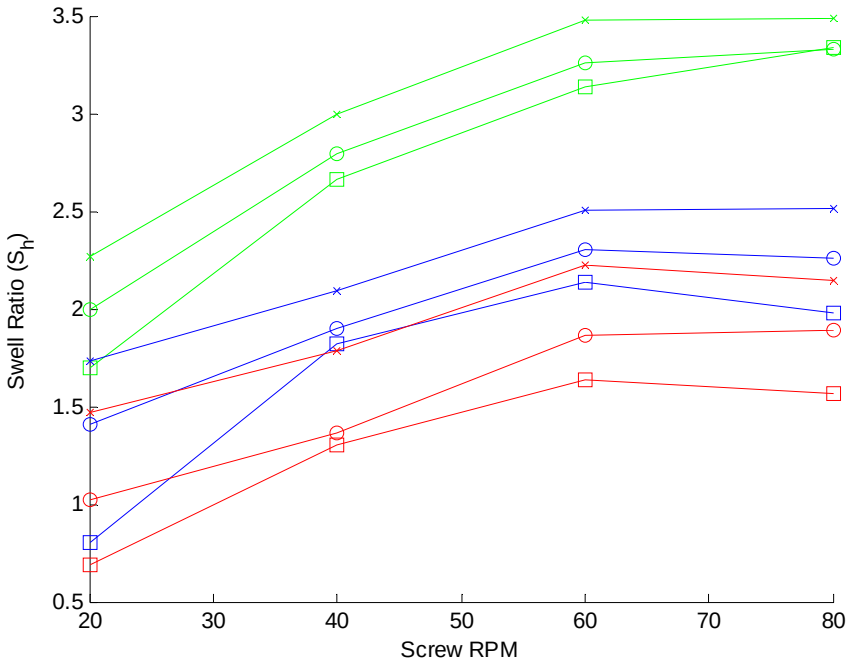

(a)

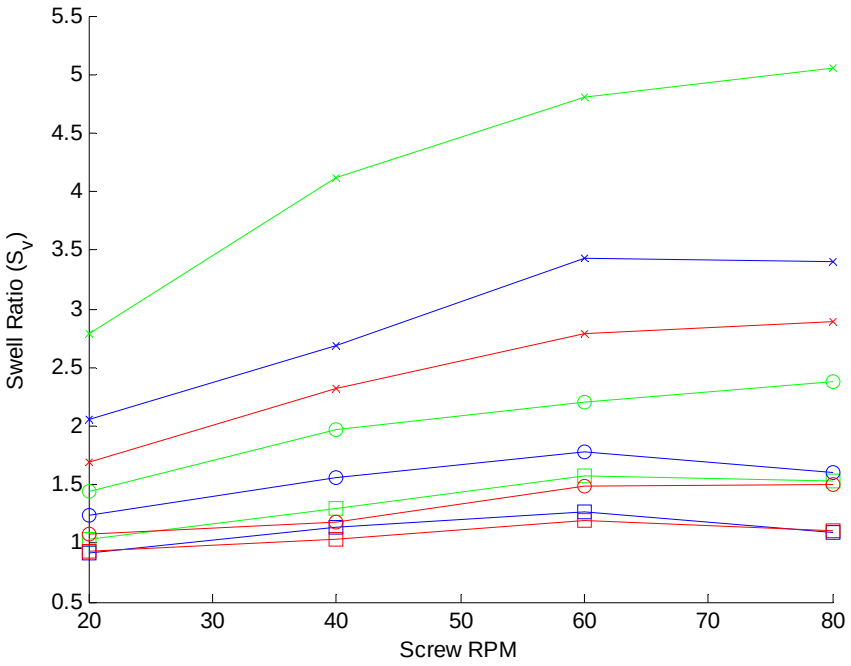
Swell Ratio (S_v)
Screw RPM
5.5
5
4.5
4
3.5
3
2.5
2
1.5
1
0.5
20
30
40
50
60
70
80

(b)

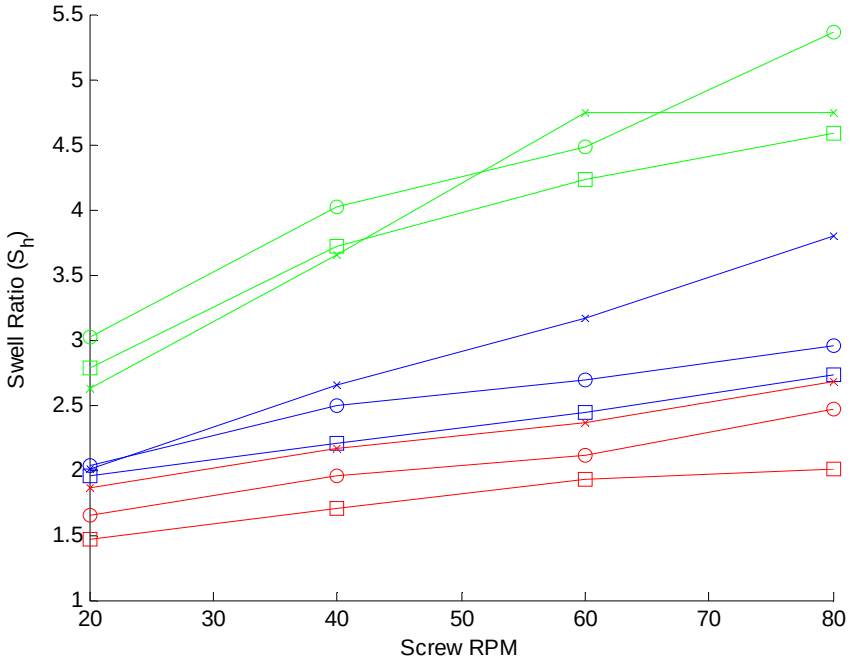
Swell Ratio (S_h)
Screw RPM
5.5
5
4.5
4
3.5
3
2.5
2
1.5
1
20
30
40
50
60
70
80

(c)

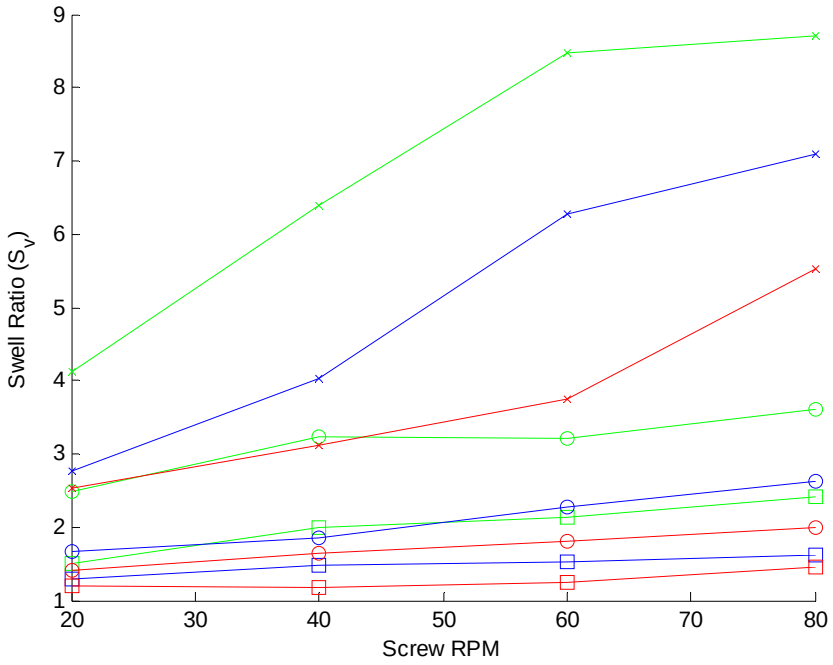
Swell Ratio (S_v)
Screw RPM
9
8
7
6
5
4
3
2
1
20
30
40
50
60
70
80

(d)

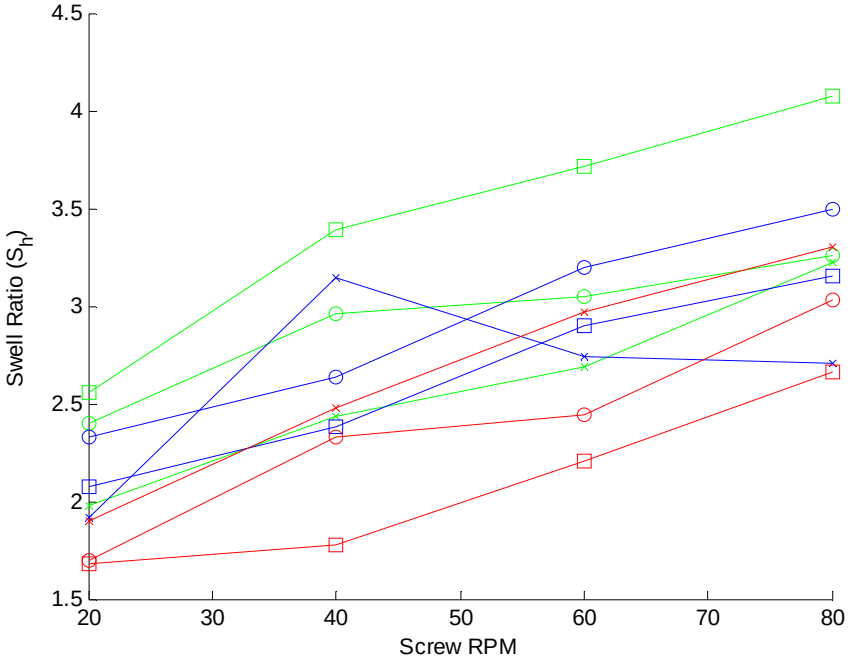
Swell Ratio (S_h)
Screw RPM
4.5
4
3.5
3
2.5
2
1.5
20
30
40
50
60
70
80

(e)

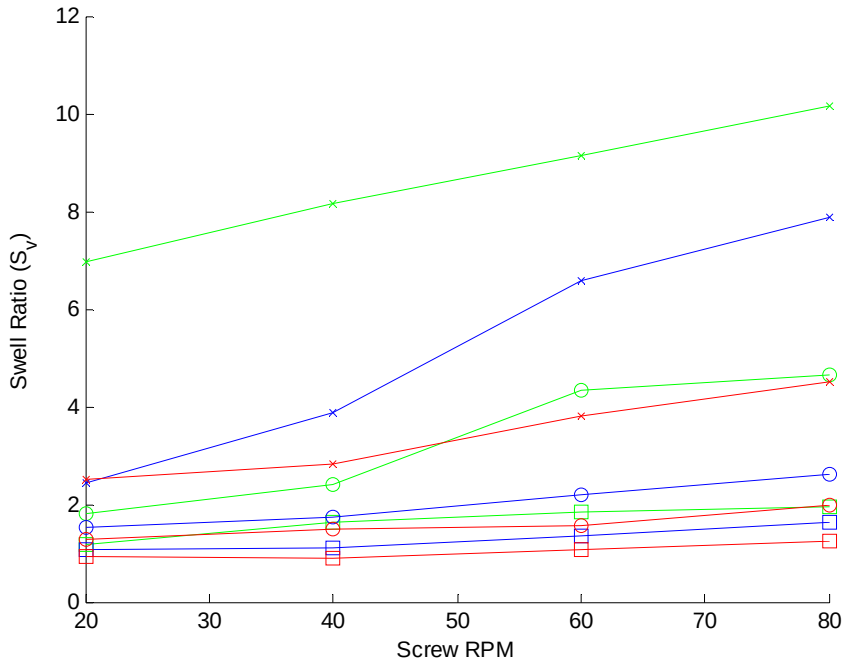
Swell Ratio (S_v)
Screw RPM
0
2
4
6
8
10
12
20
30
40
50
60
70
80

(f)

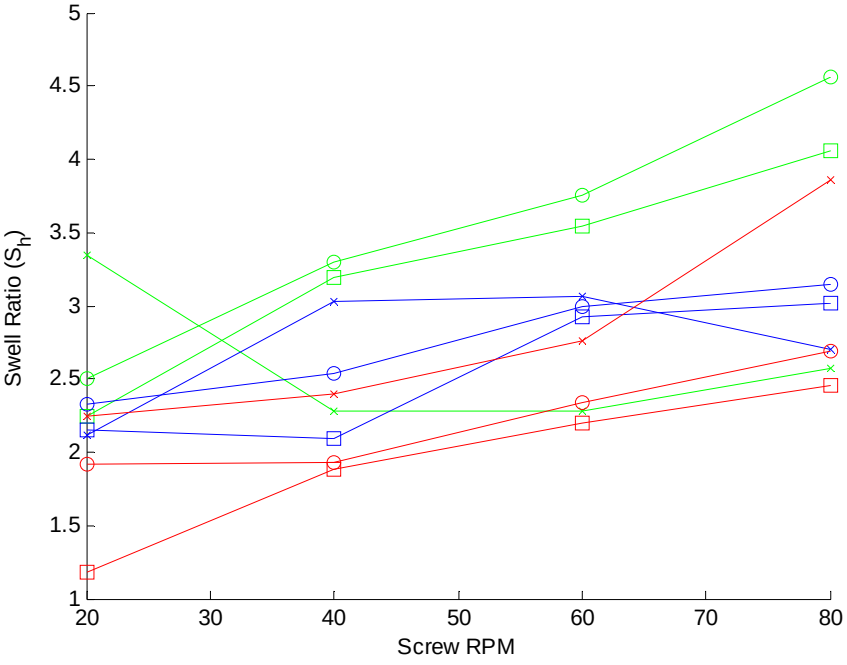
Swell Ratio (S_h)
Screw RPM
1
1.5
2
2.5
3
3.5
4
4.5
5
20
30
40
50
60
70
80

(g)

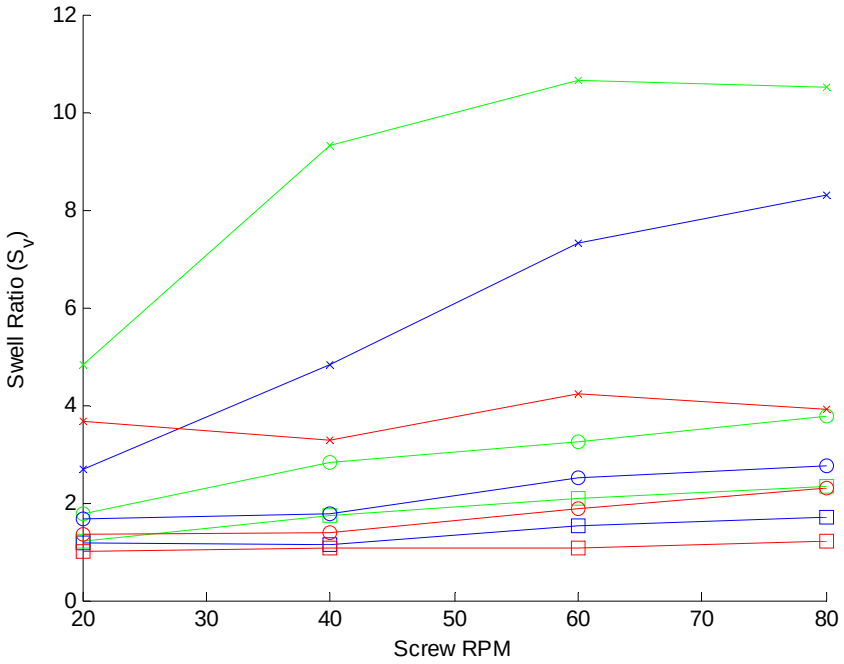

(h)

Figure 4.13. Horizontal and vertical swell ratios for (a-b) Amphora™, (c-d) Neat ABS, (e-f) 10% CF ABS, and (g-h) 13% CF ABS.

Neat ABS. A clear trend appears to exist where increasing RPM causes an increase in both swell ratios. The horizontal swell data shows better agreement with RPM than the vertical swell data, with more clearly defined trends, while the vertical data are less well defined. As with the Amphora™, the Neat ABS shows decreased swell ratios with increased platform velocity and increased nozzle height. It is important to note that the Neat ABS swells significantly more than Amphora™ at comparable settings, with both horizontal and vertical ratios nearly double those of Amphora™. Increased swell ratios suggests that the ABS swells more than the Amphora™, except that the ABS flowrates are significantly higher than the Amphora™. However, given that ABS has a high coefficient of thermal expansion of approximately 10% [12], increased ABS swelling is expected.

10% carbon fiber filled ABS. Due to the curvature of the carbon fiber filled cross sections, swell ratios are somewhat inconclusive, similar to aspect ratio. However, some trends are more obvious since horizontal and vertical effects are separated. Swell tends to increase with RPM, even with the curved cross sections, indicating that increasing swell with RPM is a significant trend, robust to transient bead effects such as curvature because the trend appears even when the bead shapes are highly irregular. Swell ratios are also grouped by platform speed, with the lowest platform speeds having the highest swell ratios, and swell ratios decreasing as platform speed increases. Swell ratios also decrease with increasing nozzle height, as the cross sections have more space to occupy between the nozzle and the platform before exceeding unity. The 1.5 mm nozzle height, 10 mm/s platform velocity swell ratio curve is of particular interest as it goes against these general trends, instead increasing up to 40 RPM and then decreasing with increasing RPM. Observing the 10% carbon fiber cross sections in Figure 4.5, 40 RPM is the point at which the beads begin to curve upward instead of lying flat against the platform at higher RPMs.

13% carbon fiber filled ABS. The 13% carbon fiber swell ratio data show less obvious trends with parameter settings than those that were seen for the previous three polymers. Swell ratios still have a tendency to increase with RPM, except for the lowest nozzle height parameter settings. Swell ratios are mostly grouped by platform speed, with greatest ratio values at the lowest platform velocity, decreasing with in value and variation with increasing platform velocity. Finally, the swell ratios decrease with increasing nozzle height at the two higher nozzle height settings, while swell ratios become irregular at the lowest nozzle height. Vertical swell at the lowest nozzle height

approaches a factor of twelve for a nozzle height of 1.5 mm, which is due in part to the curvature of the cross sections, indicating indirectly that these parameter settings are less than ideal for deposition.

Swell ratio measurement error. It is important to quantify the error in the measurements of swell ratio calculated in this section. Figure 4.14 shows plots of the Amphora^{TM} vertical and horizontal swell data with $\pm\sigma$ error bars included. To quantify the information in Figure 4.14, coefficient of variation from equation (4.5) to identify the ratio of measurement error to the spread of the data.

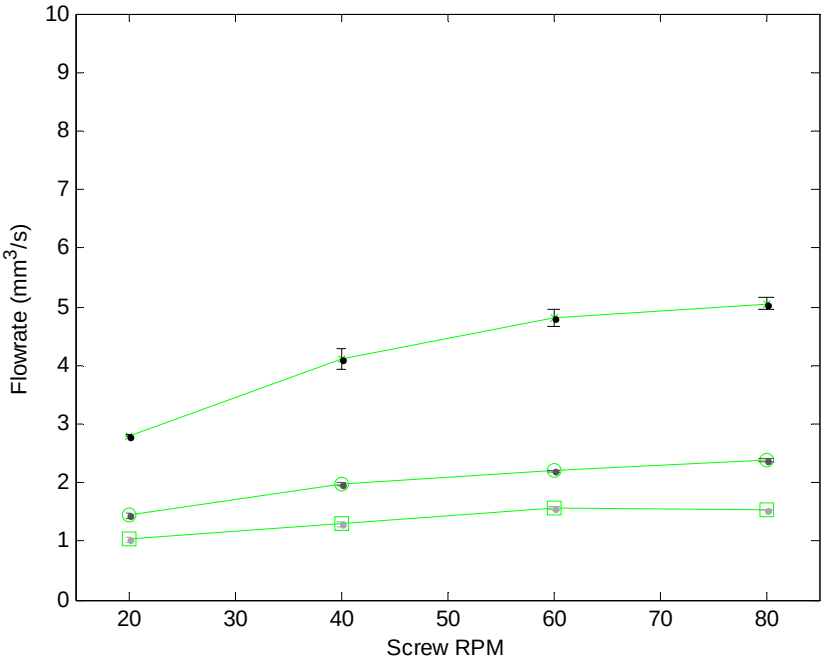

(a)

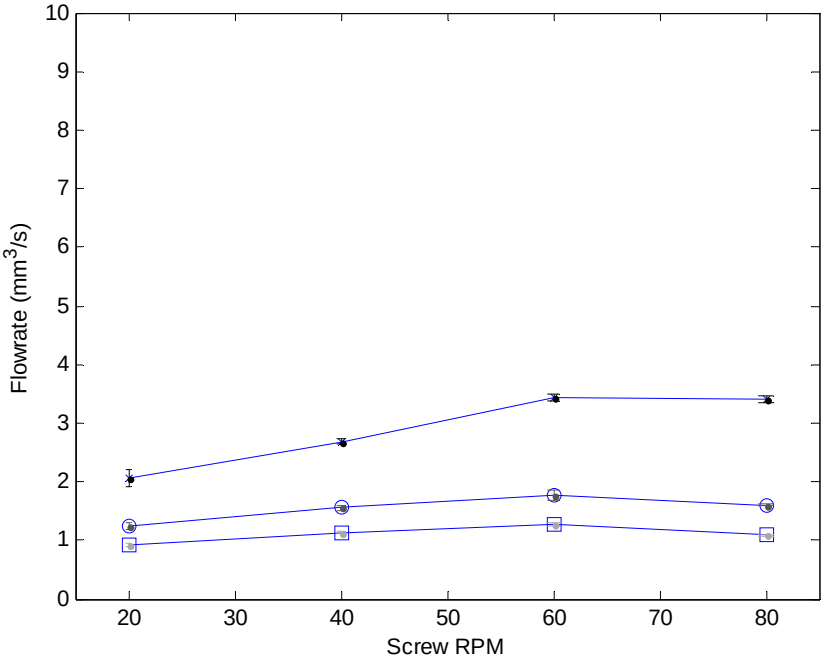
Flowrate (mm3/s)
Screw RPM
0
1
2
3
4
5
6
7
8
9
10
20
30
40
50
60
70
80

(b)

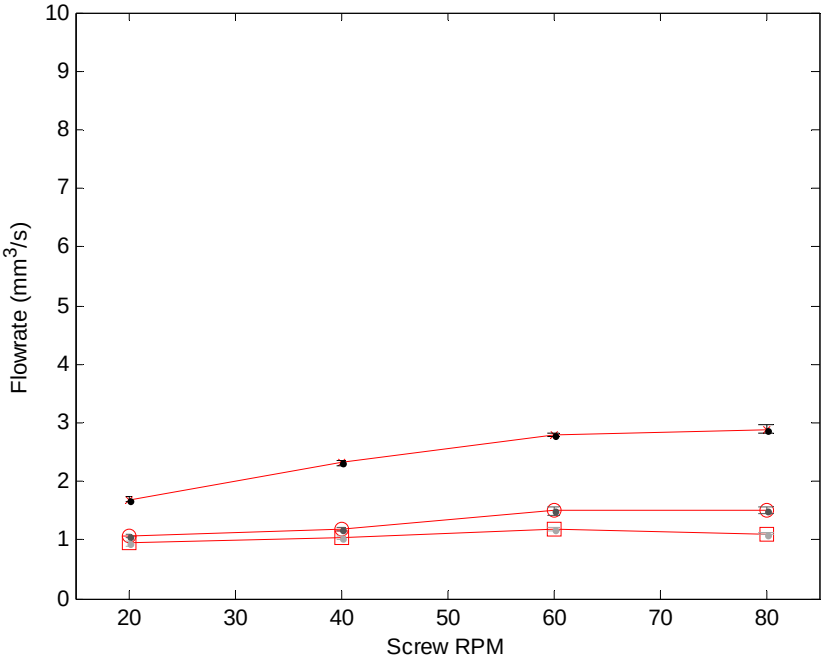
Flowrate (mm3/s)
Screw RPM
0
1
2
3
4
5
6
7
8
9
10
20
30
40
50
60
70
80

(c)

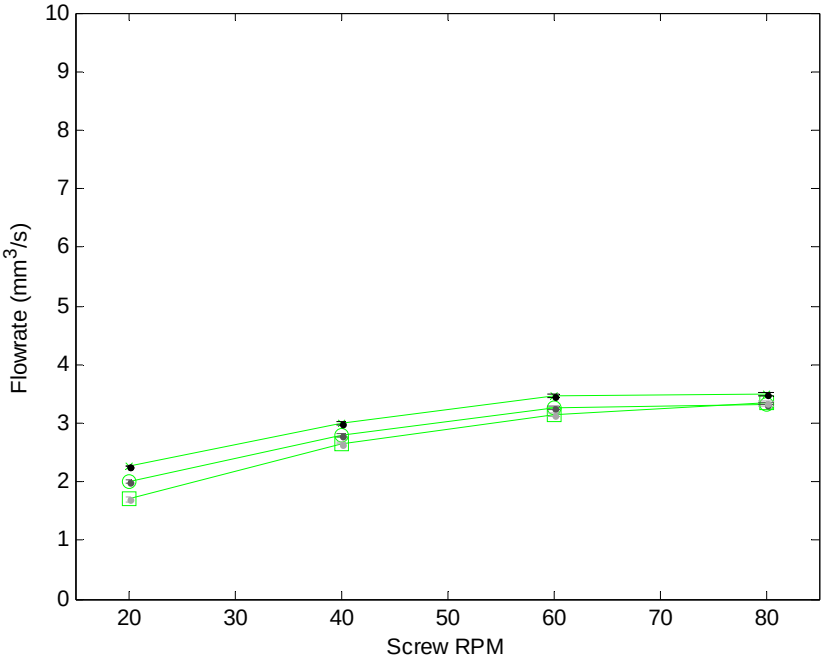
Flowrate (mm3/s)
Screw RPM
0
1
2
3
4
5
6
7
8
9
10
20
30
40
50
60
70
80

(d)

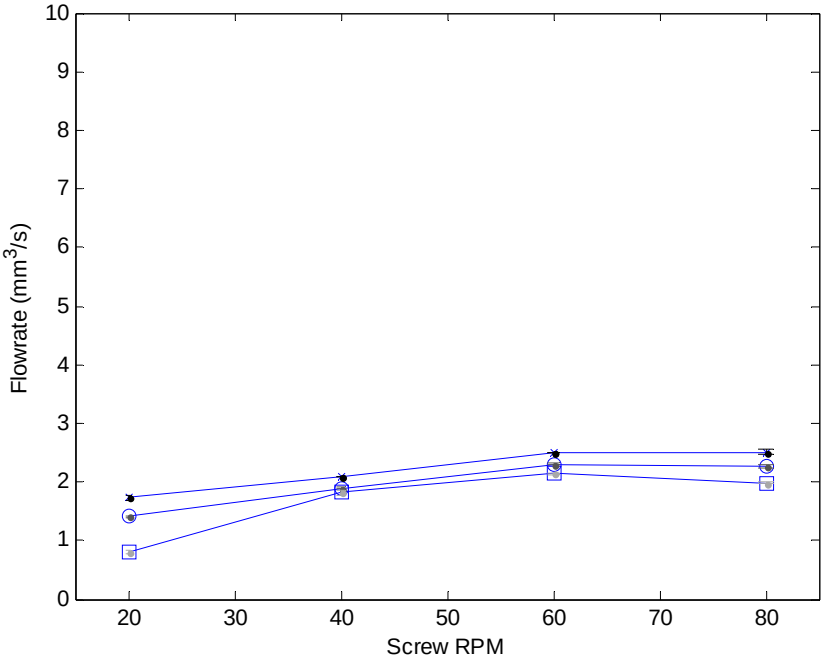
Flowrate (mm3/s)
Screw RPM
0
1
2
3
4
5
6
7
8
9
10
20
30
40
50
60
70
80

(e)

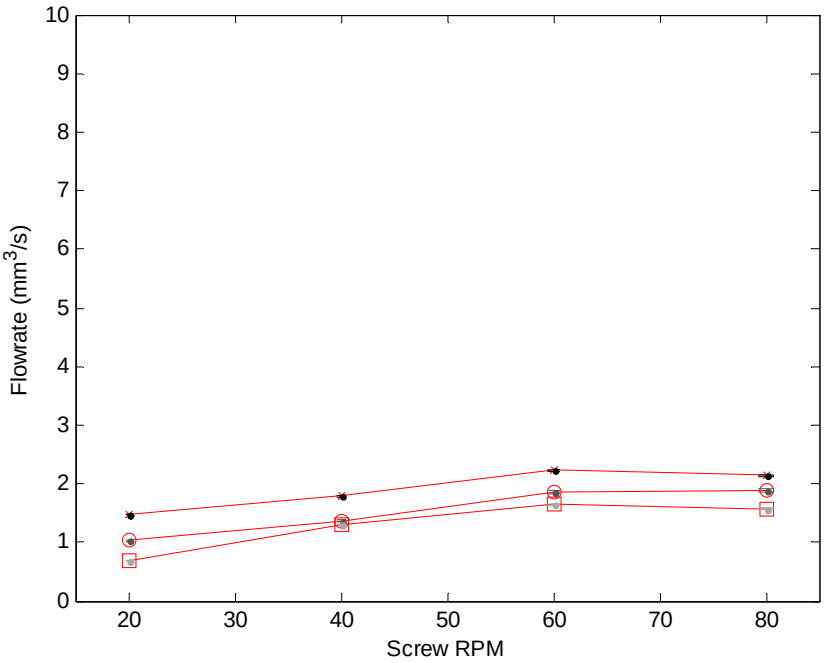

(f)

Figure 4.14. Amphora™ swell data for vertical swell at (a) 1.5, (b) 3.25, (c) 5 mm, and horizontal swell at (d) 1.5, (e) 3.25, and (f) 5 mm nozzle heights.

Table 4.7. Amphora™ vertical swell % coefficient of variation values.

Platform Velocity	Nozzle Height	RPM			
-	-	20	40	60	80
	1.5 mm	0.55	4.11	3.10	1.82
5 mm/s	3.25 mm	3.13	2.14	0.60	1.26
	5 mm	3.69	3.38	1.90	0.50
	1.5 mm	6.73	1.27	1.71	1.96
10 mm/s	3.25 mm	4.68	3.03	4.77	1.32
	5 mm	4.27	1.60	2.47	0.72
	1.5 mm	3.11	2.00	1.51	2.11
15 mm/s	3.25 mm	2.97	2.81	4.74	2.95
	5 mm	4.98	2.09	1.94	1.01

Table 4.8. Amphora™ horizontal swell % coefficient of variation values.

Platform Velocity	Nozzle Height	RPM			
-	-	20	40	60	80
	1.5 mm	0.26	0.66	0.79	0.73
5 mm/s	3.25 mm	1.05	1.14	1.06	0.75
	5 mm	2.22	0.88	0.71	1.17
	1.5 mm	2.59	0.28	0.52	1.33
10 mm/s	3.25 mm	0.77	0.67	0.63	1.04
	5 mm	2.85	2.38	0.71	0.85
	1.5 mm	0.38	1.20	1.24	0.66
15 mm/s	3.25 mm	0.41	0.94	1.48	1.82
	5 mm	0.76	0.91	0.58	1.08

The coefficient of variation data shown in Table 4.7 and

Table 4.8 indicate that the data has little associated error, with values in the tables below 5%. A comparison can be done with the Neat ABS error similar to the comparison in Section 4.2.1.

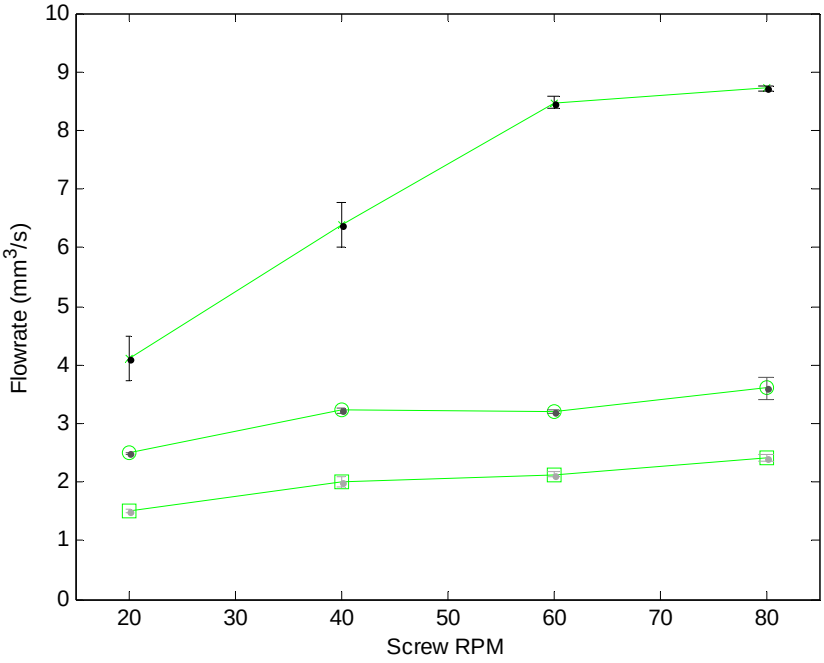
Flowrate (mm3/s)
Screw RPM
0
1
2
3
4
5
6
7
8
9
10
20
30
40
50
60
70
80

(a)

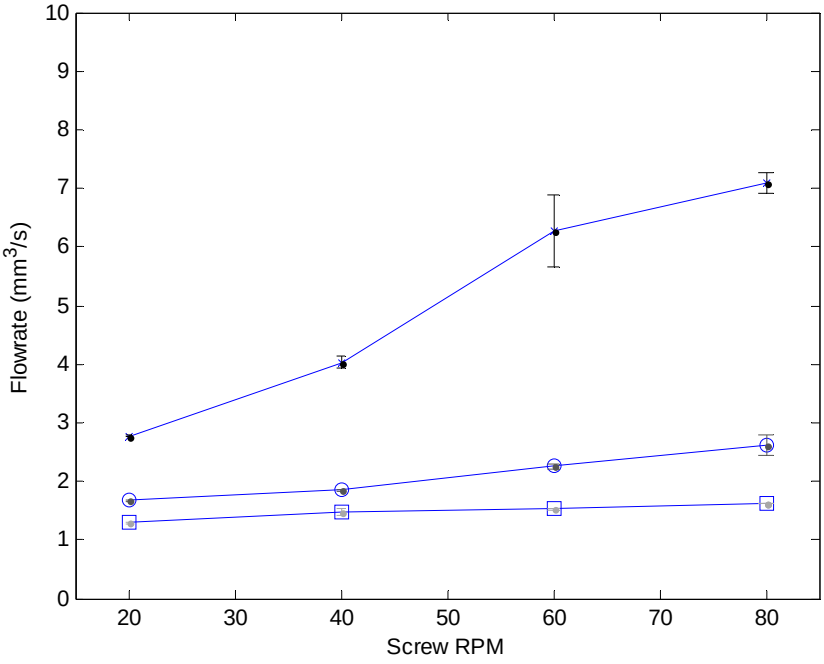
Flowrate (mm3/s)
Screw RPM
0
1
2
3
4
5
6
7
8
9
10
20
30
40
50
60
70
80

(b)

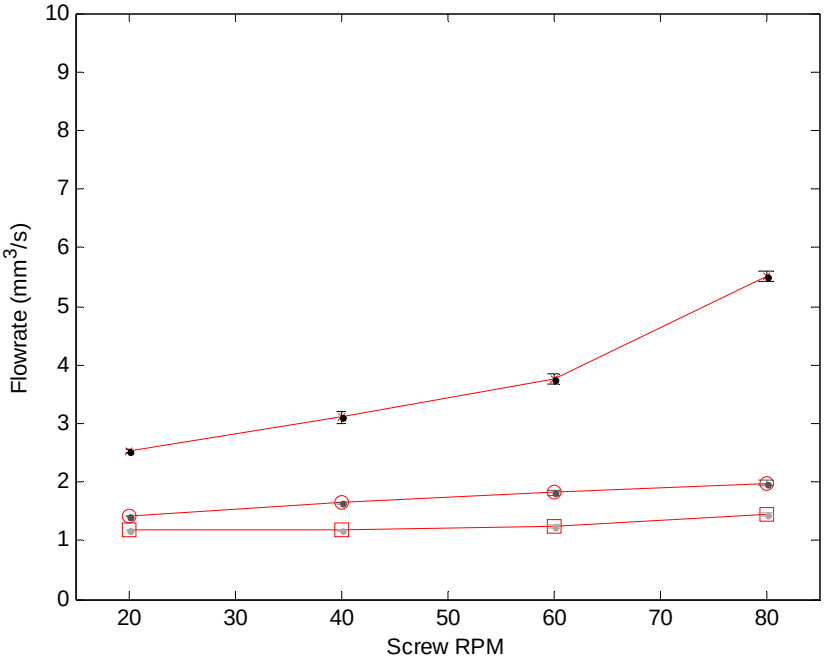
Flowrate (mm3/s)
Screw RPM
0
1
2
3
4
5
6
7
8
9
10
20
30
40
50
60
70
80

(c)

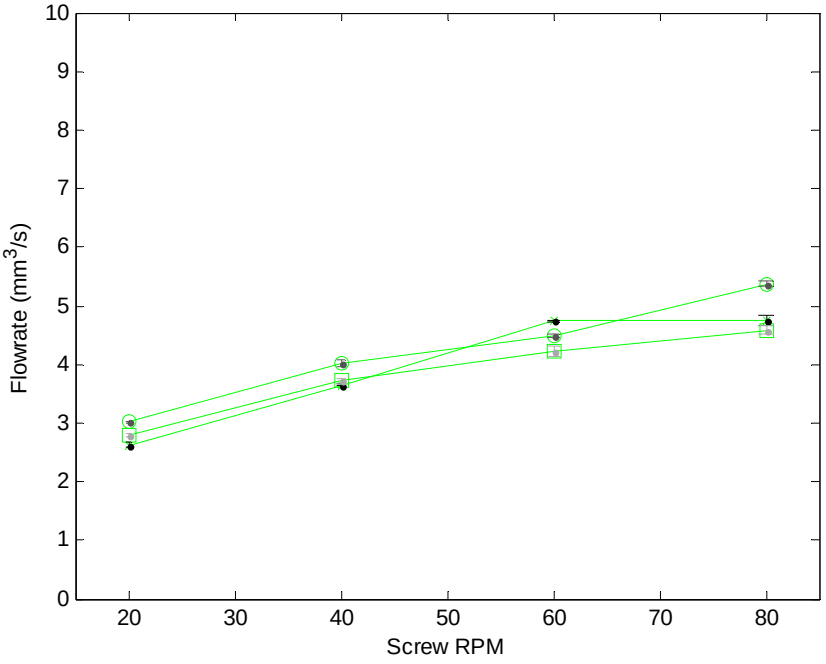
Flowrate (mm3/s)
Screw RPM
0
1
2
3
4
5
6
7
8
9
10
20
30
40
50
60
70
80

(d)

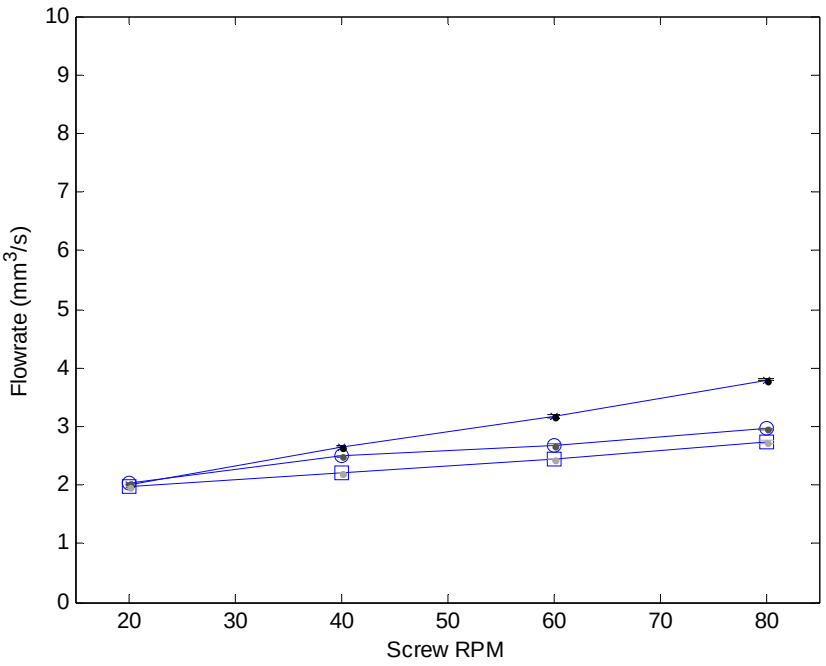

(e)

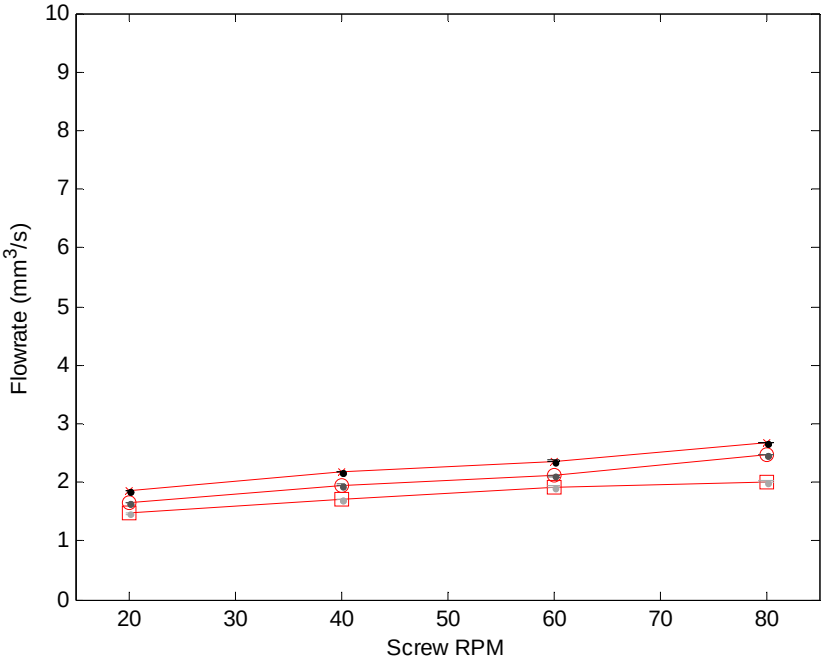

(f)

Figure 4.15. Neat ABS swell data for vertical (a) 1.5, (b) 3.25, (c) 5 mm, and horizontal (d) 1.5, (e) 3.25, and (f) 5 mm nozzle heights.

Table 4.9 and

Table 4.10 show coefficient of variation data for Neat ABS vertical and horizontal swell data, which can be compared to Amphora™ values in Table 4.7 and

Table 4.8.

Table 4.9. Neat ABS vertical swell % coefficient of variation values.

Platform Velocity	Nozzle Height	RPM			
-	-	20	40	60	80
	1.5 mm	9.25	5.82	1.16	0.45
5 mm/s	3.25 mm	0.45	1.34	0.88	5.55
	5 mm	1.54	4.01	1.54	1.98
	1.5 mm	0.50	2.57	9.95	2.52
10 mm/s	3.25 mm	1.17	0.99	1.89	6.27
	5 mm	1.20	3.46	0.92	0.84
	1.5 mm	1.10	3.42	2.69	1.47
15 mm/s	3.25 mm	0.79	0.52	1.81	1.85
	5 mm	0.58	0.54	1.82	1.76

Table 4.10. Neat ABS horizontal swell % coefficient of variation values.

Platform Velocity	Nozzle Height	RPM			
-	-	20	40	60	80
	1.5 mm	1.39	0.47	0.48	1.90
5 mm/s	3.25 mm	0.48	1.28	0.86	0.80
	5 mm	0.96	1.23	2.24	1.79
	1.5 mm	0.43	0.64	0.96	0.38
10 mm/s	3.25 mm	0.27	0.37	0.14	0.51
	5 mm	0.38	0.22	0.33	0.84
	1.5 mm	0.53	0.16	0.40	0.10
15 mm/s	3.25 mm	0.60	0.34	0.30	0.26
	5 mm	1.00	0.32	0.62	0.62

Knowledge of data error is especially important when examining data such as that shown in, where data lines cross each other on the plot; is the physical system actually

crossing at parameter settings, or is the crossing an effect of error? A few of the coefficient of variation values for the Neat ABS are slightly high, but these values are still less than 10% of the scale of the data. Therefore, the error associated with swell ratios is insignificant compared to the scale of the data, allowing the data to be interpreted as indicative of the deposition process with little effect of error on outcomes.

4.2.3 Bead Shape Convexity

In previous sections, geometry factors have been used to identify bead shapes which are better suited to deposition, with an emphasis on degrees of suitability to FFF. This section introduces a measure of convexity to identify parameter settings which are expected to perform better in the FFF process. Specific attention is given to bead shapes which have high degrees of irregularity in shape, such as the carbon fiber cross sections that curve, or parts that shrink away from the build plate. Convexity is defined as the ability to draw a straight line from any point along the boundary of a polygon to any other point along its boundary, without exiting the polygon along the path of the line [65]. A convexity ratio is defined from bead cross-sectional area A_b and minimal convex outline A_c that completely encloses the cross section:

$$C_n = \frac{A_b}{A_c} \tag{4.9}$$

where C_n is bead shape convexity. An example of bead shape versus smallest convex bead shape is shown in Figure 4.17. The convexity metric should clearly identify cross sections which are highly irregular in shape, since features such as plate lift-off, rough surfaces, and top surface concavity result in a large difference between the original and convex geometries. Convexity ratios are shown for each polymer over all parameter values studied in Figure 4.17.

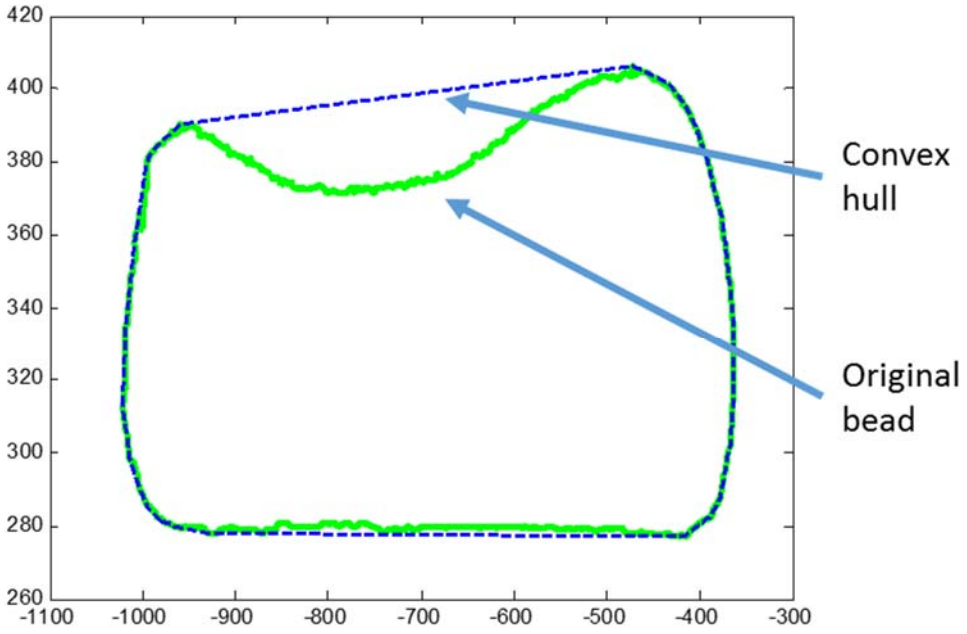

Figure 4.16. Sample bead cross section overlaid with convex hull.

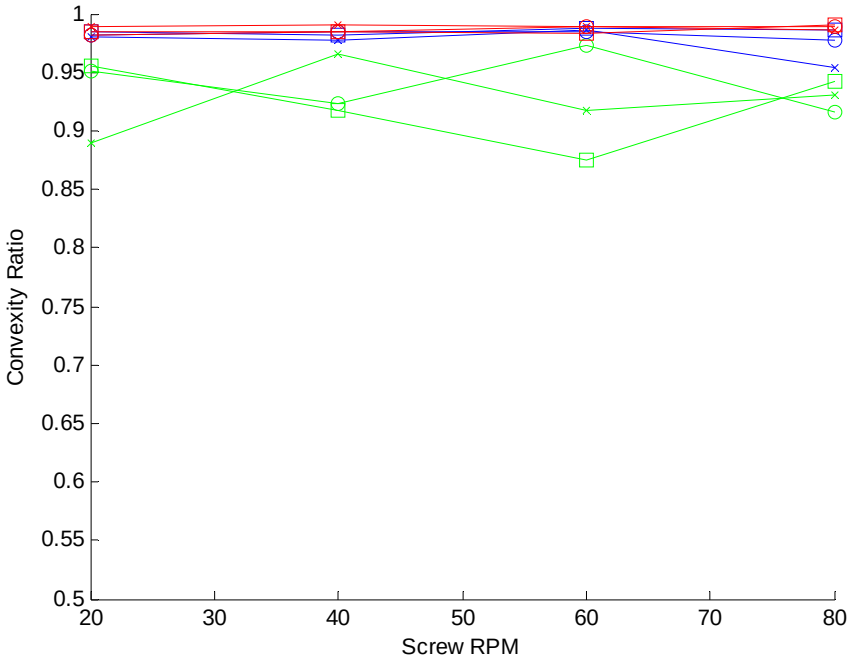

(a)

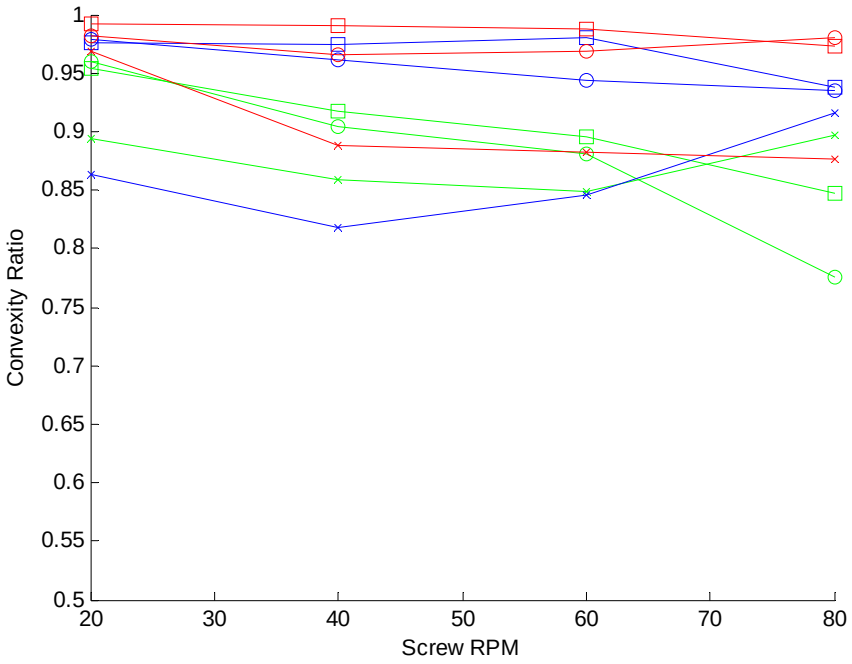
Convexity Ratio
Screw RPM
1
0.95
0.9
0.85
0.8
0.75
0.7
0.65
0.6
0.55
0.5
20
30
40
50
60
70
80

(b)

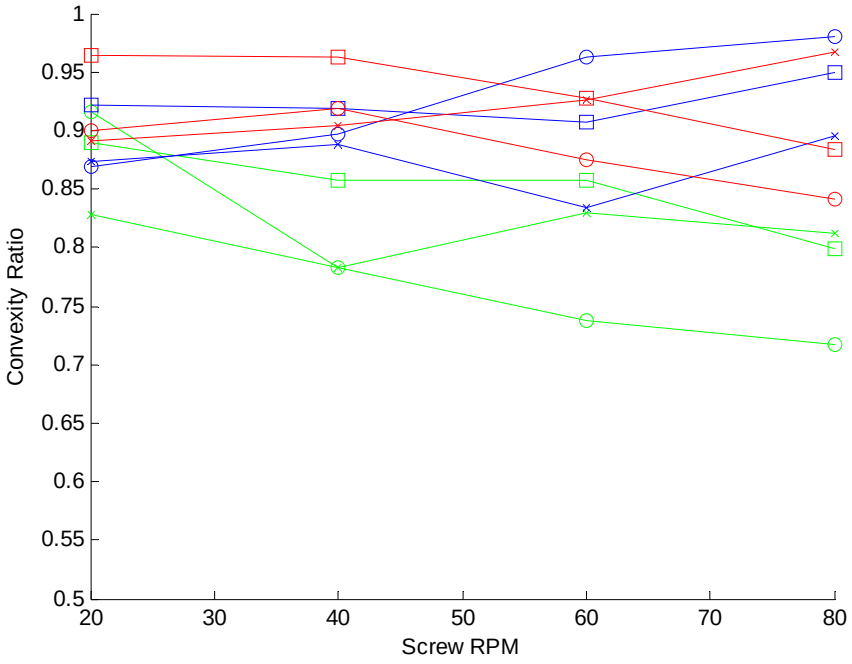
Convexity Ratio
Screw RPM
1
0.95
0.9
0.85
0.8
0.75
0.7
0.65
0.6
0.55
0.5
20
30
40
50
60
70
80

(c)

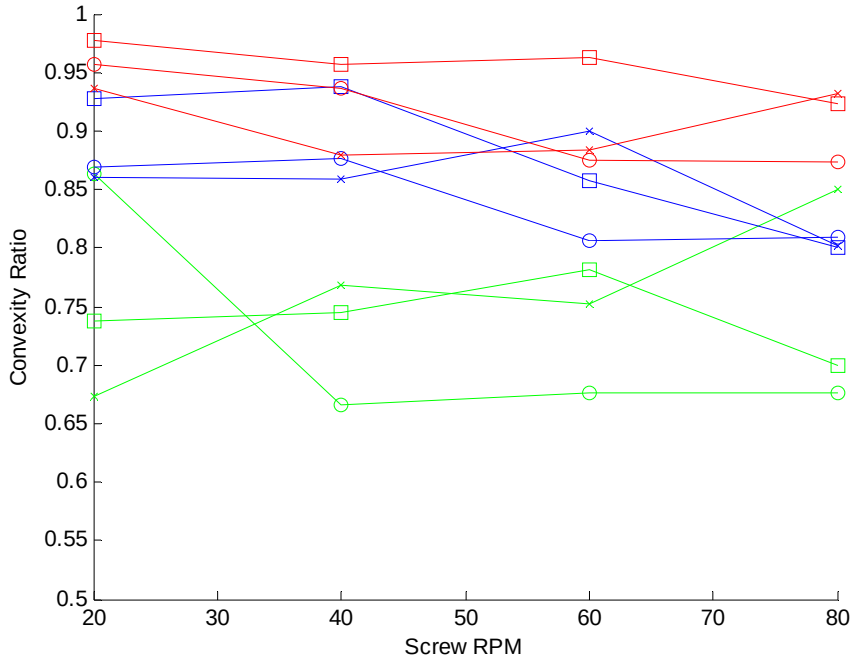

(d)

Figure 4.17. Convexity ratios for (a) Amphora™, (b) Neat ABS, (c) 10% CF ABS, and (d) 13% CF ABS over all parameter values studied.

Amphora™. Examination of the convexity of the Amphora™ cross sections shows that 94% of the convexity ratios are greater than 0.9, indicating that the cross sections are almost completely convex with few irregular features. Upon visually comparing convexity values above 0.9 with the cross sections from Figure 4.3. the bead shapes are very similar in shape, with little plate lift-off on the bottom, and little to no concavity on top. Figure 4.17 shows that the cross sections at the slowest platform velocity of 5 mm/s have the highest degree of irregularity due to concave curvature of the top surface of the beads. Noting that these bead shapes appear to be suitable from a convexity perspective, a threshold value of 0.9 will be used to compare the other polymer cross sections.

Neat ABS. Only 61% of the convexity ratios for neat ABS are acceptable by the 0.9 threshold previously established. Lower values of convexity occur for two parameter settings, those at the lowest nozzle height (1.5 mm) and the lowest platform velocity (5 mm/s). In comparison with the cross sections in Figure 4.4, cross sections at 1.5 mm and 5 mm/s possess the widest range of irregularities, from plate lift-off at the bottom to rough surface features, all of which add to the disparity between convex area and cross sectional area. Operation with parameter settings at 1.5 mm nozzle height and 5 mm/s platform velocity produce beads that do not meet the 0.9 threshold and should be avoided. It is also important to observe that the best bead shapes by the convexity ratio metric occur at the higher platform velocities, namely 10 mm/s and 15 mm/s.

10% carbon fiber filled ABS. By visual observation of the cross sections in Figure 4.5, a majority of the geometries exhibit some degree of irregular shape, most notable in the side curvature at the lowest nozzle height (1.5 mm) and lowest platform velocity (5 mm/s). Only 39% of the 10% carbon fiber filled ABS bead geometries have convexity ratios greater than 0.9. Figure 4.17 further illustrates that most convexity ratios for the two lowest platform velocities (5 mm/s and 10 mm/s) are below the 0.9 threshold, which quantifies the irregular cross sections appearing in Figure 4.5. Parameter settings at the highest table velocity (15 mm/s) and the two higher nozzle heights (3.25 mm and 5 mm) produce more acceptable values of convexity ratio, providing beads that are better suited for FFF.

13% carbon fiber filled ABS. The 13% carbon fiber cross sections display the broadest variation of data on the convexity plot, with values at the lowest velocity (5

mm/s) having a convexity ratio as low as 0.65. With only 28% of the 13% carbon fiber filled ABS beads having a convexity ratio greater than 0.9, the 13% carbon fiber beads performed the worst of the four polymers tested with the lowest number of acceptable parameter settings. Most parameter settings at the highest platform velocity (15 mm/s), and several from the midrange platform velocity setting (10 mm/s), are acceptable deposition parameters, suggesting that the highest velocity setting produces the best beads with respect to convexity for both carbon fiber filled polymers.

Convexity ratio measurement error. The convexity shape metric is based on the cross sectional area of the bead, which is also used to calculate flowrates in Section 4.1.1. Therefore, the error associated with the convexity data is the same as the error associated with the flowrate data and will not be addressed further here.

4.2.4 Shape Compactness

This section identifies ranges of bead parameters for each polymer that exhibit the highest degree of shape compactness. A shape compactness ratio is defined by selecting a specific geometric shape, and then comparing the shape of a bead cross section to a reference shape. Here the smallest geometry of the reference shape which can circumscribe the entire bead cross section is selected and the compactness ratio is defined by comparing the area of the bead to the area of the circumscribing shape [66]. Compactness is similar to convexity in that a circumscribing shape is used for area comparison, but in the case of compactness, parameter settings which were selected as optimal for FFF using the convexity ratio metric can then be evaluated using the compactness metric. For our shape compactness study a rectangle was chosen as the

reference shape, since a bead with a rectangular cross section is considered as ideal for FFF. The bead shape compactness ratio is calculated using the following equation (4.10):

$$C_m = \frac{A_b}{A_r} \tag{4.10}$$

where C_m is bead shape compactness ratio, A_b is the area of the deposited bead, and A_r is the area of the deposited bead's best-fit rectangle. Figure 4.18 shows the shape compactness ratios of three regular geometric shapes when using the rectangular parameter as the reference shape.

Note that beads with low values for compactness ratio will indicate cross sections that are not ideal for deposition, with potential defects such as significant curvature on the top and/or bottom of the beads, curving at the edges, and rough surface finish. Figure 4.19 shows shape compactness ratios for each of the four polymers across all deposition parameters considered in this thesis.

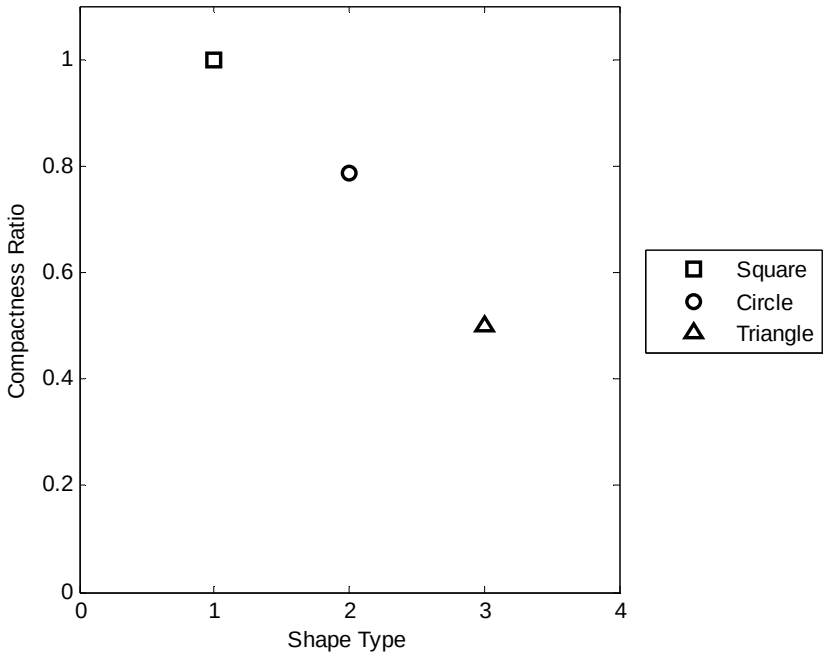

Figure 4.18. Shape compactness ratio for a square, a circle, and a triangle when using best-fit circumscribing rectangle.

Unlike the convexity parameter measured in the previous section where some cross sections approached completely convex shapes, cross sections compared using compactness will have lower overall values because a completely rectangular shape is difficult to achieve in free deposition. The FFF process is much more likely to create cross sections with curved edges. Therefore, acceptable compactness ratios can also be lower in value than convexity ratios, while keeping in mind that the purpose of comparison to a rectangular shape is to minimize the voids that would be created when using the bead shape for FFF.

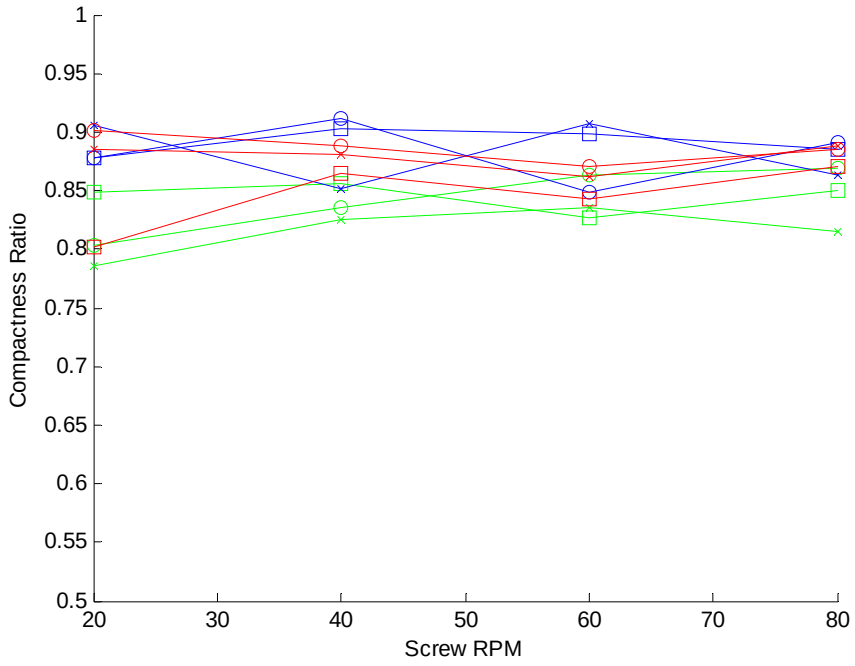

(a)

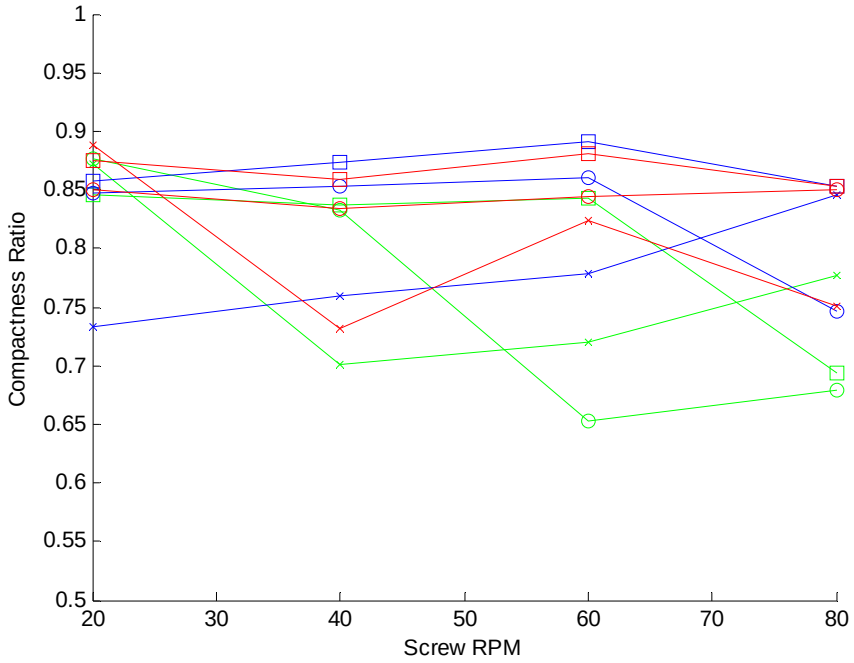
Compactness Ratio
Screw RPM
1
0.95
0.9
0.85
0.8
0.75
0.7
0.65
0.6
0.55
0.5
20
30
40
50
60
70
80

(b)

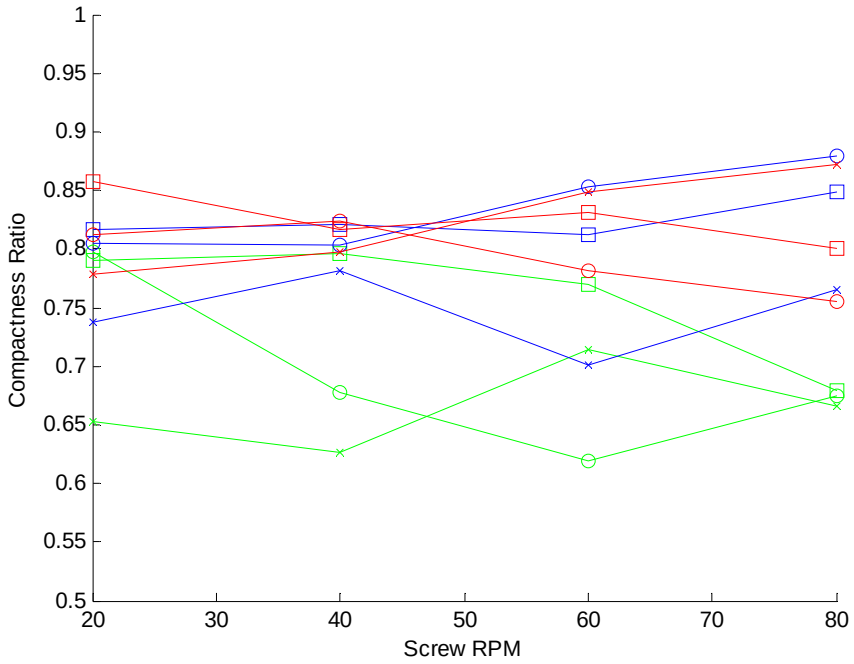
Compactness Ratio
Screw RPM
1
0.95
0.9
0.85
0.8
0.75
0.7
0.65
0.6
0.55
0.5
20
30
40
50
60
70
80

(c)

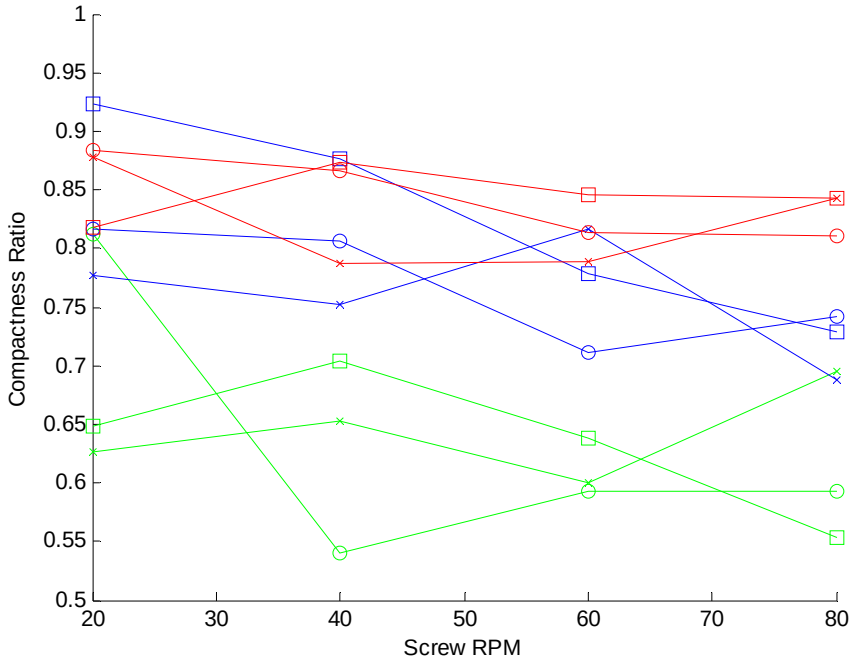

(d)

Figure 4.19. Shape compactness ratios for (a) Amphora™, (b) Neat ABS, (c) 10% CF ABS, and (d) 13% CF ABS over all parameter values studied.

Amphora™. Similar to the convexity ratios, Amphora™ cross sections have the tightest variation of compactness ratios with values at and above 0.8. Compactness ratio values appear grouped by platform velocity with the lowest platform velocity (5mm/s) having lower compactness ratios. This indicates that higher platform velocities create better beads as measured by compactness ratio. Other trends are not apparent within each group of platform velocity, suggesting that other parameters do not effect cross section rectangular shape. Therefore, all parameter settings at the higher levels of platform velocity (10mm/s and 15mm/s) are acceptable for deposition by compactness ratio.

Neat ABS. More parameters using the Neat ABS polymer fall below the 0.8 threshold than with the Amphora™ based on compactness, with parameters at the lowest platform velocity (5mm/s) and the lowest nozzle height (1.5mm) generating low compactness ratio values. Comparing ABS compactness values with the previous acceptable Amphora™ parameter values, a threshold of 0.85 is sufficient for determining parameters suitable for deposition.

10% Carbon Fiber Filled ABS. Very few of the 10% carbon fiber cross sections meet the minimum ratio value established by the Amphora™ and Neat ABS polymers. Of those parameters that are within an acceptable range, all are at the higher two platform velocities (10mm/s and 15mm/s). If the acceptable metric limit is lowered to 0.8, a majority of the higher platform velocity parameters fall into an acceptable range, which ultimately means that FFF printing with 10% carbon fiber ABS polymer will create larger voids than with Amphora™ and neat ABS.

13% Carbon Fiber Filled ABS. The 13% carbon fiber occupies the widest variation of data points, the same observation made in the convexity analysis, which follows logically because convexity and compactness are related. Using the threshold compactness ratio value of 0.85, acceptable parameter settings can be found at the higher platform velocities (10mm/s and 15mm/s), as well as the higher nozzle heights (3.25mm and 5mm). While some cross sections in the lowest platform velocity (5mm/s) demonstrate very low compactness ratio values, the 13% carbon fiber polymer performs better at specified parameter settings than the 10% carbon fiber cross sections, likely due in part to their differences in composition as outlined in Chapter Three.

Compactness Ratio Measurement Error. The compactness shape metric is based on the cross sectional area of the bead, which is the same method used to calculate flowrates in Section 4.1.1. Therefore, the error associated with the compactness data is the same as the error associated with the flowrate data.

4.3 Bead Shape Prediction Regression

Recall from Section 4.2.2 that low vertical swell ratios are desired to avoid the nozzle from impacting previously laid beads when incrementing the print in the z-direction. Additionally, the system must also deposit beads side-by-side to optimize intra-layer bonding. Therefore, it is imperative to understand the bead shape measurements as a function of deposition parameters. In this section, a model is presented which predicts bead height and width based from the deposition parameters considered in this thesis, as well as a numerical analysis of how well the model fits the empirical data.

4.3.1. Least Squares Regression Model

The numerical method of least squares regression is commonly used to fit an approximate model to the data using any combination of independent variables of any order. The process for determining the best fit coefficients requires first determining the equation and number of independent variables. For example, in the case of FFF deposition parameters in our study, bead shape is influenced by three independent parameters, each of which is assumed to linearly affect the output geometry. The equation considered here for our deposition process is:

$$y = a_0 + a_1 R + a_2 H + a_3 S \tag{4.11}$$

where y is the output bead geometry metric, a_0 is the y-intercept, a_1 is the scaling coefficient for the independent input variable RPM (R, RPM), a_2 is the scaling coefficient for the independent input variable Height (H, mm), and a_3 is the scaling coefficient for the independent input variable platform velocity (S, mm/s).

Values for the unknown coefficients are determined by using the sum of squares of the residuals S_r defined as:

$$S_r = \sum_{i=1}^{n}(y_i - a_0 - a_1R_i - a_2H_i - a_3S_i)^2 \tag{4.12}$$

S_r is the summation of the squares of each data point minus the estimation of that data point using the fitted equation [67]. The best fit coefficients are then obtained by taking partial derivatives of equation (4.12) with respect to each of the coefficients, yielding the linear set of equations:

$$\frac{\delta S_r}{\delta a_0} = -2\sum_{i=1}^{n}(y_i - a_0 - a_1R_i - a_2H_i - a_3S_i) \tag{4.13}$$

$$\frac{\delta S_r}{\delta a_1} = -2\sum_{i=1}^{n}R_i(y_i - a_0 - a_1R_i - a_2H_i - a_3S_i) \tag{4.14}$$

$$\frac{\delta S_r}{\delta a_2} = -2\sum_{i=1}^{n}H_i(y_i - a_0 - a_1R_i - a_2H_i - a_3S_i) \tag{4.15}$$

$$\frac{\delta S_r}{\delta a_3} = -2\sum_{i=1}^{n}S_i(y_i - a_0 - a_1R_i - a_2H_i - a_3S_i) \tag{4.16}$$

By setting each partial derivative equal to zero, the best fit coefficients can be calculated using methods from linear algebra. To compare the regression model to the data, the coefficient of determination method is used where we define:.

$$SS_{tot} = \sum_{i=1}^{n}(y_i - \bar{y})^2 \tag{4.17}$$

$$SS_{res} = \sum_{i=1}^{n}(y_i - f_i)^2 \tag{4.18}$$

$$R^2 = 1 - \frac{SS_{res}}{SS_{tot}} \tag{4.19}$$

In the above, SS_{tot} is the total sum of squares of the empirical data, $\bar{y}$ is the mean of the empirical data, SS_{res} is the residual data not explained by the model, f_i is the model prediction of the ith data point, and R^2 is a value between zero and one which describes the goodness of fit of the model to the experimental data; higher values of R^2 denote a better fit, while lower values of R^2 represent a worse fit.

4.3.2. Deposition Prediction Models

The least squares regression method from Section 4.3.1 is used to develop predictive shape models for horizontal and vertical bead deposition size for the four polymers used in this study. Additionally, the coefficient of determination is calculated for each regression model to determine goodness of fit.

Amphora™. The Amphora™ beads were the least sensitive to the deposition process, as described in Section 4.1.2 on general bead shape analysis. Therefore, we expect that the least squares regression for the Amphora™ will be the most accurate. Following the methods outlined in Section 4.3.1, the following bead shape models were developed for predicting the size of Amphora™ bead height and width:

$$x = 28.5 + 0.17R - 1.34H - 1.23S \tag{4.20}$$

$$y = 4.72 + 0.03R + 0.32H - 0.21S \tag{4.21}$$

where x is the horizontal bead width and y is the vertical bead height. Recall that R is in RPM, H is in mm, and S is in mm/s. The coefficient of determination for both horizontal and vertical Amphora™ bead prediction models are shown in Table 4.11.

Table 4.11. Coefficient of determination for Amphora™ models.

Model Type	R^2
Horizontal	0.889

Vertical	0.823

The coefficient of determination values for both horizontal and vertical models show good agreement with the experimental data, with both values above 0.8. The horizontal data shows very good agreement with a value at nearly 0.9, indicating that horizontal bead size can be accurately predicted using Equation 4.18.

Section 4.2.2 discussed trends of horizontal and vertical bead swell related to deposition parameters, noting that both horizontal and vertical swell increases with increasing RPM, which is supported by the prediction models where both horizontal and vertical bead shape increases with RPM. The other trends discussed in Section 4.2.2 also hold true to the prediction models, indicating that horizontal bead shape decreases with nozzle height and table speed, while vertical bead shape increases with increasing nozzle height and decreases with platform speed.

Neat ABS. The Neat ABS beads were found to be more sensitive to deposition than the Amphora™ beads, with bead shapes including irregular features that create noise in the bead shape data. Therefore, it is expected that the Neat ABS regression models will fit the data less well than the Amphora™ regression models. Least squares regression data is shown in Equations 4.20 and 4.21.

$$x = 39.2 + 0.21R - 1.07H - 1.87S \tag{4.22}$$

$$y = 8.95 + 0.06R + 0.02H - 0.44S \tag{4.23}$$

The coefficients of determination for horizontal and vertical Neat ABS prediction models are shown in Table 4.12.

Table 4.12. Coefficient of determination for Neat ABS models.

Model Type	R^2
Horizontal	0.878
Vertical	0.843

The coefficient of determination values for both horizontal and vertical models show good agreement with the experimental data, with both values above 0.8. The horizontal model fits the Neat ABS data slightly less well than the Amphora™ model, while the vertical model fits the Neat ABS data slightly better than the Amphora™ model. Relating the Neat ABS shape prediction models back to the bead shapes in Section 4.1.2, Figure 4.4, it is important to note that the regression model will predict the largest height and width features of the bead. Since the Neat ABS bead shapes in Figure 4.4 have irregular features, the predictive model is most likely influenced by these irregularities, and may over or under-predict bead dimensions based on errors introduced by irregularities.

Another important feature of the Neat ABS bead height and width models is the prediction that horizontal bead shape is positive linearly affected by RPM and negative linearly affected by nozzle height and table speed, which agrees with the conclusions from Section 4.2.2 on swell ratios. These trends are similar to the trends observed with the Amphora™ beads, indicating that the deposition process has similar effects on bead shape across polymers.

10% Carbon Fiber Filled ABS. The carbon fiber filled bead shapes were highly affected by curvature along the edges of the bead, as discussed in Section 4.1.2. While the following regression models will predict bead shape across all parameters examined in our study, the regression models for the carbon fiber beads should not be used to

deposition at parameter settings that are less than ideal for deposition. Regression models for the 10% carbon fiber filled ABS bead shapes are given in equations (4.24) and (4.25).

$$x = 21.7 + 0.18R + 0.25H - 0.57S \quad (4.24)$$

$$y = 11.1 + 0.08R - 0.56H - 0.55S \quad (4.25)$$

Coefficient of determination values for horizontal and vertical 10% carbon fiber filled ABS prediction models are shown in Table 4.13.

Table 4.13. Coefficient of determination for 10% carbon fiber filled ABS models.

Model Type	R^2
Horizontal	0.706
Vertical	0.814

The 10% carbon fiber filled ABS beads have worse agreement with their predictive models than the Amphora™ and the Neat ABS, which can be attributed to two factors. First, the carbon fiber filled beads occupy a greater range of shapes than the Amphora™ and the Neat ABS, requiring the prediction model to cover a wider variation of geometries. Another reason for the prediction models to be less accurate is because the general shape of the carbon fiber beads change as the deposition parameters, from high degrees of edge curvature and lower aspect ratios to little edge curvature and larger aspect ratios. Therefore, it is difficult for the model to accurately predict the drastic change in shape of the beads, making the model a less accurate prediction of shape.

13% Carbon Fiber Filled ABS. The 13% carbon fiber filled ABS beads were affected by the same curvature as the 10% carbon fiber filled ABS beads, causing a shape change from deposition parameters with high degrees of curvature to parameters with little to no curvature. Therefore, similar results are expected for the 13% carbon fiber

shape prediction models as the results from the 10% carbon fiber filled prediction models.

$$x = 26.8 + 0.16R - 0.39H - 0.77S \quad (4.26)$$

$$y = 11.1 + 0.08R - 0.58H - 0.51S \quad (4.27)$$

Coefficient of determination values for horizontal and vertical 13% carbon fiber filled ABS prediction models are shown in Table 4.14.

Table 4.14. Coefficient of determination for 13% carbon fiber filled ABS models.

Model Type	R^2
Horizontal	0.545
Vertical	0.775

Unlike the 10% carbon fiber filled ABS beads, the 13% carbon fiber filled ABS beads follow the same sign trends for horizontal shape prediction as those for the Amphora™ and Neat ABS, with bead size increasing with RPM and decreasing with nozzle height and platform velocity. However, the coefficient value for nozzle height contribution is significantly smaller than those for the Amphora™ and Neat ABS beads, indicating that the linear relationship of horizontal bead shape to nozzle height is not as strong. The vertical bead shape regression for the 13% carbon fiber filled ABS beads is nearly identical to the regression for the 13% carbon fiber filled ABS beads, giving a strong indication of similar behavior of the carbon fiber polymers in the deposition process.

4.3.3. Regression Summary

The regression prediction method defined in Section 4.3.1 and Section 4.3.2 can be applied to all output variables examined in our study. This section provides an

overview of the regression equation for each of these output variables, as defined in (4.11), where the a_0 term is the y-intercept term, a_1 is the RPM coefficient, a_2 is the nozzle height coefficient, and a_3 is the platform velocity coefficient. In the following, the input RPM is in RPM, nozzle height is in mm, and platform velocity is in mm/s. Regression coefficients and R^2 values for all output variables are summarized in the following tables:

Table 4.15. Regression Coefficients for Flowrate in mm^3/s

Material	A_0	A_1	A_2	A_3	R^2
Amphora	184.54	11.64	0.87	7.09	0.825
Neat ABS	721.71	20.42	-32.21	-13.03	0.879
CF-10	15.76	21.10	-11.15	30.86	0.884
CF-13	145.10	18.29	8.37	25.93	0.868

Table 4.16. Regression Coefficients for Bead Width in mm

Material	A_0	A_1	A_2	A_3	R^2
Amphora	28.5	0.17	-1.34	1.23	0.889
Neat ABS	39.2	0.21	-1.07	-1.87	0.878
CF-10	21.7	0.18	0.25	-0.57	0.706
CF-13	26.8	0.16	-0.39	-0.77	0.545

Table 4.17. Regression Coefficients for Bead Height in mm

Material	A_0	A_1	A_2	A_3	R^2
Amphora	4.72	3.30E-2	0.32	-0.21	0.823
Neat ABS	8.95	6.23E-2	2.40E-2	-0.44	0.843
CF-10	11.1	7.59E-2	-0.56	-0.55	0.814
CF-13	11.1	7.51E-2	-0.58	-0.51	0.775

Table 4.18. Regression Coefficients for Aspect Ratio

Material	A_0	A_1	A_2	A_3	R^2
Amphora	5.96	6.36E-3	-0.55	-6.33E-2	0.75
Neat ABS	4.77	-3.64E-3	-0.22	-3.36E-2	0.43
CF-10	2.47	-9.74E-3	9.41E-2	0.15	6.26E-2
CF-13	3.11	-8.40E-3	-1.33E-2	9.09E-2	0.19

Table 4.19. Regression Coefficients for Horizontal Swell

Material	A_0	A_1	A_2	A_3	R^2
Amphora	2.99	1.78E-2	-0.14	-0.13	0.89
Neat ABS	4.11	2.19E-2	-0.11	-0.20	0.88
CF-10	2.28	1.86E-2	2.59E-2	-6.03E-2	0.71
CF-13	2.82	1.68E-2	-4.07E-2	-8.15E-2	0.55

Table 4.20. Regression Coefficients for Vertical Swell

Material	A_0	A_1	A_2	A_3	R^2
Amphora	4.05	1.41E-2	-0.57	-9.15E-2	0.800
Neat ABS	6.72	2.99E-2	-1.04	-0.18	0.777
CF-10	8.09	3.26E-2	-1.26	-0.25	0.823
CF-13	8.31	3.30E-2	-1.34	-0.23	0.730

Table 4.21. Regression Coefficients for Convexity Ratio

Material	A_0	A_1	A_2	A_3	R^2
Amphora	0.82	1.84E-4	5.35E-4	3.55E-3	0.227
Neat ABS	0.74	-9.85E-4	1.87E-2	5.95E-3	0.406
CF-10	0.62	-1.81E-4	1.65E-2	1.09E-2	0.528
CF-13	0.59	-1.29E-3	7.76E-3	2.00E-2	0.719

Table 4.22. Regression Coefficients for Compactness Ratio

Material	A_0	A_1	A_2	A_3	R^2
Amphora	0.91	-5.91E-5	4.10E-4	5.71E-3	0.576
Neat ABS	0.82	-7.42E-4	2.06E-2	6.82E-3	0.616
CF-10	0.77	-3.78E-4	9.73E-3	9.60E-3	0.126
CF-13	0.68	-8.00E-4	4.95E-3	1.83E-2	0.723

It should be noted that the cross-sectional area of a bead can be determined by dividing the flowrate regression equation by platform velocity. Aspect ratio could also be determined as a ratio of the horizontal to vertical regression equations, which would

result in an aspect ratio regression equation that is not linear. Finally, vertical and horizontal swell are related to vertical and horizontal bead height by the vertical nozzle height and the nozzle diameter. The information contained in Table 4.15 through Table 4.22 allow future users the ability to predict bead shape behavior, and use our work to facilitate further studies.

A few specific notes should be made on the data presented in these tables. Data for flowrate in Table 4.15 have high R^2 values above 0.8, indicating a good linear fit to the flowrate data. The Aspect Ratio regression fit, however, has extremely poor R^2 values, indicating that the data is not well described using a linear regression fit. It would be better for future users to combine the bead width and height regression equations, which have high R^2 values, and take the ratio of the horizontal regression equation to the vertical regression equation. Finally, convexity ratio and compactness ratio also have low values for R^2, indicating that linear regression is not a sufficient method for predicting bead convexity and compactness.

CHAPTER FIVE

Conclusions and Future Work

5.1 Conclusions

The process of scaling FFF from prototyping and modeling to industrial strength parts is complex, involving addition of discrete fibers to increase mechanical properties, transition from filament systems with heaters to extrusion systems with screws, and a re-examination of the process parameters in a large scale system. Acknowledging that fibers will be present to reinforce the printed part, and further that an extrusion system will be used for deposition, the focus of this work was to characterize and define deposition parameters and affect bead shape. Furthermore, our goal was to parse bead geometry data to form conclusive results on parameters that are sufficient for large scale FFF.

Cross section data was collected using the Exon 8 Single Screw Extruder and a translation platform with two automated axes, where beads were deposited on the platform across specific parameter settings of nozzle height, platform velocity, and screw RPM. Testing was performed using each of four polymers typical in FFF: Amphora^{TM}, Neat ABS, 10% Carbon Fiber Filled ABS, and 13% Carbon Fiber Filled ABS. Cross sections were taken from each bead using a low speed saw, which were then imaged and uploaded to MatLab. Boundaries of each cross section were traced using the 'im' suite, and stored as an array of (x,y) points which were used to calculate geometric parameters considered important in FFF processing.

5.1.1. Polymer Specific Conclusions

Amphora™. Of the four polymers tested, the Amphora™ was the least susceptible to swelling, surface defects, and shape irregularities based on the MatLab analysis. Bead shapes produced using the Amphora™ polymer are the most regular, showing a high degree of convexity and rectangularity, as well as the least amount of swell in both the horizontal and vertical directions. Aspect ratios are slightly higher than the other three polymers, which is due in part to the Amphora™ not curving at the edges, as seen in the carbon fiber beads.

However, flowrate is lower for the Amphora™ than the other polymers, suggesting that the screw has a more difficult time processing the polymer than ABS, and therefore the screw produces less volume in the same amount of time. Ultimately, lower flowrate would result in longer production times or increased energy for the process to attain a similar flowrate as the ABS, a drawback that should be evaluated on an individual basis for FFF application.

Neat ABS. Maximum flowrate for the ABS polymers were similar, each producing approximately 150% more volume compared to the Amphora™, indicating that the extruder is more readily able to process the material, and that parts could be printed more quickly with ABS. However, the neat ABS was more susceptible to warping and irregular surface features, performing lower than Amphora™ with respect to swelling, convexity, and compactness. Aspect ratios for the neat ABS were less variant than Amphora™, but still cover a range wide enough to achieve different desired surface finishes. Fewer parameter settings produced acceptable bead shapes for FFF, with those

parameters that were acceptable taking place at higher settings of platform velocity and nozzle height.

10% Carbon Fiber Filled ABS. The differences between unfilled and filled ABS were prominent, with the most notable distinguishing trait being the tendency for the carbon fiber ABS to curve at the edges at lower platform velocities and nozzle heights. Tendency to curve removed many carbon fiber deposition parameters as possibilities for FFF, effectively shrinking the range of acceptable deposition settings. Of the parameters left unaffected by curvature, aspect ratio has little variation which does not allow the user to easily overcome surface finish effects at the edges of a part. Furthermore, few parameter settings fall into acceptable ranges for convexity, and even fewer for compactness, suggesting that this ABS/carbon fiber blend may not be well suited for FFF under these extrusion conditions.

13% Carbon Fiber Filled ABS. The 13% carbon fiber filled ABS beads did not create worse deposition results than the 10% carbon fiber filled ABS beads. There are many reasons for this result, including that the two types of carbon fiber ABS are produced by different companies, and may be different blends of ABS as suggested by the DSC tests in Chapter Three. However, many similarities between the bead shapes created by the 10% and 13% carbon fiber filled ABS beads indicate that the polymers behave similar during extrusion, having similar curvature and surface irregularity along the edges of the beads. The 13% carbon fiber beads performed better than the 10% carbon fiber beads in convexity and compactness, allowing for a broader operating range of deposition settings to produce acceptable bead shapes. Swell ratios and aspect ratios

were comparable for both carbon fiber ABS polymer blends, covering a smaller range than the Amphora™ and neat ABS and creating potential issues with surface finish.

5.1.2. General Conclusions

Overall, better bead shapes were produced as table speed and nozzle height increased, with the most regularly shaped cross sections being those deposited at higher platform velocities (10mm/s and 15mm/s) and higher nozzle heights (3.25mm and 5mm). RPM had little effect on the geometry parameters aside from increasing the cross sectional area of the beads. In fact, cross sectional area was found to scale directly with RPM while maintaining the same shape. The carbon fiber filled ABS polymers were the most sensitive to the deposition process, having the largest defects including curvature at the edges, while the Amphora™ was the most robust to processing conditions. However, the Amphora™ also had a significantly lower flowrate, creating smaller cross sections and increasing the time needed to print an Amphora™ part. There is also the issue of the Amphora™ pulsing during deposition due to the screw having difficulties processing the polymer, which must also be taken into account when making a large scale FFF materials decision.

5.2. Future Work

There are several future research options based on the findings of this work, which can be grouped into two categories. The first is improvements to the FFF extrusion system, and the second further geometry and parameter studies to be conducted using the existing system.

5.2.1. System Improvements

The extrusion system has several aspects that could be improved to further this research, listed here:

- Redesign the pellet feeding system, including the hopper, aluminum spacers, and 45° bend as a cohesive unit, to better allow for changes in material and ease of removal.

- Automate the z-axis which controls the nozzle height, allowing for users to easily build parts in three dimensions without manually increasing the nozzle height.

- Increase the size of the deposition platform to allow for a larger build volume.

- Write MatLab code for automatically generating the command string input into LabVIEW which operates the platform, allowing the user to easily generate new laydown patterns.

- Determine the mechanism behind low Amphora™ flowrate and pulsing, which was partially solved by the addition of aluminum spacers between the hopper and the screw.

Each of these improvements would allow the user to more easily collect deposition data, and expand the applicability of this system to large scale FFF.

5.2.2. Further Studies

More research data can be collected on the existing system to further understand the effects of parameters on large scale FFF, and by increasing the amount of data available researchers could more easily determine other factors of interest. Some potential future studies include:

- Evaluate another FFF material using the same parameters, potentially PLA or nylon, and compare with existing results.

- Using some of the better parameter settings for each polymer, perform additional studies with multiple beads, examining further FFF parameters

such as distance between beads, incremented nozzle height between layers, edge surface finish between layers, and voids.

- Study and model fluid dynamics of extrusion screw, to better understand flow and how it affects deposition.

- Modify extruder to include pressure gauges to monitor pressure drops within the system.

Large scale FFF has the potential to revolutionize traditional manufacturing, but requires further study to become a viable industrial technology. The ideas presented here for further study would allow FFF technology to progress further toward the goal of industrial realization.

APPENDIX

APPENDIX A

Large Scale Deposition System Operation

The extrusion system used in this research is a combination of a two-axis programmable platform and an extrusion welder on a vertical axis. Each of these components are operated separately, as outlined here.

A.1 Platform

The programmable platform is driven by three NEMA 14, 750 RPM, 10.2 in-oz torque stepper motors, one at each end of the longer x-axis and one for the shorter y-axis, as shown in Figure A.1. Two motors are used in the longer axis to provide adequate torque along the travel length, with a single motor suitable for the second axis. Each motor-axis set is controlled using an R256 controller, with both controllers wired into a USB485 converter card that hooks directly into any computer USB port.

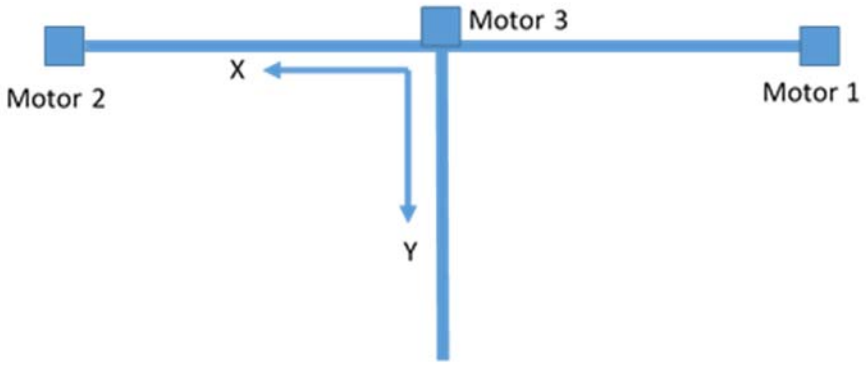

Figure A.1. Stepper motor placement for (x,y) axes.

Several failsafe components are wired into the platform system, including an optical interrupter for each axis, which senses when the axis has traveled to its 'home' position and stops translation. A pushbutton for emergency stopping is also included, which can be programmed to stop translation at any time. Power to the system is supplied using a 30V 3A DC power supply. A simple circuit schematic is shown in Figure A.2, with more detailed diagrams of each component included in the McMaster-Carr stepper motor documentation [68].

To operate the table, a program is implemented in LabVIEW which communicates with the converter card through a COM port; COM port number changes depending on which USB port the card is plugged into. A block diagram of the LabVIEW program and the user interface is shown in Figure A.3.

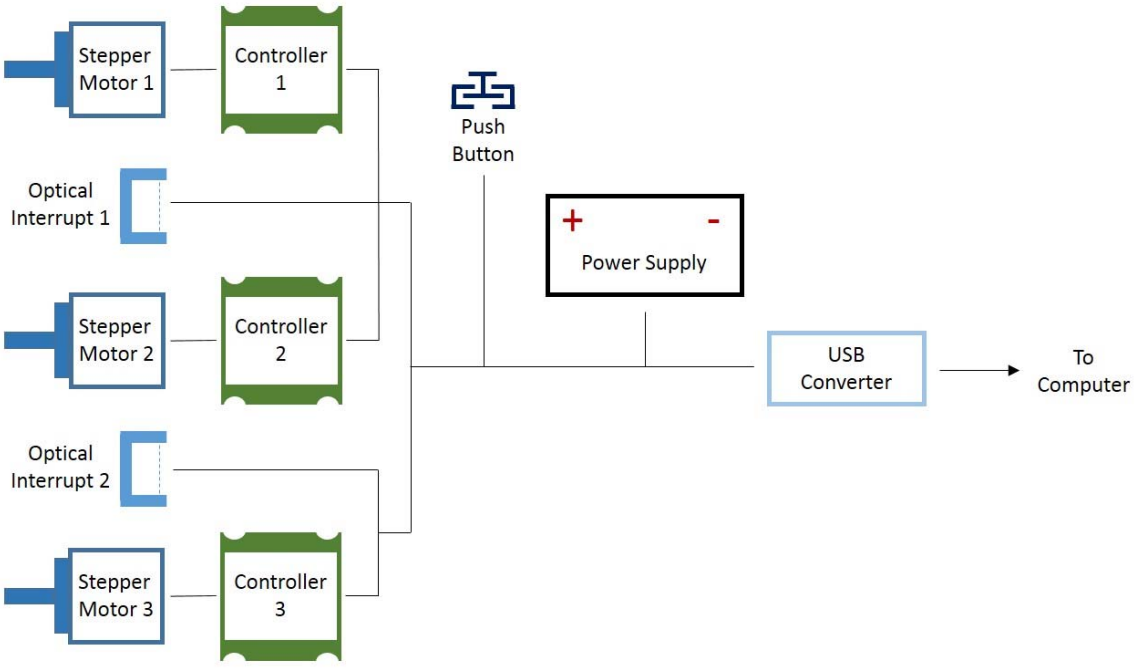

(a)

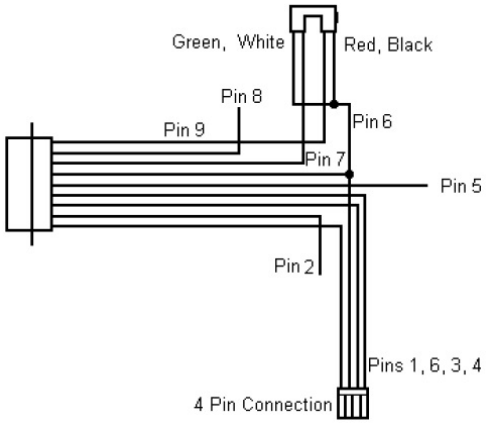

(b)

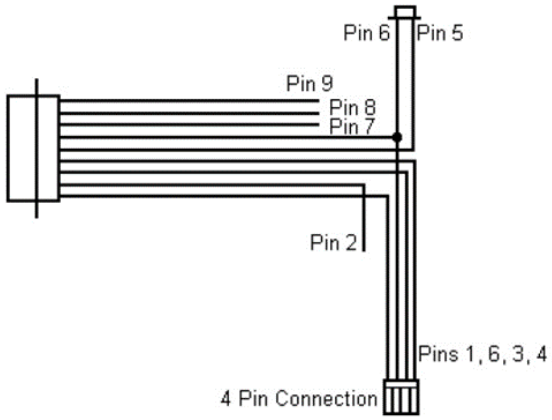

(c)

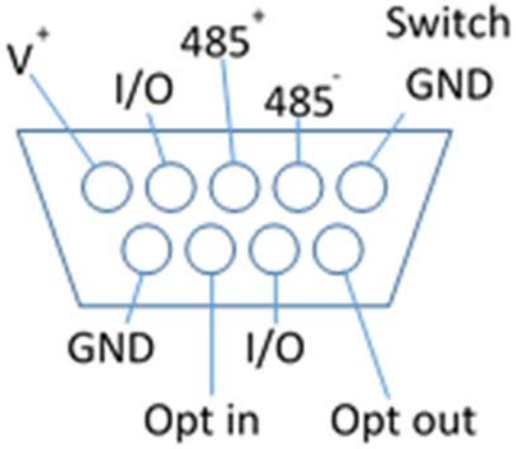

(d)

Figure A.2. Table circuit diagrams.

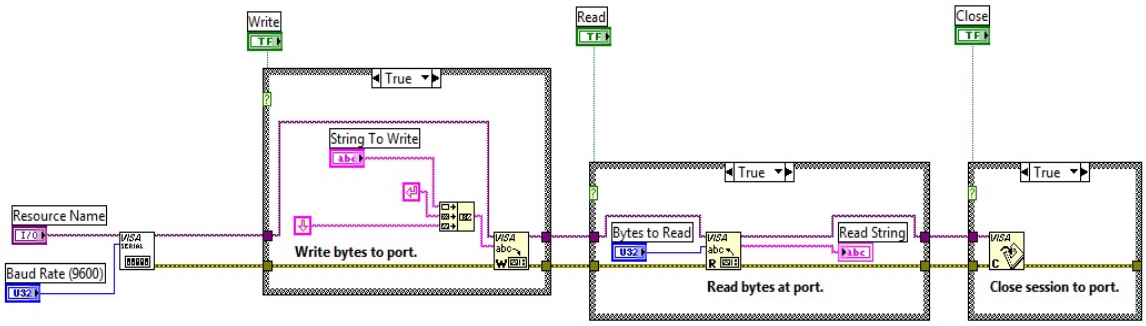

(a)

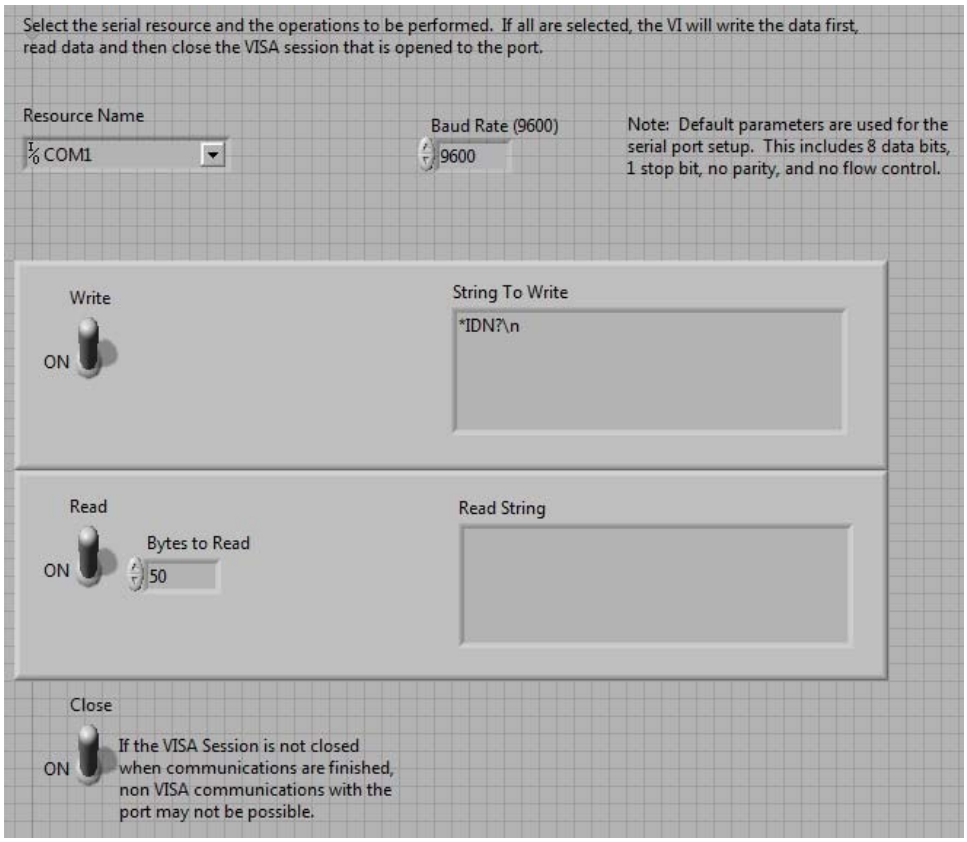

(b)

Figure A.3. LabVIEW block diagram and user interface for operating platform.

Commands are typed into the “String To Write” field, and executed by hitting “Run” in the LabVIEW command window. A new command cannot be executed until the previous command has been relayed to the controllers, resulting in a 2-3 second delay between executable commands. As a result, precise movements are best executed using loops and pauses within a single command rather than several commands executed in succession. A list of typical commands are outlined in Table A.1:

Table A.1. List of basic commands for operating platform.

/1, /2, /3, /A, /_	Always begin a command string with ‘/’, followed by the motor number(s). ‘1’, ‘2’, and ‘3’ call the individual motors as in Fig. 1, while ‘A’ calls both motors 1 and 2, and ‘_’ calls all motors.
/1m50R	‘m50’ specifies the percentage amps used by the motor, and should be kept at 50%. Truncate the string with ‘R’ to execute.
/1V200000R	‘V’ sets the velocity of the motor in steps per second, and can range from 0:300000.
/1F1R	‘F1’ switches the rotation polarity of motor 1. Since the primary axis has two motors, one of them must be switched to rotate with each other.
200000	When specifying the number of steps to move, the motor default resolution is 256 μsteps/step, and the user inputs the desired distance in μsteps.
/1Z7000000R	‘Z’ tells the motor to rotate toward home 7000000 steps or until the optical sensor is interrupted.
/1z0R	‘z’ sets the absolute position of the current motor position, in this case to 0.
/1P100000R	‘P’ translates the motor in the positive direction.
/1D100000R	‘D’ translates the motor in the negative direction.
/1A100000R	‘A’ translates the motor to the absolute position.
/1M1000R	‘M’ pauses the motor for a specified number of milliseconds.
/1TR	‘T’ terminates the current command to the motor.
/1H04R	‘H04’ sends the command to the motor, but the command waits for the push button to execute.
/1gP100000G0R	‘g…G0’ is a loop, with commands between ‘g’ and ‘G’ iterating a specified number of times. In this case, ‘G0’ is an infinite loop, while ‘G5’ would iterate 5 times.

/_TR\r /_A0R	In LabView, several lines can be typed before sending the commands to the motor. Each line can be terminated with '\r' before starting the next line.

Using the basic commands from Table A.1, a series of useful strings are generated which allow the platform full range of movement in the FFF process. A partial list of these strings are shown in Table A.2:

Table A.2. List of initiation and concatenation commands for operating platform.

/_m50V200000R\r /1F1R\r /_Z8000000z0R	This is an initialization sequence. 'm' sets the current, 'V' sets the velocity, 'F1' reverses the polarity of the motor, then all motors travel until their optical sensors are interrupted, 'Z', before setting that absolute position to position 0, 'z'.
/AA2000000gP3000000M3000… D3000000M3000G3A0R\r /3A2000000gM15000P600000… M15000P600000G3M3000A0R	Each line calls a different axis, 'A' for the primary and '3' for the secondary axis. In the first string, the command moves the axis to an absolute position before starting a loop, moving in the positive direction, pausing, and moving back again 3 times. At the end, the motors return to home. In the second string, the motor pauses, moves positive, pauses and moves positive again before moving home. Note that the amount of time each motor pauses is equal to the time the other motor is moving. A visual of this movement is provided in Fig. 4.
/_TR\r /_A0R	Strings terminate the commands at all motors, then returns all motors to home position.

Both axes are outfitted with ACME-10 ½" screws which give 0.1 in/rev. At 1.8 deg/step, the motor provides 200 steps/rev, or 2000 steps/in. With a resolution of 256 μsteps/step, the code in the second row of Table A.2, as shown in Figure A.4, moves horizontally 3000000 μsteps, 5.86in, and vertically 600000 μsteps, 0.98in, before repeating the motion in a loop for three iterations.

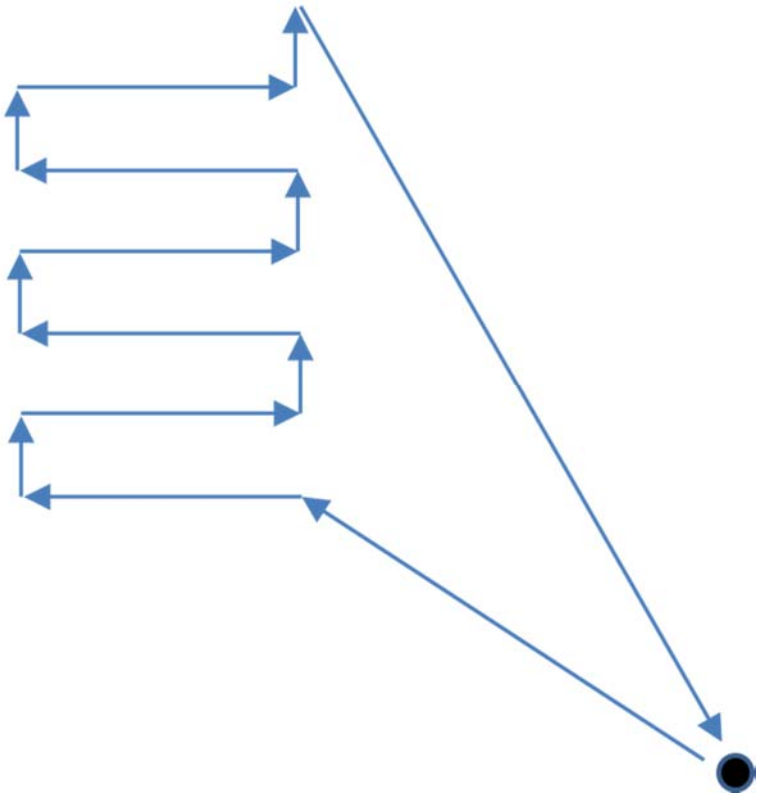

Figure A.4. Translation pattern from Table A.2.

The platform also has adjustable height feet, which can be modified to ensure the platform travels horizontally. To determine if the platform is level, a dial indicator can be attached to the steel extruder bracket hanging from the extrusion stand, and the platform feet adjusted to maintain a constant reading during platform movement. Given that the extruder is on a vertically adjustable screw, there is not an exact necessary height for the table, simplifying the levelling process by allowing the platform height to have a range of acceptable values.

A.2 Exon8 Extruder

The extruder portion of the large scale deposition system is the Exon8 single screw extruder from HapCo Inc, which at an operating temperature of 170°C is capable of outputting 11 lbs/min of Amphora™ polymer. Operating instructions for the extruder are as follows.

The extruder system is run through a control box, as shown in Figure A.5. To start the extruder, turn the knob on the back of the control box clockwise from horizontal to diagonal as shown in Figure A.6, with the Off position showing a circle and the On position showing a line.

Figure A.5. Exon8 Control Box.

Figure A.6. Exon8 in Off (left) and On (right) positions.

The control box allows the operator to specify separate temperatures for the extruder and the preheat air. After turning the system on, the control box will look like Figure A.7, with the bottom digital display flashing ‘bb’ to indicate the system is not preheated.

Figure A.7. Exon8 Control Box immediately after being turned on.

Both extruder and air temperatures are in degrees Celsius, and can be adjusted using the arrows at any time. However, the system will only operate when the actual temperature (in red) is within 15°C of the specified temperature (in green). In general, the air temperature reaches steady state within seconds, while the extruder takes approximately 20 minutes to preheat.

When the extruder temperature is within range, the screw RPM can be specified on the bottom digital display in the range 0-80 RPM. The screw will not begin rotating until the user presses the 'RUN' button, and the screw can be stopped at any time by pressing the 'STOP/RESET' button. RPM can also be adjusted using the potentiometer knob to the right of the RPM readout. Finally, the screw can be stopped in case of emergency by pressing the red 'EMERGENCY STOP' push button.

The extruder as mentioned previously is mounted on a vertically adjustable axis, which can be used to modify the distance between the extruder nozzle and the table. The vertical mounting system is shown in Figure A.8.

The extruder is mounted on three parallel vertical rods, the middle of which is an ACME-5 ¾" screw which gives 0.2 in/rev. The other two axes are unthreaded rods on either side of the screw rod to minimize torque on the screw itself and provide stability to the system. On each of the unthreaded rods is a ball bearing slide-lock nut, which locks the system in place during extrusion. The nuts are moved by holding the larger main section and pulling down on the grip, then sliding the nut into its new position before releasing, as shown in Figure A.9. Slide-lock nut movement.
. The locking nuts ensure that the mass of the extruder does not cause the system to drift down during operation, and should always be set before use.

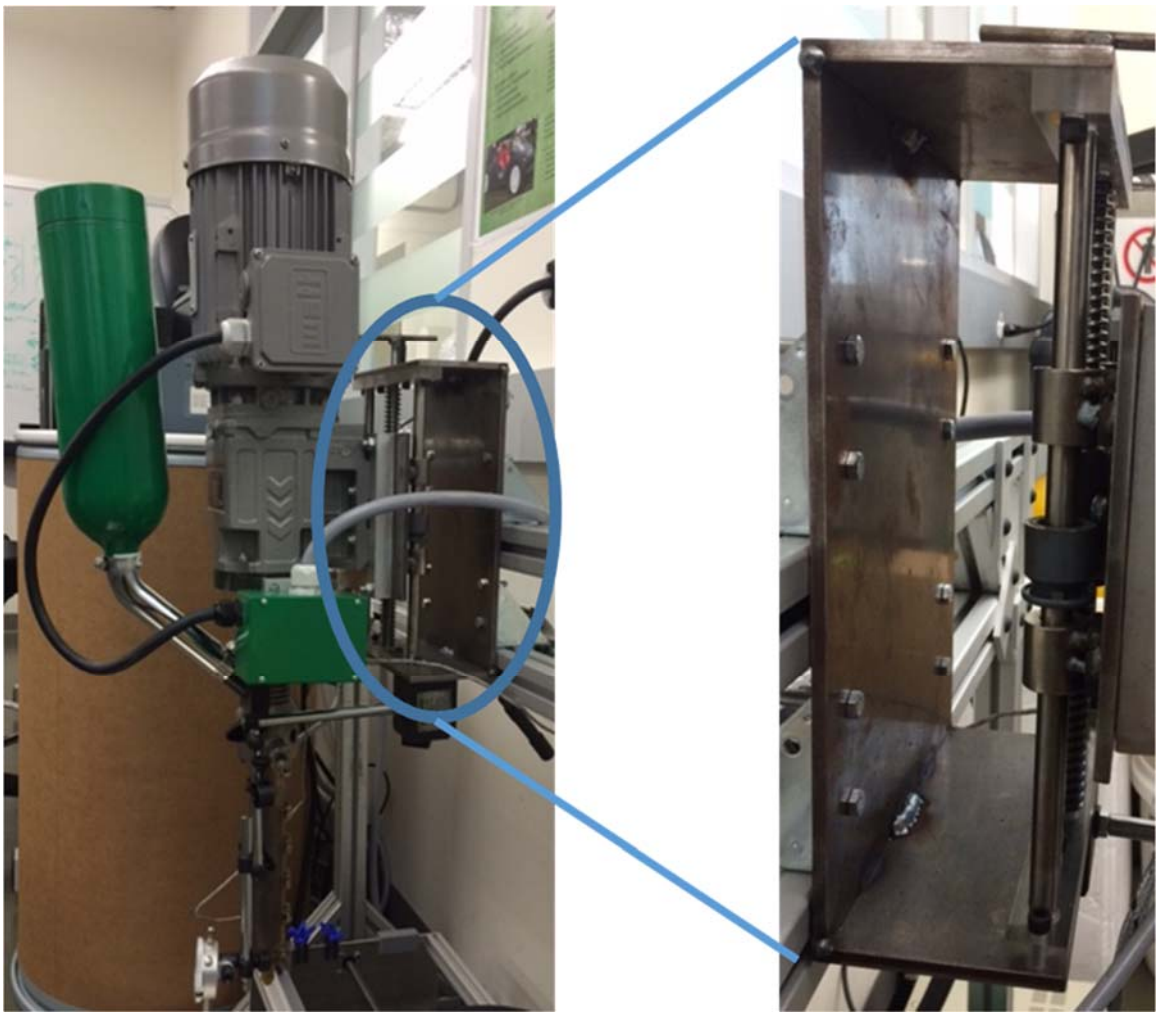

Figure A.8. Vertical axis translation system.

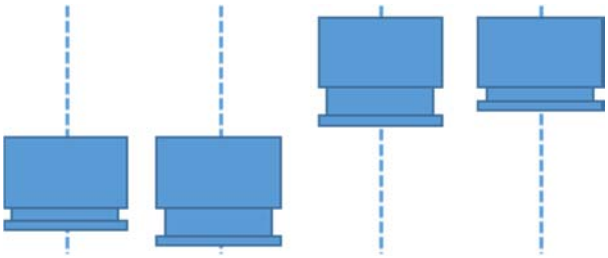

Figure A.9. Slide-lock nut movement.

Finally, the nozzle tip of the extruder can be removed or outfitted as needed using a metric size 13 wrench, and keeping in mind that the threads are reverse-threaded because the extruder spends its life upside down.

BIBLIOGRAPHY

[1] "MakerBot Replicator 2X," *MakerBot*. [Online]. Available: http://store.makerbot.com/replicator2x. [Accessed: 21-Apr-2016].

[2] "Modulus of Elasticity or Young's Modulus - and Tensile Modulus for some common Materials." [Online]. Available: http://www.engineeringtoolbox.com/young-modulus-d_417.html. [Accessed: 21-Apr-2016].

[3] E. J. Barbero, *Introduction to Composite Materials Design*, 2nd Ed. CRC Press, 2011.

[4] "World's First 3D Printed Car." [Online]. Available: http://web.ornl.gov/sci/manufacturing/media/news/3d-car/. [Accessed: 11-Feb-2016].

[5] T. J. Horn and O. L. A. Harrysson, "Overview of current additive manufacturing technologies and selected applications," *Sci. Prog.*, vol. 95, no. 3, p. 255+, 2012.

[6] D. T. Pham and R. S. Gault, "A comparison of rapid prototyping technologies," *Int. J. Mach. Tools Manuf.*, vol. 38, no. 10–11, pp. 1257–1287, Oct. 1998.

[7] P. M. Pandey, N. Venkata Reddy, and S. G. Dhande, "Improvement of surface finish by staircase machining in fused deposition modeling," *J. Mater. Process. Technol.*, vol. 132, no. 1–3, pp. 323–331, Jan. 2003.

[8] D. Espalin, J. A. Ramirez, F. Medina, and R. Wicker, "Multi-material, multi-technology FDM: exploring build process variations," *Rapid Prototyp. J.*, vol. 20, no. 3, pp. 236–244, 2014.

[9] N. S. A. Bakar, M. R. Alkahari, and H. Boejang, "Analysis on fused deposition modelling performance," *J. Zhejiang Univ. Sci. A*, vol. 11, no. 12, pp. 972–977, Dec. 2010.

[10] K. Salonitis, J. Pandremenos, J. Paralikas, and G. Chryssolouris, "Multifunctional materials: engineering applications and processing challenges," *Int. J. Adv. Manuf. Technol.*, vol. 49, no. 5–8, pp. 803–826, Dec. 2009.

[11] M. Lauwaert, "Playing outside the box - on LEGO toys and the changing world of construction play," *Hist. Technol.*, vol. 24, no. 3, pp. 221–237, Sep. 2008.

[12] R. Melnikova, A. Ehrmann, and K. Finsterbusch, "3D printing of textile-based structures by Fused Deposition Modelling (FDM) with different polymer materials," *IOP Conf. Ser. Mater. Sci. Eng.*, vol. 62, no. 1, p. 12018, 2014.

[13] J. F. Rodriguez, J. P. Thomas, and J. E. Renaud, "Characterization of the mesostructure of fused-deposition acrylonitrile-butadiene-styrene materials," *Rapid Prototyp. J.*, vol. 6, no. 3, pp. 175–185, 2000.

[14] Dietmar Drummer, Sandra Cifuentes-Cuéllar, and Dominik Rietzel, “Suitability of PLA/TCP for fused deposition modeling,” *Rapid Prototyp. J.*, vol. 18, no. 6, pp. 500–507, Sep. 2012.

[15] H. . Ramanath, M. Chandrasekaran, C. . Chua, K. . Leong, and K. . Shah, “Modeling of extrusion behavior of biopolymer and composites in fused deposition modeling,” *Key Eng. Mater.*, vol. 334–335, pp. 1241–1244, 2007.

[16] X. Li, R. Cui, L. Sun, K. E. Aifantis, Y. Fan, Q. Feng, F. Cui, and F. Watari, “3D-printed biopolymers for tissue engineering application,” *Int. J. Polym. Sci.*, 2014.

[17] D. Roberson, C. M. Shemelya, E. MacDonald, and R. Wicker, “Expanding the applicability of FDM-type technologies through materials development,” *RAPID Prototyp. J.*, vol. 21, no. 2, pp. 137–143, 2015.

[18] N. Hill and M. Haghi, “Deposition direction-dependent failure criteria for fused deposition modeling polycarbonate,” *Rapid Prototyp. J.*, vol. 20, no. 3, pp. 221–227, 2014.

[19] S. H. Masood, K. Mau, and W. . Song, “Tensile properties of processed FDM polycarbonate material,” in *Materials Science Forum*, 2010, vol. 654–656, pp. 2556–2559.

[20] O. S. Carneiro, A. F. Silva, and R. Gomes, “Fused deposition modeling with polypropylene,” *Mater. Des.*, vol. 83, pp. 768–776, Oct. 2015.

[21] Anonymous, “Nylon FDM Material Offers Greater Strength,” *MoldMaking Technology*, p. 14, Feb-2014.

[22] M. J. Cieslinski, K. J. Meyer, J. T. Hofmann, P. Wapperom, and D. G. Baird, “Simulating orientation of long, semi-flexible glass fibers in three-dimensional injection molded thermoplastic composites,” presented at the SPE ACCE, 2013, vol. 2.

[23] W. Zhong, F. Li, Z. Zhang, L. Song, and Z. Li, “Short fiber reinforced composites for fused deposition modeling,” *Mater. Sci. Eng. A*, vol. 301, no. 2, pp. 125–130, Mar. 2001.

[24] Eastman, “Eastman Amphora 3D Polymer AM1800.” Sep-2014.

[25] Q. Sun, G. M. Rizvi, C. T. Bellehumeur, and P. Gu, “Effect of processing conditions on the bonding quality of FDM polymer filaments,” *Rapid Prototyp. J.*, vol. 14, no. 2, pp. 72–80, 2008.

[26] R. W. Gray, D. G. Baird, and J. H. Bohn, “Effects of processing conditions on short TLCP fiber reinforced FDM parts,” *Rapid Prototyp. J.*, vol. 4, no. 1, pp. 14–25, 1998.

[27] H. K. Garg and R. Singh, “Pattern Development for Manufacturing Applications with Fused Deposition Modelling – A Case Study,” *Int. J. Automot. Mech. Eng.*, vol. 7, pp. 981–992, Jun. 2013.

[28] S.-H. Ahn, M. Montero, D. Odell, S. Roundy, and P. K. Wright, “Anisotropic material properties of fused deposition modeling ABS,” *Rapid Prototyp. J.*, vol. 8, no. 4, p. 248, 2002.

[29] S. H. Ahn, C. Baek, S. Lee, and I. S. Ahn, “Anisotropic Tensile Failure Model of Rapid Prototyping Parts - Fused Deposition Modeling (FDM),” *Int. J. Mod. Phys. B*, vol. 17, no. 08n09, pp. 1510–1516, Apr. 2003.

[30] A. Armillotta, “Assessment of surface quality on textured FDM prototypes,” *Rapid Prototyp. J.*, vol. 12, no. 1, pp. 35–41, 2006.

[31] A. Boschetto, V. Giordano, and F. Veniali, “3D roughness profile model in fused deposition modelling,” *Rapid Prototyp. J.*, vol. 19, no. 4, pp. 240–252, 2013.

[32] “PLA Filament,” *MakerBot*. [Online]. Available: http://store.makerbot.com/filament/pla#rep2-truered. [Accessed: 13-Jan-2016].

[33] “BMW i : Concept.” [Online]. Available: http://www.bmw.com/com/en/insights/corporation/bmwi/concept.html#carbon. [Accessed: 11-Feb-2016].

[34] H. Yoshida, T. Igarashi, Y. Obuchi, Y. Takami, J. Sato, M. Araki, M. Miki, K. Nagata, K. Sakai, and S. Igarashi, “Architecture-scale Human-assisted Additive Manufacturing,” *ACM Trans Graph*, vol. 34, no. 4, p. 88:1–88:8, Jul. 2015.

[35] S. Lim, R. A. Buswell, T. T. Le, S. A. Austin, A. G. F. Gibb, and T. Thorpe, “Developments in construction-scale additive manufacturing processes,” *Autom. Constr.*, vol. 21, pp. 262–268, Jan. 2012.

[36] G. B. Jeffery, “The Motion of Ellipsoidal Particles Immersed in a Viscous Fluid,” *Proc. R. Soc. Lond. Ser. Contain. Pap. Math. Phys. Character*, vol. 102, no. 715, pp. 161–179, 1922.

[37] “The Collected Paper of: Albert Einstein, Volume 2, The Swiss Years: Writings, 1900-1909.” Princeton University Press, 1989.

[38] F. Folgar and Tucker, Charles L. III, “Orientation Behavior of Fibers in Concentrated Suspensions,” *J. Reinf. Plast. Compos.*, vol. 3, no. 2, pp. 98–119, Apr. 1984.

[39] S. G. Advani and C. L. Tucker III, “The Use of Tensors to Describe and Predict Fiber Orientation in Short Fiber Composites,” *J. Rheol. 1978-Present*, vol. 31, no. 8, pp. 751–784, Nov. 1987.

[40] J. Wang, J. F. O’Gara, and C. L. T. Iii, “An objective model for slow orientation kinetics in concentrated fiber suspensions: Theory and rheological evidence,” *J. Rheol. 1978-Present*, vol. 52, no. 5, pp. 1179–1200, Sep. 2008.

[41] J. H. Phelps and C. L. Tucker III, “An anisotropic rotary diffusion model for fiber orientation in short- and long-fiber thermoplastics,” *J. Non-Newton. Fluid Mech.*, vol. 156, no. 3, pp. 165–176, Feb. 2009.

[42] J. S. Cintra, “Orthotropic Closure Approximation for Flow Induced Fiber Orientation,” *J. Rheol. - J RHEOL*, vol. 39, no. 6, 1995.

[43] S. Montgomery-Smith, D. Jack, and D. E. Smith, “The Fast Exact Closure for Jeffery’s equation with diffusion,” *J. Non-Newton. Fluid Mech.*, vol. 166, no. 7–8, pp. 343–353, Apr. 2011.

[44] C. L. Tucker III and E. Liang, “Stiffness predictions for unidirectional short-fiber composites: Review and evaluation,” *Compos. Sci. Technol.*, vol. 59, no. 5, pp. 655–671, Apr. 1999.

[45] D. A. Jack and D. E. Smith, “Elastic Properties of Short-fiber Polymer Composites, Derivation and Demonstration of Analytical Forms for Expectation and Variance from Orientation Tensors,” *J. Compos. Mater.*, vol. 42, no. 3, pp. 277–308, Feb. 2008.

[46] L. J. Love, V. Kunc, O. Rios, C. E. Duty, A. M. Elliott, B. K. Post, R. J. Smith, and C. A. Blue, “The importance of carbon fiber to polymer additive manufacturing,” *J. Mater. Res.*, vol. 29, no. 17, pp. 1893–1898, Sep. 2014.

[47] K. Yasuda, S. Henmi, and N. Mori, “Effects of abrupt expansion geometries on flow-induced fiber orientation and concentration distributions in slit channel flows of fiber suspensions,” *Polym. Compos.*, vol. 26, no. 5, pp. 660–670, Oct. 2005.

[48] J. Nixon, B. Dryer, D. Chiu, I. Lempert, and D. I. Bigio, “Three parameter analysis of fiber orientation in fused deposition modeling geometries,” in *Annual Technical Conference - ANTEC, Conference Proceedings*, 2014, vol. 2, pp. 985–995.

[49] B. P. Heller, D. E. Smith, and D. A. Jack, “Effects of extrudate swell and nozzle geometry on fiber orientation in Fused Filament Fabrication nozzle flow,” *Addit. Manuf.*

[50] A. Bellini, S. Güçeri, and M. Bertoldi, “Liquefier Dynamics in Fused Deposition,” *J. Manuf. Sci. Eng.*, vol. 126, no. 2, p. 237, 2004.

[51] B. N. Turner, R. Strong, and S. A. Gold, “A review of melt extrusion additive manufacturing processes: I. Process design and modeling,” *Rapid Prototyp. J.*, vol. 20, no. 3, pp. 192–204, 2014.

[52] N. Mostafa, H. M. Syed, S. Igor, and G. Andrew, “A study of melt flow analysis of an ABS-Iron composite in fused deposition modelling process,” *Tsinghua Sci. Technol.*, vol. 14, no. S1, pp. 29–37, Jun. 2009.

[53] A. V. Gusarov, M. Pavlov, and I. Smurov, “Residual Stresses at Laser Surface Remelting and Additive Manufacturing,” *Phys. Procedia*, vol. 12, Part A, pp. 248–254, 2011.

[54] A. S. Wu, D. W. Brown, M. Kumar, G. F. Gallegos, and W. E. King, “An Experimental Investigation into Additive Manufacturing-Induced Residual Stresses in 316L Stainless Steel,” *Metall. Mater. Trans. A*, vol. 45, no. 13, pp. 6260–6270, Sep. 2014.

[55] Y. Jin, J. Zhang, Y. Wang, and Z. Zhu, “Filament geometrical model and nozzle trajectory analysis in the fused deposition modeling process,” *J. Zhejiang Univ. Sci. A*, vol. 10, no. 3, pp. 370–376, Mar. 2009.

[56] “HAPCO INC.” [Online]. Available: http://hapcoinc.com/product.php?name=extruders-all-models. [Accessed: 21-Apr-2016].

[57] “80/20 Inc. - T-slotted aluminum framing system.” [Online]. Available: https://www.8020.net/. [Accessed: 25-Apr-2016].

[58] S. H. Kim, H. K. Yoon, S. J. Kim, and Y. H. Park, “TGA CHARACTERISTIC AND FABRICATION OF POROUS SiC CERAMICS,” *Int. J. Mod. Phys. B*, vol. 24, no. 15n16, pp. 2863–2868, Jun. 2010.

[59] R. Tsukuda, S. Sumimoto, and T. Ozawa, “Thermal conductivity and heat capacity of ABS resin composites,” *J. Appl. Polym. Sci.*, vol. 63, no. 10, pp. 1279–1286, Mar. 1997.

[60] ASTM, “D1238-13: Standard Test Method for Melt Flow Rates of Thermoplastics by Extrusion Plastometer.” ASTM, Aug-2013.

[61] N. G. Karsli, A. Aytac, and V. Deniz, “Effects of initial fiber length and fiber length distribution on the properties of carbon-fiber-reinforced-polypropylene composites,” *J. Reinf. Plast. Compos.*, vol. 31, no. 15, pp. 1053–1060, Aug. 2012.

[62] Makerbot Industries LLC, “Makerbot PLA Filament.” .

[63] Buehler, “IsoMet Low Speed Saw.” Buehler, 2013.

[64] D. G. Baird and D. I. Collias, *Polymer Processing: Principles and Design*, 2nd Ed. John Wiley & Sons, Inc., 2014.

[65] J. Zunic and P. L. Rosin, “A new convexity measure for polygons,” *IEEE Trans. Pattern Anal. Mach. Intell.*, vol. 26, no. 7, pp. 923–934, Jul. 2004.

[66] W. Li, M. F. Goodchild, and R. Church, “An Efficient Measure Of Compactness For Two-Dimensional Shapes And Its Application In Regionalization Problems,” *Int. J. Geogr. Inf. Sci.*, vol. 27, no. 6, pp. 1227–1250, 2013.

[67] S. C. Chapra, *Applied numerical methods with MATLAB for engineers and scientists*, 2nd ed. Boston: McGraw-Hill Higher Education, 2008.

[68] “McMaster-Carr.” [Online]. Available: http://www.mcmaster.com/. [Accessed: 21-Apr-2016].